Comparative Numerical Modelling of Tsunami Propagation Over Various Bathymetries

A thesis

submitted in partial fulfilments

of the requirements for the Degree

of

Doctor of Philosophy in Physics

in the

University of Canterbury

by

Beth Geraghty

Department of Physics and Astronomy

University of Canterbury

2006

Abstract

This thesis uses numerical simulations to assess the most suitable model type for simulating dispersive and non dispersive tsunami wave propagation over a range of bathymetries. These simulations are presented in two parts. The first part highlights differences between results as predicted by a fully nonlinear Boussinesq model (with its ability to predict dispersion) and a non dispersive, linear or weakly nonlinear model, for simulations of a dispersive wave incident at various idealized bathymetric features. The second part determines the efficacy in a real world application of the Boussinesq model as opposed to a nonlinear shallow water model. In addition, a discussion on the geophysical parameters which influence the choice of numerical model for simulating tsunami propagation in a particular bathymetric region is provided.

The fundamental model in this study is the fully nonlinear extended Boussinesq model Geowave V1.0 (GW). For the purpose of the current research project the linear (GWL) and weakly nonlinear shallow water equations (GWS) were implemented into GW.

Part one uses idealized bathymetry which contains either a single or a double bathymetric feature. The length of the wave in relation to the water depth is analogous to that of a potential tsunami produced from a mechanism such as a sub-marine landslide, slump or volcanic eruption. This theoretical research is then linked to the geophysical world.

Numerical results for single features show that small changes in depth across a continuous feature can cause transmitted wave amplitudes predicted by the fully nonlinear extended Boussinesq equation set of Geowave (GWB), to be significantly smaller than those by GWS. Differences between GWB and GWS predictions of reflected and transmitted amplitudes depend more on the type and form of the feature than on whether

its width will cause the strongest reflection. Numerical results for scatter from a double feature show that the reflected wave amplitude is dependent on the second feature located within a distance of 1.5λ. Contributions from the fully nonlinear dispersive terms are shown to be most dependent on this separation distance and are of particular significance when the features are separated by 0.5λ. Application of the above research to an existing geophysical feature suggests the potential significance in the use of a Boussinesq model for simulation of a tsunami (with dispersive properties) over a varied bathymetric domain.

The second part of this research uses Geowave to simulate propagation of dispersive and non dispersive hypothetical tsunami waves over a variety of geophysical domains. Geowave's fully nonlinear extended Boussinesq equation set is shown to be robust in predicting evolution of both types of wave. This work ascertains that Geowave is not suitable for application to a large scale domain due to its reduced ability in predicting coastal wave amplification.

Acknowledgements

My most sincere thanks goes to all those who provided me with support throughout the completion of this thesis. In particular, to my Principal Supervisor Darlene Heuff, for her scientific assistance and friendship during the years of both my honours degree and PhD and to my co-supervisors, Bob Spigel and Jack Baggaley, and mentor Roger Reeves.

Outside of the university I would like to express my gratitude to Willem de Lange for his prompt answers to my emails and Ahmet Yalciner for his words of encouragement in Crete, 2005.

I would like to thank Phil Watts, for providing me with the rights to use Geowave V1.0, and other tsunami scientists which include Roy Walters, James Goff, Gaye Downes, William Power and Patrick Liu, for various pieces of assistance in personal communications throughout my PhD.

Thanks to the people of the Beer Society for providing relaxing and fun times only a few yards walk from my office.

A special thanks to all my friends, especially Yan Zeng, Andreas Baumgaertner, Lizzy Wylie de Boer and Ben Carter, for keeping me sane on a daily basis, and to Craig Mills, Yuko Nagata, Robert Weiss and Debbie Salmon for your support from a distance.

I am forever appreciative to my mother, Helen Mckinlay for her help in editing my thesis and the fun that she made it, and to my sister (Emma) and Dad (Mike), for their consistent encouragement. Finally, a gigantic thanks to my partner Martin for the distances he went to support me in the completion of this thesis.

Contents

Figures

Tables

Chapter 1

Introduction

The 2004 Indian Ocean tsunami, in which approximately 216,000 perished, is the second largest death toll ever recorded as a result of natural causes. The dramatic impact of this event has strongly reinforced the necessity of research into tsunamis.

A tsunami is a wave of water that is caused by a sudden large disturbance to the ocean. The main mechanisms are submarine earthquakes and landslides (refer Chapter 2). This disturbance causes an immediate vertical displacement of water. The wavelength of a tsunami is dependent on its generation source, as discussed in Chapter 2. It can vary from several to a few hundred kilometres. The amplitude of the tsunami wave as it propagates across deep ocean waters is commonly less than 0.5 m (Hammack, 1972) which makes it not obvious to the casual observer. As the wave arrives in shallow water it can undergo shoaling. This process can result in a wave amplitude capable of causing major coastal damage and loss of life. A tsunami that reaches a coastline is classified according to the distance it has propagated from source to inundation. A far field tsunami (also called a distant-source or tele-tsunami) is sourced more than 1000 km from the area of interest whereas a near field tsunami is sourced less than 1000 km from this area (rewritten from a tsunami glossary provided by the Pacific Environmental Marine Laboratory at the website http://www.pmel.noaa.gov/tsunami-hazard/terms.html).

One of the earliest significant tsunamis recorded was in Japan. This event was generated by the July 9, 1586 earthquake off the west coast of Peru, South America

(Satake et al., 2003). An incomplete list of significant tsunamis subsequent to this 1586 event is presented in Table 1.1. A more detailed overview of past tsunami events and their generation mechanisms can be found at:

http://www.e11thhour.org/resources/timelines/tsunami.global.html.

Year	Location of impact	Dead
1586, July 24	Peru	56
1883, August 27	Indonesia	>36,000
1896, June 15	Japan	>27,000
1933 March 3	Sanriko	3000
1946, April 1	Hawaii	159
1960, May 5	Chile	1000
1964, March 28	Alaska	131
1977, August, 19	Indonesia	180
1983, May 26	Hokkaido	104
1992, December 12	Flores Island	>2080
1993, July 12	Hokkaido	>500
1994, June 2	Java	223
1998, July 17	Papua New Guinea	>2200
2004, December 24	Sumatra	~ 216,000

Table 1.1: An incomplete list of previous significant tsunamis

The map below highlights coastal areas where tsunamis arriving at the shoreline with a height greater than 2 m have been recorded. It also includes the significant events listed in Table 1.1.

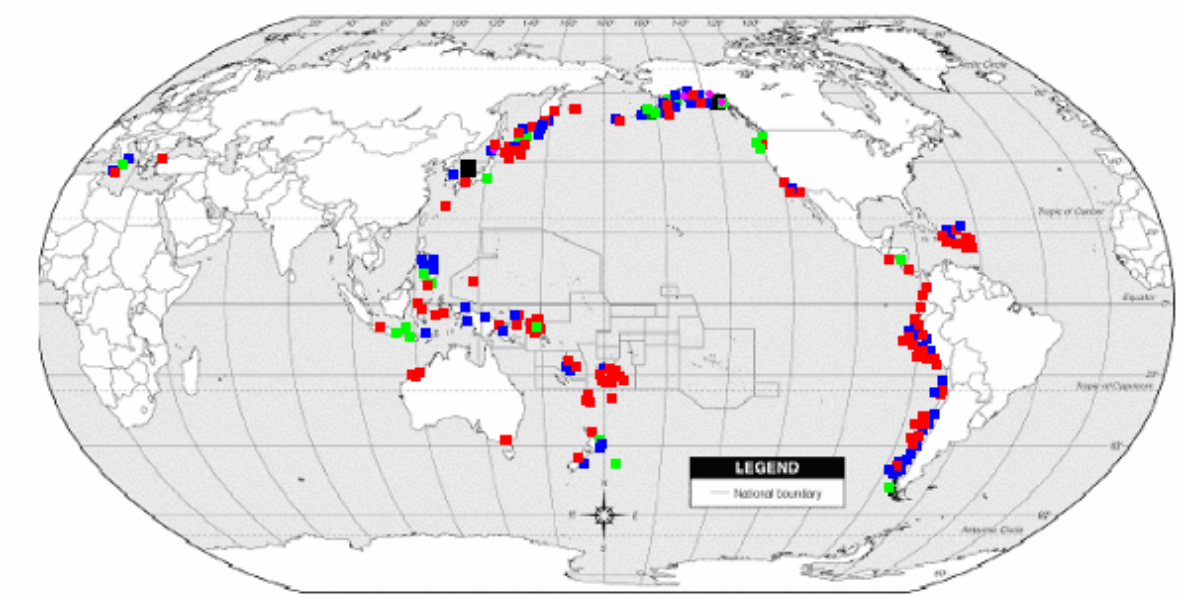

Figure 1.1: World map illustrating regions affected by tsunamis of amplitudes between: 2 and 5 m (red), 5 and 10 m (blue) and $\geq$30 m (black).

Compared to other sources of coastal damage such as monsoon flooding, historical and present day records demonstrate that tsunamis pose a real danger to coastal areas. Because of the increase in the global population and human exploitation of coastlines for reasons such as habitation, recreation and tourism, a strong public awareness of this danger is of utmost importance.

Identification of populated regions at risk to potential tsunami hazard is a key factor to the development of an effective early warning program. As is shown in Chapter 2, the majority of studies concerning tsunami hazard involve the numerical modelling of tsunami propagation. It is proposed that further work into the comparative abilities of numerical tsunami models in their application to various kinds of submarine topographies, could help in the choice of which type would best be used for this modelling.

1.1 Objective of the current research

The present work aims to assess differences between results predicted by a fully nonlinear extended Boussinesq model (with its ability to predict dispersion) and a non dispersive, linear or weakly nonlinear model in their application to modelling dispersive and non dispersive tsunami waves over a varying bathymetries, and to determine the usefulness and robustness of the geophysical application of the more computationally demanding Boussinesq model.

This work is carried out in two parts. Firstly, numerical simulations are used to highlight contributions from nonlinear and dispersive terms to the scatter of dispersive waves from single and combined idealized bathymetric features. These waves are analogous to a potential tsunami wave produced by a tsunami generating mechanism, such as a sub-marine landslide, slump or volcanic eruption.

The second part investigates the usefulness and robustness of a Boussinesq model in its application to a variety of geophysical bathymetric domains. In addition, it emphasizes any advantages and or shortcomings associated with this type of model application.

1.2 Thesis layout

Chapter 1 of this thesis outlines the significance of tsunamis and motivates the importance of understanding their propagation.

Chapter 2 contains a synopsis of previous tsunami research. In this chapter the area of tsunami research which this thesis to will contribute is defined. This is followed by motivation for the use of the numerical model Geowave V1.0 was chosen as the tool of research. Chapter 3 provides detailed information on Geowave and discusses various adaptations made to it for the purpose of this research.

In Chapter 4 the numerical results of simulations used to highlight contributions from nonlinear and extended Boussinesq terms to the scatter of a wave with dispersive properties from single idealized bathymetric features, are presented and discussed. In Chapter 5 an investigation into these contributions to scatter, from a combination of two idealized bathymetric features, is presented. Chapter 6 provides a link between the theoretical content of Chapters 4 and 5 and the geophysical world.

Chapter 7 contains an investigation into the robustness of the chosen numerical tool Geowave in its application to a variety of geophysical domains. In addition to this, a discussion of the issues surrounding the choice of numerical model based on the particular geophysical application is provided.

This thesis concludes in Chapter 8 with a brief summary of the previous chapters. This highlights the new scientific contributions to the knowledge base of numerical modelling of tsunami propagation. Also presented in this chapter are some proposals for further development of the numerical model Geowave V1.0.

Chapter 2

Tsunami Background and Literature Overview

Section 2.1 of this chapter provides a general scientific background to tsunami generation and propagation. Section 2.2 gives an overview to numerical modelling of tsunami. Section 2.3 contains a synopsis of previous tsunami research. The objective of the current research is presented in section 2.4.

2.1 Background to tsunami generation and propagation

Essential to any study of tsunamis is an appreciation on how they are produced and the physics of their propagation. Section 2.1.1 discusses tsunami generation mechanisms. Section 2.1.2 provides a general overview of the physics behind tsunami propagation.

2.1.1 Tsunami generation mechanisms

Tsunamis are a relatively common occurrence. According to the Tsunami Laboratory in Novosibirsk, between 1900 and 2001, 796 tsunamis were observed or recorded. Tsunamis can be generated by a variety of mechanisms including:

- Earthquakes
- Submarine landslides
- Sub aerial landslides
- Atmospheric coupling
- Bolide explosion
- Nuclear explosion/ detonation
- Volcanic Eruptions

A list of tsunami generation mechanisms and the deaths which resulted from each type are given below in Table 2.1.

Tsunami generation Mechanism	No. of events which have caused tsunamis	% of events	Deaths which resulted from the tsunami	% deaths
Earthquake	7,174	82.3	690,929	90.6
Landslide	65	4.6	14,661	1.9
Volcanic	65	4.6	516,43	6.8
Unknown	121	8.5	5364	0.7
Total	1422	100	762,597	100

Table 2.1: Tsunami generation mechanisms and the deaths that resulted.

It is common knowledge that earthquakes are the usual mechanism for generating tsunami. Tectonic motions which produce a tsunami normally involve a strike slip fault or a dip slip fault. A strike slip fault is a horizontal movement and a dip slip fault involves vertical movement (Chick, 1999). Records show tsunami waves produced from a strike slip fault have in most cases propagated short distances (Chick, 1999). The second most common mechanism of tsunami generation is by landslides. Landslides can take place totally underwater (submarine) or they can originate on land and the debris can flow underwater. The other mechanisms (as above) are less common, i.e. volcanic eruptions account for approximately 5% of tsunamis (de Lange and Hull, 1994).

The wavelength of a tsunami wave is directly correlated to the size of the source mechanism. For example, tsunamis generated by seismic sources depend on the earthquake magnitude, its focal depth and rupture length. Wavelengths of seismic generated tsunamis average several hundred kilometres, unlike those from sub-marine landslides and slumps which average only a few kilometres (Matsuyama et al., 1999). The generation of a

tsunami by earthquake occurs over a short time-frame i.e. seconds, not minutes. (A landslide however can take longer). The result of the short time-frame is that the initial earthquake-generated tsunami waveform will be composed of fewer frequencies components. This waveform will undergo less and often negligible dispersion (Matsuyama et al., 1999) and can propagate long distances. Dispersion is defined in section 2.1.2. Seismic generated tsunamis will radiate in all directions from the source. Landslide generated tsunamis propagate in a focused direction. This focused propagation can cause near field run-up amplitudes to be much larger than those of seismic generated tsunamis.

It is often the case that an earthquake will trigger a submarine landslide or slump that in turn generates a tsunami. An example of this is the 1958 Lituya Bay tsunami that resulted from a landslide triggered by the July 9, 1958 earthquake along the Fairweather Fault, Alaska. The initial surface displacement reached a maximum height of 516 m (Pararas-Carayannis, 1999). A second example is the tsunami produced by the 1998 combined earthquake and submarine slump at Sissano Lagoon, Papua New Guinea which killed over 2000 people (Tappin et al., 2001).

Historically, volcanic-generated tsunamis are scarce (refer to Table 2.1). However, before the December 2004 Indian Ocean event, the Krakatoa volcanic eruption of August 27, 1883 was the cause of the most damaging tsunami of all time. Despite their previously scarce occurrence, there is concern for future danger from such mechanisms. For example, the semi-enclosed Hauraki Gulf, New Zealand could be at risk to such an event from volcanoes in the Tonga-Kermadec subduction zone (de Lange and Healy, 2001). Such an event could devastate Auckland, the largest metropolitan city in New Zealand that lines the inner coastline of the Gulf. An even more catastrophic tsunami event would be from the collapse of the Cumbre Vieja Volcanoe, La Palma Canary Islands. It is estimated that this could result in the subsidence of 150 to 500 km^3 of rock into the sea, generating a wave that would arrive at the coastline of America with amplitudes ranging between 10 and 25m

high (Ward and Day, 2001). Gisler (2005) hypothesizes that in a worst-case scenario, the initial surface displacement could reach 1508 m with the greatest hazard for the immediate coastlines, i.e. those in the Canaries Archipelago and of mainland Africa and Europe.

The most common region for the generation of tsunamis is around the Pacific Rim or 'Pacific Ring of Fire'. This is due to the lithospheric plates (see Figure 2.1), the movement of which produces submarine earthquakes. Tsunamis have also been generated by earthquakes in many other ocean basins, for example, the 2004 Sumatra_andaman earthquake which generated the Indian Ocean Tsunami. This was the most destructive tsunami ever recorded and resulted from an earthquake of magnitude 9 with a rupture length of 1300 km (Titov et al, 2005).

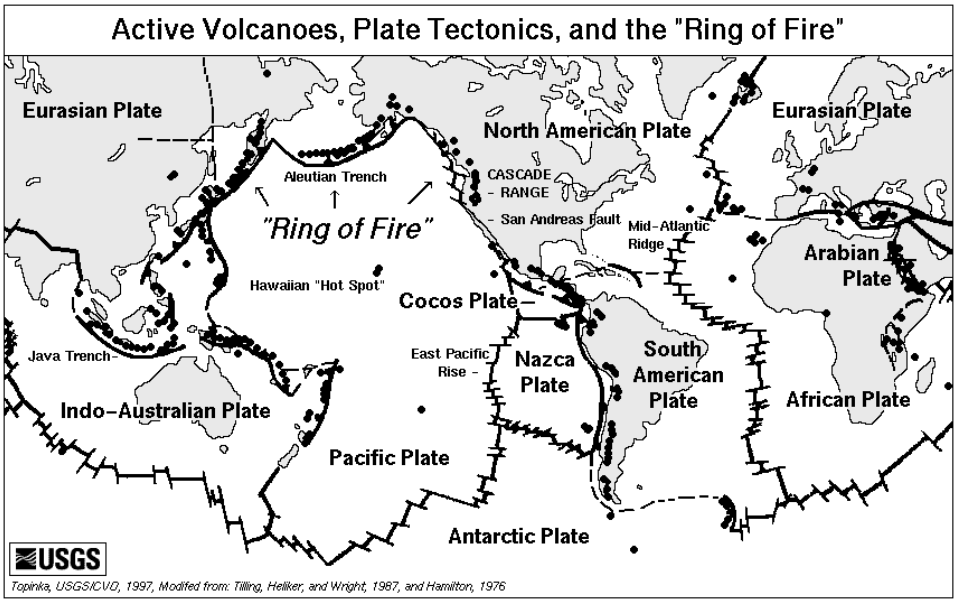

Figure 2.1: Illustration representing active volcanoes (black dots) and the lithospheric plates (black lines). Taken from Topinka (1997), USGSICVO (http://oceanexplorer.noaa.gov).

2.1.2 Physics of tsunami propagation

This section provides a brief overview on the physics of tsunami wave propagation.

An initial tsunami wave is made up of different frequency components. During the propagation process and relative to the water depth *H*, the initial waveform components may travel at phase speeds (celerities) which depend on their wavelength λ (refer Table 2.2), i.e., the various components will separate from the initial waveform and travel at their own distinctive speed. This process is known as dispersion. The result of this is that the lower frequency (longer wavelengths) components, which in deep water travel faster than high frequency components, will therefore reach the coastline first.

Depending on the ratio of the water depth (*H*) and wavelength (λ) (Table 2.2), tsunami waves are classified as either deep water waves, intermediate depth water waves or shallow water waves. The wavelength of a propagating tsunami is most often much greater than the depth of the ocean across which it propagates. It is therefore typically modelled as a shallow water wave, for which the speed is independent of T (Equation 2.3).

relative depth H/λ	wave type	wave celerity	wavelength (λ)
$H/\lambda < 0.05$	shallow water wave	$\sqrt{gH}$	$\sqrt{gH}T$
$0.05 < H/\lambda < 0.5$	intermediate depth wave	$\sqrt{\frac{g\lambda}{2\pi}\tanh\left(2\pi\frac{H}{\lambda}\right)}$	$\frac{gT^2}{2\pi}\tanh\left(2\pi\frac{H}{\lambda}\right)$
$H/\lambda > 0.5$	deep water wave	$\sqrt{\frac{g\lambda}{2\pi}}$	$\frac{gT^2}{2\pi}$

Table 2.2: Wave classification and overview of the relationship between period (*T*), wavelength (λ), depth (*H*) and celerity (*c*). Taken from Sorensen, 1992.

The wave celerity is given (Dean and Darlrymple,) by:

$$c = \frac{\omega}{k} \qquad 2.1$$

where k is the wave number defined by $k = \frac{2\pi}{\lambda}$ and ω is the wave frequency.

For a non-dispersive wave the frequency is given by:

$$\omega = \pm k\sqrt{gH} \qquad 2.2$$

where g is acceleration due to gravity of 9.8 ms^{-2} and H is water depth.

For a dispersive wave in deep water the frequency is given by:

$$\omega = \pm\sqrt{kg}\,. \qquad 2.3$$

In general it can be shown that non-dispersive shallow water waves all travel at a speed given by Equation 2.4 (Table 2.2)

$$c = \sqrt{gH}\,, \qquad 2.4$$

and that dispersive waves in deep water travel at a phase velocity independent of the depth as:

$$c = \sqrt{\frac{g}{k}}\,. \qquad 2.5$$

In the case that a tsunami wave is generated and it's wavelength is not much greater than the ocean depth, its speed is dependent on its wavenumber (Equation 2.5). Assuming an average tsunami propagation depth to be the mean depth of the Pacific Ocean (Table 2.3), a relative depth (water depth/wavelength) to be of less than 0.05 and a tsunami wave

period to be within the range between 15 minutes and 300 minutes (Walters and Goff, 2003), the corresponding wavelengths can be calculated from the wavelength equations in Table 2.2. The resulting wavelengths range between 185 km, for waves at the higher frequency end of the scale ($\omega = 2\pi / T$) and 3695 km for waves at the lower frequency end. Because the wavelength is proportional to the speed (Equation 2.1), the longer wavelength (lower frequency) components will travel fastest across the deep water reaching the coastal regions first. A Fourier analysis of a tsunami (Figure 2.2) emphasizes this by illustrating that the majority of energy that reaches a coastline is found in the lower frequency wave components.

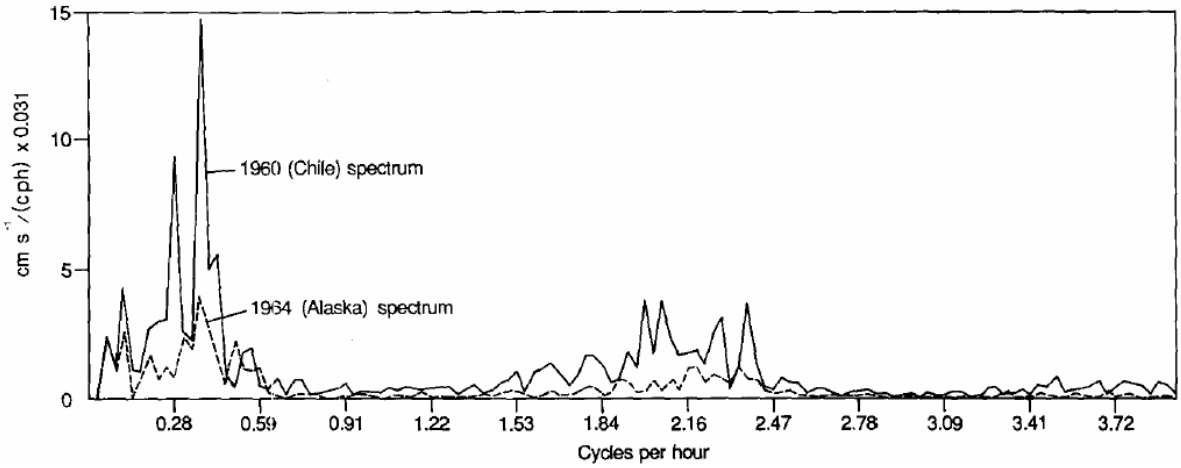

Figure 2.2: Frequency spectra for the 1960 Chile and 1964 Alaskan tsunamis in Wellington Harbour, New Zealand. The majority of energy for each tsunami is observed to occur in the lower frequency modes (Figure taken from Gilmour, 1990).

Ocean	Mean depth (km)	Maximum depth (km)
Pacific	4.3	10.9
Atlantic	3.3	8.61
Indian	3.9	7.26
Artic	1.05	4.6

Table 2.3: Mean Ocean depths. (This table was constructed based on the data provided on the public domain by Dr. Michael Pidwirny, University of British Columbia Okanagan).

Because earthquakes are the most common mechanism of tsunami generation, far field events occur more frequently and provide the possibility for a single tsunami to be a global event. Figure 2.3 shows the global reach of the 2004 Sumatra tsunami.

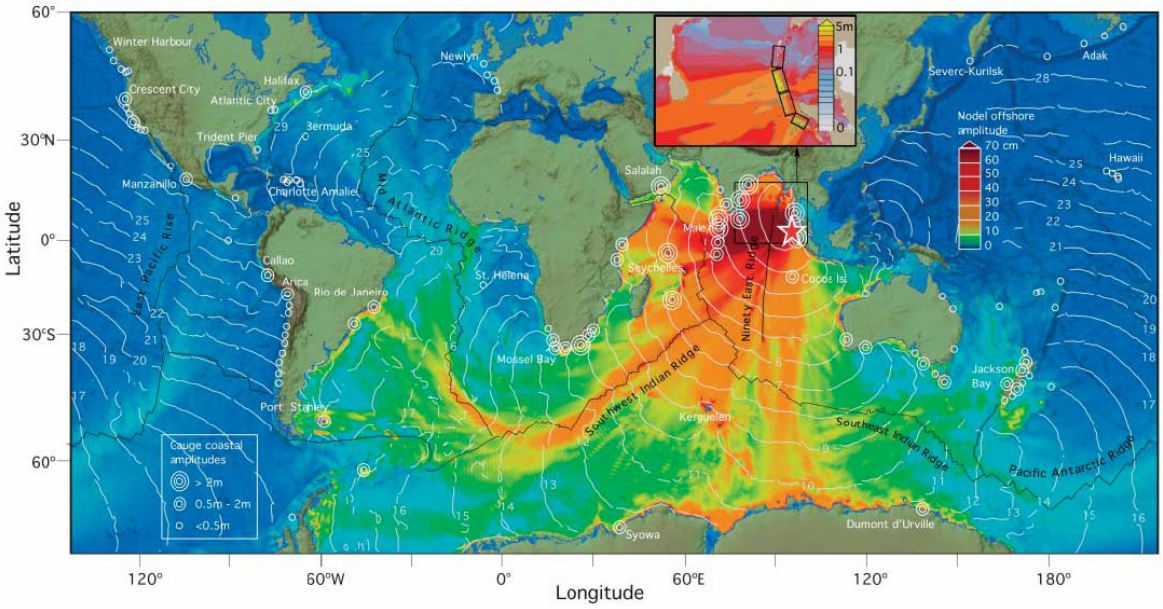

Figure 2.3: Global chart showing energy propagation of the 2004 Sumatra tsunami calculated from the numerical model MOST. Filled colours show maximum computed tsunami heights during 44 hours of wave propagation simulation. Contours show computed arrival time of tsunami waves. Circles denote the locations and amplitudes of tsunami waves in three range categories for selected tide-gauge stations. The inset shows fault geometry of the model source and a close-up of the computed wave heights in the Bay of Bengal. Distribution of the slip among four subfaults (from south to north: 21 m, 13 m, 17 m, 2 m) provides the best fit for satellite altimetry data and correlates well with seismic and geodetic data inversions. (Figure and caption taken from Titov et al., 2005).

Countries that border the Pacific Basin are particularly susceptible to far field events from different regions of the Pacific Ocean. Examples of far field events to have reached New Zealand are the 1960 Chile event. Records of this event show coastal tsunami amplitudes ranging from 25 m in Isla Mocha Chile (Abe, 1995) to 3.5 m in New Zealand (de Lange and Healy, 1986), the 1964 Alaska (de Lange and Healy, 1986; de Lange and

Fraser, 1999; de Lange and Healy, 2000) and the 1998 Papua New Guinea tsunami (de Lange and Fraser, 1999).

2.2 Numerical modelling of tsunamis

The following three subsections provide a brief introduction to numerical modelling of tsunami.

2.2.1 Motivation for the use of numerical tsunami models

The evolution of a tsunami with time is governed by partial differential equations (for further detail on these equations, refer to Chapter 3). When these equations become too complex to solve analytically, they can be solved by use of a numerical method. This type of method discretizes a numerical domain into grid elements and provides an approximation to the equations at each grid node (point that connects discretized grid elements). For further detail on the method solving the equations the reader could consult Garg (1998).

2.2.2 Numerical methods on which tsunami models are based

There are several numerical methods available for solving the partial differential equations that govern the propagation of tsunamis. For example, the finite difference method (*fdm*), the finite element method (*fem*) and the finite volume method. The first two are the most common methods. The numerical grids employed by each method are described below.

Finite difference grid:

A finite difference grid consists of uniform sized cells. Each cell has a width (Δx) and length (Δy). This uniformity is advantageous in that grid generation is simpler and that on

an equivalent number of node basis, solving with use of a structured finite difference grid requires less time. However in order to most accurately resolve the physics, an unstructured grid (finite element method) may be more efficient. Numerical models are more stable when the horizontal dimensions are similar in size (i.e. within 5%, Watts, 2002). As a result of this regularity, this type of finite difference grid is limited to applications where the domain is small, which means a high resolution can be achieved, or where the grid resolution is of a less importance. However, finite difference grids do have the possibly for a varied grid resolution through grid adaptations, i.e. nested grids. MOST (Titov and Synolakis, 1998) is an example of a numerical model that employs this technique.

Finite element grid:

A finite element grid consists of cells (elements) which are variable in size (and often triangular in shape). This is helpful for large numerical domains where a finer resolution is required in the shallower coastal waters to capture effects such as amplification, but is superfluous in the deeper water. The use of various sized triangles is advantageous over uniform sized cells (*fdm*) as they fit more precisely along a challenging boundary, such as curved coastlines. The finite element grid does however possess computational disadvantages, such as a greater time required to solve the more tedious equation sets.

2.2.3 Input data required by a numerical model

Numerical modelling can be conducted for a non-hypothetical or hypothetical tsunami. For either case the propagation model will require a set of initial conditions. These initial conditions are often developed by the input of data which describes a past event, into a program used specifically for generating initial conditions (Watts et al., 2003, Watts et al.,

2002; Heinrich et al., 2000; Tappin et al., 2001). These conditions are then used in the propagation model.

2.2.4 Which numerical equation set to use?

For computational efficiency, the majority of tsunami propagation models are based on the nonlinear or linear shallow water equations (refer to Chapter 3). This is justifiable because during propagation most tsunami wavelengths are much greater than the water depth, i.e. the horizontal scale is much larger than the vertical scale. Additional to this and according to a study's domain and focus, computational speed can be increased by the neglection of nonlinear terms. Dependent on the research question being addressed, this may have little effect on the results. For example, use of a linear shallow water model (Guibourg et al., 1997) and an extended Boussinesq model (Herbert et al., 2001) predicted a wave entering the Marquesas Archpigalieo to have approximately the same energy.

2.3 Previous tsunami research

The earliest studies of tsunamis were conducted by the Japanese around 1880. The majority of these early studies were descriptive (Hammack, 1972). The Sanriku March 3, 1933 tsunami (which killed more than 3000 people) was the stimulus of modern tsunami research (Zelt, 1986). The following overview provides an insight into the main areas of tsunami research published in English. It pays particular attention to research areas that have used a numerical approach and places the work of this thesis in context.

2.3.1 Tsunami hazard prediction for risk management

Due to the way in which bathymetry can trap tsunami wave energy, by for example, reflection or refraction, the height which a tsunami runs up (where run up is defined as the

maximum water level above a reference point, normally taken as the mean sea level position of the waters edge) can vary significantly along a coastline (Choi et al., 2002). For example, a difference of 10 m in wave amplitude was observed between two locations only 5 km apart (Gilmour and Stanton, 1990).

In order to minimise the destructive effects of tsunamis, an understanding of the possible effect of local bathymetric conditions would be required for all coastal regions. Such a study would consider potential tsunami events including the wave amplification and wave run-up specific to the coastal bathymetry of a particular region. This approach requires a clear understanding of the dynamics of tsunamis, from initial cause to resultant effect.

A number of numerical studies have been conducted which investigate tsunami hazard for risk management. Some New Zealand examples include; East coast (Walters and Goff, 2003; Barnett, 1994), Wellington (Barnett et al., 1991; Gilmour and Stanton., 1990), Canterbury and Otago (Todd, 1999), Kaikoura (Walters et al., 2006), Bay of Plenty (de Lange and Healy, 1986) and the Firth of Thames (Chick et al., 2001; de Lange and Healy, 2000; de Lange and Fraser, 1999). Other studies include; the Korean coast (Choi et al., 2001), East Japan Sea (Choi et al., 2005), Marquesas Islands (Herbert et al., 2001), French coast of the Mediterranean (Pelinovsky et al., 2002), coastal Aniva Bay (Khramushin and Shevchenko, 1994), U.S. west coast (Gonzalez, 1995), Baker Lake (U.S) (Walder et al., 2006; Borrero et al., 2001), Calabria and Eastern Sicily (Tinti, 1993) and the Canary Islands (Ward and Day, 2001; Gisler, 2005).

Analysis of historical tsunami data sets can also provide an indication of tsunami hazard. This may lead to inaccurate predictions because some data sets are incomplete. Studies that aim to complete data sets can be specific (Choi and Lee, 1993) or incorporated into a larger work (Choi et al., 1994b).

2.3.2 Use of numerical modelling in the discovery of tsunami generation mechanisms

From the literature it is clear that an important component of tsunami research is the use of numerical models in combination with historic tsunami amplitudes to reproduce a past waveform and reveal the source of its generation. This procedure is known as inverse modelling. Knowledge of the factors surrounding tsunami generation may help in the prediction of a future tsunami. For example, when a seismic fault is discovered, it can be monitored and predictions made as to when a tsunami may be generated and, its possible magnitude.

Following the 1998 Papua New Guinea (PNG) tsunami a multitude of numerical studies employed this method of inverse modelling to understand the true origin (slump source) of the large amplitude tsunami wave (Heinrich et al., 2000; Tappin et al., 2001; Synolakis et al., 2002; Watts et al., 2002). The work of Tanioka (1999) used this method to show that the 1998 PNG tsunami waveform that reached Japan was not dependent on the additional slump source found by the above authors.

This method has also been employed for numerous other tsunami events to gain a better understanding of a fault mechanism or to determine a fault's location; for example, the 1693 Sicily tsunami (Piatanesi and Tinti, 1997), the 1887 Ligerian coast tsunami (Eva and Rabinovich, 1997), the 1905 Calabrian tsunami (Tinti and Piatanesi, 2001), the 1969 Gorringe Bank tsunami (Gjevik et al., 1997), the 1975 Kalapana tsunami (Day, 1975), the 1982 Torishima tsunami (Satake and Kanamori, 1984), the 1992 Flores tsunami (Imamura et al., 1995), the 1999 Kocaeli tsunami (Tinti et al., 2006) and, the 2004 Sumatra tsunami (Geist, et al., 2006; Watts et al., 2005).

2.3.3 Effects of bathymetry on tsunami propagation and amplification

From the literature it has been observed that bathymetric features in the open ocean and offshore can significantly influence the propagation and amplification of tsunami waves. Numerical studies involving these effects of bathymetry are relatively scarce (with the exception of a number of circular island studies). Following each of the last two major tsunami events, the 1998 Papua New Guinea tsunami and the 2004 Indian Ocean tsunami, a large number of numerical studies emerged. Of these however, only a few investigated bathymetric influences. A numerical study that investigated the influence of mid ocean topography on tsunami waves is that of Titov et al. (2005) which showed mid-ocean ridge topographies caused wave trapping and focusing of the 2004 Indian Ocean tsunami. Narayan et al. (2005) concluded from the 2004 Indian Ocean event that the continental shelf width played a major role in the pattern of tsunami damage in the two Indian districts of Nagapattinam and Kanyakumari. Matsuyama (1999) presents evidence that offshore bathymetry played a critical role in the behavior of the 1998 PNG event. A further study on the effect of a continental shelf is that by de Lange (1983). This suggests that the impact of a far-field tsunami is dependent on the energy that is transmitted as it crosses a continental shelf. It also suggests that up to 40% of wave energy may be reflected by the continental slope to the east of New Zealand.

As mentioned above, the literature contains a number of numerical studies that investigate how the presence of a circular island affects the run-up and or amplification of tsunami waves. These studies include those which investigated the role circular bathymetry plays in focusing tsunamis (Matsuyama et al., 1999; Nakamura, 2006), and tsunami run-up at circular islands (Liu et al., 1994; Choi and Liu, 1999; Briggs et al., 2000). Further island studies include Herbert et al. (1999) which examined the impact of the Kurile 1994, Chile

1995, Mexico 1995 and Peru 1996 tsunamis in order to understand the amplification phenomena observed in the Marquesas Islands.

There also exist a limited number of theoretical and analytical studies that investigate how bathymetry affects the propagation and amplification of a tsunami. For example, Weber's integral technique (Sandoval & Farreras, 1993) was used to show how resonance in the Gulf of California affects tsunami amplification. Tinti and Vannini (1995) used a theoretical means to understand the influence a circular island has on wave amplification. Two analytic studies investigate tsunami scatter from bathymetric features. The first study (Koshimura et al., 1999) provides fundamental solutions to the scatter of tsunamis from an idealized ridge. The second study (Mofjeld et al., 2000) does the same for a range of idealized bathymetries. Application of the latter to geophysical bathymetry can be seen in Mofjeld et al. (2001) and Titov (1999) respectively.

2.3.4 Validation of numerical models

Numerical models require mathematical formulations that can accurately model wave evolution as the tsunami propagates over a diverse range of water depths (Wei et al., 1995). The desire to obtain a greater and greater accuracy in predicting tsunami wave propagation as well as faster computational speeds provides motivation for the modification of mathematical equation sets. In order to draw concise quantifiable conclusions from numerical predictions, validation of these models is imperative.

The history behind the validation of long wave run up (shallow water) models began with the first international workshop on long wave run up models held at Catalina Island 1990. The proceedings are reported in Liu et al. (1991). Since then, two further workshops on this topic have been held. One in 1997 (Synolakis, 1997) the other in 2004, refer to www.cee.cornell.edu/longwave/index.cfm?page=background. One method of

model validation is by the comparison of one numerical model with another. Some examples of intercomparison between long wave models can be seen in: Watts et al. (2003), Chick and de Lange (1999), Imteaz and Imamura (2001) and Walters (2005).

Another method of validation is the comparison of model results against observational data (e.g. Chen et al., 2000; Horrillo et al., 2005; Lynett and Liu, 2002; Walters, 2005; Walters and Goff, 2003; Kowalik and Whitmore, 1991). Kowalik and Whitmore (1991) used this method to show that for propagation distances across the equator, the inclusion of the Coriolis force may be required. A numerical simulation of the 2004 Indian Ocean event showed wave trapping which was partly attributable to the Coriolis force (Kowalik et al., 2005).

Alternatively, numerical results can be compared against experimental results from a benchmark case. In the field of tsunami research, a benchmark case is a laboratory experiment in which the bathymetry or experimental scenario is analogous to that which a tsunami may encounter as it propagates across the ocean. Popular benchmark cases are those presented in Beji and Battjes (1993), Watts et al. (2000) and Briggs et al. (1995).

The intercomparison of model results is important to help accurately describe tsunamis according to the physical parameters surrounding their propagation, i.e. source mechanism, water depth, path of travel. One method of developing this understanding is to compare model results with the inclusion and exclusion of certain terms, for example, with and without nonlinear terms (Satake, 1995; Imteaz and Imamura, 2001; Chick and de Lange, 1999) or with and without fully nonlinear and dispersive terms (Lynett et al., 2003; Sato, 1995).

Although the incorporation of a sufficient number of terms which describe wave behaviour is required to accurately model tsunami propagation, it is imperative that there are models available that are not excessive in computational time. This is of particular importance when tsunami predictions are required for immediate tsunami warnings.

Following the 2004 Indian Ocean event, two numerical models were compared against observed global tsunami arrival times in order to find models that would be effective for a Disaster Alert System. These models were MOST (Titov and Synolakis, 1998) and the INGV model (A. Piatanesi, Istituto Nazionale di Geofisica e Vulcanologia, Rome, Italy). Comparisons found that although all three models predicted real time tsunami arrivals relatively well, they were computationally too slow to be effective in a Disaster Alert System. (Annunziato and Best, 2005).

2.4. Overview on the choice of numerical modelling tool

To carry out the research needed to fulfil the purpose of this thesis, a numerical model was required. This section presents an overview of numerical models able to simulate tsunami propagation. It concludes with the model chosen for this thesis.

There are a number of different theoretical approaches upon which numerical models are based. Models which impose the hydrostatic approximation include; the linear model TUNAMI (Imamura, 1995), the nonlinear models TUNAMI-N2 (Imamura, 2004), SI3D (Smith, 1997), RIF/DIF (Kirby and Dalrymple, 1985), RiCOM with shallow water limit (Walters, 2005), 3DD (Black, 1995) and, MOST (Titov and Synolakis, 1998) and also models based on the Boussinesq equations which include FUNWAVE (Chen et al., 2000; Kennedy et al., 2000), Geowave (Watts, 2002) and COULWAVE (Lynett and Liu, 2002).

A limited number of non-hydrostatic models also exist and include the full Navier Stokes method used by TUNA-VOF2D (Horrillo et al., 2005) and the Reynolds-averaged Navier-Stokes model RiCOM (Walters, 2005).

A propagation model must be chosen in order to match specific modelling needs with the individual research question. The main factors to be considered in the choice of a numerical tool are: the source of the tsunami (near or far field) which provides an indication of the tsunamis wavelength; the characteristics of the region to be modelled,

properties of the wave, i.e., whether it is dispersive or non-dispersive, linear or non linear, whether the initial water displacement is instantaneous, and whether run up or inundation is to be considered.

Characteristics of the region are important for determining a regions influence on the aforementioned factors. For example, the depth to horizontal length ratio of a region influences which numerical method (*fdm* or *fem*) will be best (for further detail refer to section 2.2). The depth can also dictate the properties of a wave i.e., nonlinear or dispersive. If the wave amplitude for a region divided by the water depth is much less than 1, nonlinear terms can be neglected. If however, this is not the case, nonlinear terms should be included (further detail on nonlinear terms is given in Chapter 3). The decision whether or not to include the effects of dispersion depends both on the wavelengths produced from the tsunami generation mechanism and on the region's water depth. This decision can also be influenced by the propagation distance. For example, Heinrich et al. (2000) assume that due to a short propagation distance, components of the wave packet have not had significant time to disperse and thus waves can be treated as non dispersive. However, near field simulations which have included dispersive terms (e.g. Lynett et al, 2003; Watts et al., 2003) show they have a significant effect. A region's size also dictates the co-ordinate form of the applicable model. For models which neglect curvature (i.e. those in local Cartesian co-ordinates) are best applied to regions across which the latitude varies by less than a few tens of degrees.

Table 2.4 lists the models considered (and their attributes) in the choice of numerical model for this thesis. The chosen model is the fully nonlinear, two-dimensional, finite-difference, extended Boussinesq model Geowave V1.0 (GW) (Watts, 2002). GW is the combination of the propagation model FUNWAVE (FW) (Chen et al., 2000; Kennedy et al., 2000) and the Tsunami Open and Progressive Initial Conditions System V1.2 (TOPICS) (Watts, 2002). Motivation for the use GW, comes firstly through an interest in

the advantages of the extended Boussinesq equations, and secondly through its ease of availability at no cost on the internet.

The advantage of the propagation component FW is its predictor corrector scheme for time-stepping, in which first order spatial derivatives are discretized to 4^{th} order accuracy. This eliminates leading order truncation error terms that would otherwise be the same size as the dispersive terms in predicting wave propagation across relatively deep water. Modifications made to FW during the development of GW meant that GW was restricted to the fully nonlinear extended Boussinesq equation set of FW. For further details on these modifications refer to Chapter 3.

	Geowave	FUNWAVE	TSUNAMI	TSUNAMI-N2	3DD	REF/DIF	MOST	COUL-WAVE	RiMA10	ADCIRC	TUNA-VOF2D	RiCOM	SI3D
Hydrostatic	x	x	x	x	x	x	x	x	x	x			x
Non-hydrostatic											x	x	
Linear			x										
Non-linear	x	x		x	x	x	x	x	x	x		x	x
Full Navier Stokes											x		
Boussinesq													x
Boussinesq extended	x	x						x					
2D	x	x	x	x				x				x	
3D					x	x	x		x	x	x		x
Finite difference	x	x		x	x	x	x	x					x
Finite element			x						x			x	
Available on the public domain	x	x				x		x		x			

Table 2.4: List of Models considered and their attributes.

Chapter 3

The Numerical Model Geowave V1.0

Geowave (GW) (Watts, 2002), is a two dimensional, depth integrated, finite difference model made up of the Tsunami Open and Progressive Initial Conditions System TOPICS V 1.2 (Watts, 2002) and the propagation code of FUNWAVE. It is set up to use a fully nonlinear, extended Boussinesq equation set. Its use as the numerical tool for this thesis is motivated by its Boussinesq equation set and its availability free of charge, on the public domain. At the time this thesis was written there was no available manual specifically for Geowave.

The following chapter provides an overview of GW. Section 3.1 examines the mathematical scheme and its modifications made to the equation sets for the purpose of this thesis. Section 3.2 provides a brief overview of the finite difference scheme. The boundary and initial conditions are given in sections 3.3 and 3.4. Section 3.5 discusses the causes of instability in GW.

3.1 The mathematical scheme and modified equation sets of Geowave

3.1.1 Background theory to the development of Geowave

GW, like most numerical tsunami models, was developed based on the two dimensional shallow water equations for nonlinear non dispersive wave propagation. These equations are obtained by neglecting dispersive terms in the Navier Stokes equations. (The linear shallow water equations are obtained by neglecting both nonlinear and dispersive terms).

Because the derivation of these equations is already published numerous times throughout the literature this work does not re derive them but instead the reader is referred to Stoker (1957) and the standard assumptions made in their derivation are as presented as follows:

(1) The effects of friction are negligible and therefore flow is assumed inviscid.

(2) The flow is irrotational

(3) The horizontal scale is much larger than the vertical scale, i.e. $H << \lambda$

(4) The pressure is assumed to be hydrostatic

(5) The fluid is incompressible

Despite the computational efficiency of the nonlinear, non dispersive shallow water equations, there are limitations. Firstly, their application is restricted to when the horizontal scale is greater than the vertical, i.e. the wavelength is much greater than the water depth so that the ratio of water depth to wavelength is less than 0.05 and the vertical velocity of the wave crest can then be assumed insignificant. Secondly, for intermediate and shallower coastal water depths, non linear behaviour such as shoaling can cause a significant increase in the wave amplitude. The effect of this is a steeper wave-front. Additional nonlinear terms are required in order to describe this. (The consequence of the steeper wave means the vertical velocity and acceleration increase, therefore reducing the accuracy to which the hydrostatic approximation holds). Finally, models based on the shallow water equations are not always capable of accurately modelling waves near the source. This is because deep water waves may occur in this region. As defined in Chapter 2, these waves can undergo dispersion. In order to satisfy all three of the above conditions, an effective propagation model should accurately simulate wave evolution from deep water through to the surf zone (Wei and Kirby, 1995).

3.1.2 The fully nonlinear, extended Boussinesq equations of Geowave

The most fundamental Boussinesq equations introduce low order terms into the dispersion relation in the nonlinear or linear shallow water equations by expansion of the horizontal velocities about a fixed point in the vertical. This introduces weakly dispersive terms to the shallow water equations. Two of the first Boussinesq models to use this method in combination with the linear shallow water equations are those of Peregrine (1967) and Madsen and Sørensen (1992). Making the assumptions (1-4) in section 3.1.1 Nwogu (1993) begins with the continuity equation and Euler equations of motion (Navier Stokes equations for inviscid motion) and develops a set of nonlinear Boussinesq equations using an arbitrary level velocity (instead of the depth averaged velocity). The arbitrary level z_α = 0.531 H (where H is the still water depth) is obtained from $\alpha = (z_\alpha / H)^2 / 2 + (z_\alpha / H)$, where α = -0.390. This value of α was chosen by Nwogu (1993) on the basis that it provides a solution to the expanded dispersion relation (Equation 3.1) that is much closer to the solution of the dispersion equation ($\omega^2 = gk \tanh(kH)$) in intermediate depths, than the depth averaged velocity does.

$$c^2 = \frac{\omega^2}{k^2} = gH\left[\frac{1-(\alpha+1/3)kH^2}{1-\alpha(kH^2)}\right] \qquad 3.1$$

The dispersion equation was then extended by Wei et al. (1995) and fully nonlinear terms were retained. The approach of Wei et al. (1995) is different to that of Nwogu (1993) in that the derivation of the extended Boussinesq equations begins with a boundary value problem for inviscid irrotational flow. The equations from the boundary value problem can then be used to give the Laplace equation and Bernoulli's equation. These equations are later used to arrive at the conservation of mass and conservation of momentum equations.

In order to reduce the dimensionality of the boundary value problem, horizontal velocities are expanded about the seabed. Wei et al. (1995) followed the method of Nwogu (1993) and replace, in this case, the value of the velocity potential at the sea bed, for the value of the velocity potential at an arbitrary depth. The velocity potential can then be substituted into the conservation of mass and momentum equations and dispersive (μ) and nonlinear (δ) terms of up to 4th order were retained. Based on this equation set, the fully nonlinear, extended Boussinesq, two dimensional, finite difference model FUNWAVE was developed. The fully nonlinear, weakly dispersive equations of Wei et al. (1995) consist of the conservation of mass equation (3.2) and conservation of momentum equation (3.3) as follows:

$$\eta_t + \nabla.\left\{(H+\eta)\left[\underline{u}_\alpha + \left(z_\alpha + \frac{1}{2}(H-\eta)\right)\nabla(\nabla.(H\underline{u}_\alpha)) + \left(\frac{1}{2}z_\alpha{}^2 - \frac{1}{6}\left(H^2 - H\eta + \eta^2\right)\right)\nabla(\nabla.\underline{u}_\alpha)\right]\right\} = 0 \qquad 3.2$$

$$\begin{aligned}
&\underline{u}_{\alpha t} + (\underline{u}_\alpha.\nabla)\underline{u}_\alpha + g\nabla\eta + z_\alpha\left\{\frac{1}{2}z_\alpha\nabla(\nabla.\underline{u}_{\alpha t}) + \nabla(\nabla.(H\underline{u}_{\alpha t}))\right\} \\
&+ \nabla\left\{\frac{1}{2}\left(z_\alpha{}^2 - \eta^2\right)(\underline{u}_\alpha.\nabla)(\nabla.\underline{u}_\alpha) + \frac{1}{2}\left[\nabla.(H\underline{u}_\alpha) + \eta\nabla.\underline{u}_\alpha\right]^2\right\} \\
&+ \nabla\left\{(z_\alpha - \eta)(\underline{u}_\alpha.\nabla)(\nabla.(H\underline{u}_\alpha)) - \eta\left[\frac{1}{2}\eta\nabla.\underline{u}_{\alpha t} + \nabla.(H\underline{u}_{\alpha t})\right]\right\} = 0
\end{aligned} \qquad 3.3$$

where η is the surface elevation, H is the still water depth, $\underline{u}_\alpha$ is the horizontal velocity vector at the water depth $z = z_\alpha = 0.531H$, $\nabla = (\partial/\partial x, \partial/\partial y)$ is the horizontal gradient operator, g is the gravitational acceleration and the subscript t denotes the partial derivative with respect to time.

Equations 3.2 and 3.3 express the progression of non-breaking waves over a smooth and impermeable bottom. These equations were rewritten in the FUNWAVE user manual (Kirby et al., 1998) to include coefficients for bottom friction, wave breaking and subgrid lateral turbulent mixing. Given the existing discrepancies in the grouping of

mathematical terms between the 'funwave' component of the GW code and the FUNWAVE manual with regards to grouping of the mathematical terms, Equations 3.2 and 3.3 are rewritten as Equations 3.4, 3.5 and 3.6 to include various physical effects and to represent their form as found in GW. These effects are wave breaking (F_{br} (3.19) and G_{br} (3.20), defined at the end of this section) and boundary absorption (F_{sp} (3.21) and G_{sp} (3.22), defined in section 3.3.1) and bottom friction (F_b).

$$\eta_t = E(\eta,u,v) + E_2(\eta,u,v) \tag{3.4}$$

$$[U(u)]_t = F(\eta,u,v) + [F_1(v)]_t + [F_2(\eta,u,v)] + F^t(\eta_t,u_t,v_t) + F_{br} + F_b \tag{3.5}$$

$$[V(v)]_t = G(\eta,u,v) + [G_1(v)]_t + [G_2(\eta,u,v)] + G^t(\eta_t,u_t,v_t) + G_{br} + G_b \tag{3.6}$$

$U, V, E, E_2 F, F_1, F_2, G, G_1, G_2, F^t$ and G^t are functions of η, u, v, u_t or v_t (where $u, v,$ are the horizontal velocity components at z_α) and are defined by Equations 3.7 to 3.18.

$$U = u + H\left[b_1 H u_{xx} + b_2 (Hu)_{xx}\right] \tag{3.7}$$

$$V = v + H\left[b_1 H v_{yy} + b_2 (Hv)_{yy}\right] \tag{3.8}$$

where 3.7 and 3.8 represent the LHS of 3.5 and 3.6.

$$\begin{aligned} E = &-\frac{1}{\kappa}\left[(\Lambda u)_x (\Lambda v)_y\right] \\ &-\left\{a_1 H^3 (u_{xx} + v_{xy}) + a_2 H^2\left[(Hu)_{xx} + (Hv)_{xy}\right]\right\}_x \\ &-\left\{a_1 H^3 (u_{xy} + v_{yy}) + a_2 h^2\left[(Hu)_{xy} + (Hv)_{yy}\right]\right\}_y \end{aligned} \tag{3.9}$$

The parameters κ and Λ are for the moving shoreline 'slot technique' (Tao., 1983 and 1984) used for run up and are defined in (Kennedy et al., 2000). Their values for the research of this thesis, where run up is not considered and the slot technique is deactivated, are $\kappa = 1$ and $\Lambda = H + \eta$.

$$F = -g\eta_x - \gamma\left(uu_x + vu_y\right) \tag{3.10}$$

$$G = -g\eta_y - \gamma\left(uv_x + vv_y\right) \tag{3.11}$$

$$F_1 = -H\left[b_1 Hv_{xy} + b_2\left(Hv\right)_{xy}\right] \tag{3.12}$$

$$G_1 = -H\left[b_1 Hu_{xy} + b_2\left(Hu\right)_{xy}\right] \tag{3.13}$$

The following functions (3.14 to 3.18) are associated with the fully nonlinear extended Boussinesq terms.

$$\begin{aligned} E_2 = &-\left\{\left[a_1 H^2\eta + \frac{1}{6}\eta\left(H^2 - \eta^2\right)\right]\left(u_{xx} + v_{xy}\right)\right\}_x - \left\{\left[a_2 H\eta - \frac{1}{2}\eta\left(H+\eta\right)\right]\left[\left(Hu\right)_{xx} + \left(Hv\right)_{xy}\right]\right\}_x \\ &-\left\{\left[a_1 H^2\eta + \frac{1}{6}\eta\left(H^2 - \eta^2\right)\right]\left(u_{xy} + v_{yy}\right)\right\}_y - \left\{\left[a_2 H\eta - \frac{1}{2}\eta\left(H+\eta\right)\right]\left(Hu\right)_{xy} + \left(Hv\right)_{yy}\right\}_y \end{aligned} \tag{3.14}$$

$$\begin{aligned} F_2 = &-\left\{\frac{1}{2}\left(z_\alpha{}^2 - \eta^2\right)\left[u\left(u_x + v_y\right)_x + v\left(u_x + v_y\right)_y\right]\right\}_x \\ &-\left\{\left(z_\alpha - \eta\right)\left[u\left[\left(Hu\right)_x + \left(hv\right)_y\right]_x + v\left[\left(Hu\right)_x + \left(Hv\right)_y\right]_y\right]\right\}_x - \frac{1}{2}\left\{\left[\left(Hu\right)_x + \left(Hv\right)_y + \eta\left(u_x + v_y\right)\right]^2\right\}_x \end{aligned} \tag{3.15}$$

$$\begin{aligned} G_2 = &-\left\{\frac{1}{2}\left(z_\alpha{}^2 - \eta^2\right)\left[u\left(u_x + v_y\right)_x + v\left(u_x + v_y\right)_y\right]\right\}_y \\ &-\left\{\left(z_\alpha - \eta\right)\left[u\left[\left(Hu\right)_x + \left(Hv\right)_y\right]_x + v\left[\left(Hu\right)_x + \left(Hv\right)_y\right]_y\right]\right\}_y - \frac{1}{2}\left\{\left[\left(Hu\right)_x + \left(Hv\right)_y + \eta\left(u_x + v_y\right)\right]^2\right\}_y \end{aligned} \tag{3.16}$$

$$F^t = \left\{\frac{1}{2}\eta^2\left[\left(u_t\right)_x + \left(v_t\right)_y\right] + \eta\left[H\left[\left(u_t\right)\right]_x + \left[h\left(v_t\right)\right]_y\right]\right\}_x \tag{3.17}$$

$$G^t = \left\{\frac{1}{2}\eta^2\left[\left(u_t\right)_x + \left(v_t\right)_y\right] + \eta\left[H\left[\left(u_t\right)\right]_x + \left[H\left(v_t\right)\right]_y\right]\right\}_y \tag{3.18}$$

For a better understanding of the following sections, several of the alterations which were made to FW in its implementation into GW are listed below:

- the linear approximation that assumed that the wave elevation is ‘usually’ smaller than the water depth was removed
- boundaries were made open and radiative

- surface elevation and its associated horizontal velocities are truncated to zero at the boundaries
- parameters such as the sponge layer width (refer to section 3.3.1) and the high energy filter application frequency (refer to section 3.3.2) were hardwired in
- the choice of viscous damping and absorbing sponge layer boundary conditions were removed
- the frame for time dependent initial conditions was removed
- all initial conditions are read in as ASCII files

Wave breaking in Geowave

Wave breaking in GW remains unchanged from that implemented into FW by Kennedy et al. (2000). The introduction of wave breaking into FW is significant as it allows the application of both FW and GW to regions within the surf zone. Energy dissipation (due to wave breaking) is modelled by the introduction of the momentum mixing terms F_{br} and G_{br} (Chen et al., 2000). This provides a more realistic onset and finish of a wave breaking.

$$F_{br} = \frac{1}{H+\eta}\left[\left(\nu\left((H+\eta)u_\alpha\right)_x\right)_x + \frac{1}{2}\left(\nu\left(\left((H+\eta)u_\alpha\right)_y + \left((H+\eta)v_\alpha\right)_x\right)\right)_y\right] \qquad 3.19$$

$$G_{br} = \frac{1}{H+\eta}\left[\frac{1}{2}\left(\nu\left(\left((H+\eta)v_\alpha\right)_x + \left((H+\eta)u_\alpha\right)_y\right)\right)_x + \left(\nu\left((H+\eta)v_\alpha\right)_y\right)_y\right] \qquad 3.20$$

where ν is the eddy viscosity localized on the front face of the breaking wave.

This method does not model the physical curling and breaking process but predicts when the frictional drag will reach a maximum value that causes the wave to break. Following the breaking of a wave, additional terms to compensate for energy dissipation are included; refer Chen et al. (2000) for further detail.

3.1.3 Obtaining different equation subsets from Geowave

To aid in the research conducted for this thesis, Geowave was adapted to enable it to calculate wave propagation based on two further equation sets. The coefficients $\gamma, a_1, b_1, a_2, b_2$ and the parameter '*ibe*' can be used to manipulate Equations 3.4, 3.5 and 3.6 to allow GW to propagate waves based on the fully nonlinear extended Boussinesq equations (GWB), the nonlinear non dispersive shallow water equations (GWS) and the linear non dispersive equations (GWL). Outlined in the table below are the values for these coefficients and that of 'ibe' needed to obtain the different subsets of GW. For the reader who is not familiar with the Geowave code, please note that γ is defined in the code as 'clnr'.

Equation subset	ibe	γ (clnr)	Boussinesq coefficients (a_1, b_1, a_2, b_2)	Functions calculated for the specific ibe value
GWB	2	1	all coefficients active	E2, F2, G2, Ft & Gt, U, V, E, G, G, F1, G1,
GWS	4	1	0	U, V, E, F, G,
GWL	5	0	0	U, V, E , F, G, F1, G1,

Table 3.1 Coefficient values used to switch between solving equation subsets of Geowave (GW)

Subroutines where equations are solved

Equations 3.4 to 3.11 are solved irrespective of the given value of '*ibe*' and '*clnr'*. Equations 3.12 to 3.18 are solved only for the condition *ibe* = 2. The subroutines where all of the Equations 3.4 to 3.18 are solved are outlined in the table below.

Function	Subroutine solved in	Solved when
4	etsol	ibe = 2, 4, 5
5 to 6	eval_utvt	ibe = 2, 4, 5
7 to 8	unsol & vnsol	ibe = 2, 4, 5
9	eval_e	ibe = 2, 4, 5
10 to 11	eval_fg	ibe = 2, 4, 5
12 to 13	eval_fg	ibe = 2
14	eval_e2	ibe = 2
15 to 16	eval_f2g2	ibe = 2
17 to 18	eval_ftgt	ibe = 2

Table 3.2: Function calculated for a particular 'ibe' value, and the subroutine in which it is calculated.

3.2 Finite difference scheme

The equations of GW are solved using the fourth order composite Adams Bashforth-Moulton finite difference scheme, discussed in detail by Wei et al. (1995). This scheme utilizes a 3^{rd} order Adams-Bashforth predictor step and a 4^{th} order Adams-Moulton corrector step. First order spatial terms are differenced to 4^{th} order accuracy. This means that all errors in the nonlinear shallow water equations are reduced to fourth order in the grid spacing and time step size. Spatial and temporal differencing of the higher order nonlinear dispersive terms is done to second order accuracy. The outcome of this is that the truncation errors (used to determine the error between the approximate and true solution of a partial differential equation) are smaller than the dispersive terms (Wei et al., 1995).

3.3 Geowave's boundary conditions

Boundary conditions are used in numerical simulations to control the flux at the outer edges of a numerical domain. The following sections 3.3.1 and 3.3.2 discuss the choice of boundary conditions available in GW and the alternative methods which it employs for removal of excess energy at the boundaries.

3.3.1 Choice of Geowave boundary conditions

As previously mentioned in section 3.1.2, in the development of GW, open radiation boundary conditions were hardwired into the code and the coefficients ω_2 (viscous damping) and ω_3 (sponge filter) that existed in FUNWAVE have been eliminated from the artificial damping terms of F_{sp} and G_{sp} (Equations 3.21 and 3.22). Nonetheless, Newtonian cooling remains.

$$F_{sp} = -\omega_1(x, y)u \qquad 3.21$$

$$G_{sp} = -\omega_1(x, y)v \qquad 3.22$$

where

$$\omega_1(x, y) = c_1 \omega f(x) \qquad 3.23$$

c_1 is the coefficient controlled by the GW parameter '*cspg*' and $\omega = 2\pi / k$, where k is the wave number and

$$f(x) = \frac{\exp[(x - x_s)/(x_l - x_s)]^2 - 1}{\exp(1) - 1} \qquad x_s < x < x_l \qquad 3.24$$

The parameter x_s denotes the start of the damping layer and x_l the end of the damping layer. The width of the layer is normally between two and three wavelengths (Wei et al., 1995) and is controlled by the parameter 'ispg' in GW. The best compromise between numerical stability and computational power is achieved when the value of '*ispg*' is

equivalent to two wavelengths. However, depending on the degree to which a wave interacts with the boundary throughout a simulation, an increase or a decrease in '*ispg*' may be necessary. The sponge layer is removed when the value of '*ispg*' is 1. This damping technique is applied in the GW subroutine 'funwave'.

3.3.2 Alternative methods of energy removal used in Geowave

Energy filters within GW that can be used alone, or in addition to the above boundary conditions, are as follows; a high energy (short wave) filter (subroutine fltr), a lateral boundary filter (subroutine fltr1) and a slot filter (subroutine fltr3). The latter is associated with run up and is therefore not relevant to the present study.

The high energy and lateral boundary filters

The high energy and lateral boundary filters both employ the same algorithm with the exception that the latter contains additional smoothing coefficients. The general filter, upon which they are both based, is designed to remove short, high energy wavelengths that develop from nonlinear interactions during the simulation process. The minimum wavelength allowed by GW to propagate is twice the grid resolution (Wei et al., 1995) and regardless of GW's improved dispersion relation, modelling of these short wavelengths is still invalid due to the large depth to wavelength ratio (Wei et al., 1995).

Equation 3.25 is adapted from the method of Shapiro (1970) by (Wei et al., 1995). It is fourth order and calculates a new filtered value at each node using a weighted average method spread over 9 nodes. If fewer than 9 nodes exist across the numerical domain, amplitudes will be dampened. New filtered values are determined at each node by

$$Z_i^* = \frac{1}{256}\left[186Z_i + 56\left(Z_{i+1} + Z_{i-1}\right) - 28\left(Z_{i+2} + Z_{i-2}\right)\right] \qquad 3.25$$

where Z^* represents the new filtered values and Z (a function of η and u) is a combination of the long and short wave components.

Application of the filter is governed by a response function (R) defined as

$$R = \left\{1 - \sin^8\left[\pi / \left(L_x / dx\right)\right]\right\}\left\{1 - \sin^8\left[\pi / \left(L_y / dy\right)\right]\right\} \qquad 3.26$$

where L_x and L_y represent the wavelengths in the x and y directions respectively. Figure 3.1 illustrates that as the ratio of the wavelength to an individual grid cell dimension (*dx* or *dy*) increases, so does the value of *R*. This results in a reduction of the filter effect. For example, when the ratio of wavelength to grid spacing is two, *R* is zero and the complete filter effect is applied.

The high energy filter is applied to the entire simulation domain at a time step frequency controlled by the GW parameter '*itftr*'. For example, for *itft* = 20, the high energy filter will be applied to the simulation domain once every 20 time steps. The lateral boundary filter is activated when the GW parameter '*idft*'=1 and deactivated when '*idft*'=0.

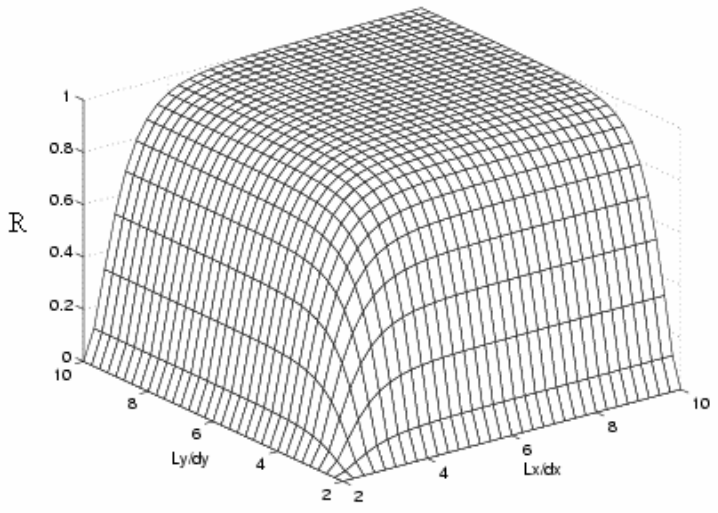

Figure 3.1: Response function (*R*) of the 2-D 9x9 point filter (taken from Kirby et al., 1998).

Regardless of the energy removal technique employed, surface elevation and horizontal velocities are truncated at the boundary in the GW subroutines bcet, bcu and bcv.

3.4 Geowave initial conditions

A numerical model requires the input of certain data for its initialization. The files required by GW are; the bathymetric data, the initial surface displacement and the horizontal velocity profiles in the horizontal directions. The initial surface must be internal to the domain. Time independent boundary conditions often necessitates the extension of the numerical grid to incorporate the length of a wave or wave train. The majority of simulations within this thesis use a monochromatic sinusoidal wave or wave-train to represent a tsunami wave. These sinusoidal waves are developed using either the 'design wave tsunami' (see below) mechanism within TOPICS (refer section 3.4.1 below) or MATLAB.

3.4.1 TOPICS initial conditions tool

The Tsunami Open and Progressive Initial Conditions System TOPICS V1.2 (Watts, 2002) approximates initial water surface elevations and velocities for use in tsunami propagation models. TOPICS allows a wave to be generated by the following six mechanisms; co-seismic displacement, submarine translational slide, submarine rotational slump, sub-aerial landslide, pyroclastic flow and design wave tsunami. A combination of up to 9 sources can be chosen. As the latter is used frequently for the present study, a simple flowchart depicting the subroutines it calls is provided in Appendix A. This flowchart indicates minor modifications made which allow the user to input initial files and bypass TOPICS.

The 'design wave tsunami' mechanism develops a finite tsunami wave-train in the GW subroutine 'wave'. The wave-train can be composed of waves that are deep water, intermediate depth, or shallow water waves, defined in Table 2.2. The wave-train can enter from any angle. In the case that it enters perpendicular to a domain edge, its length will

extend along the whole of that edge. The 'design wave tsunami' component of TOPICS was modified so that it could produce an internal initial wave-train such that the boundary conditions could be applied to all outer edges of the numerical domain.

3.5 Causes of instability in Geowave

For a system to have numerical stability, its energy must not increase from that given at the start of time stepping i.e. it is stable when analytical and numerical values converge. An increase in the energy of the numerical values induces instability. This energy is most often increased through the build up of errors from numerical approximations. These errors then magnify at each time step and can cause the computation process to crash. For further information on numerical stability the reader is referred to Dahlquist et al. (2003).

There are four main factors which should be taken into account with regard to the numerical stability of GW.

1 If energy is not damped sufficiently before reaching the boundaries, numerical blow-up often results therein. A damping layer composed of water nodes can result in too much noise (defined in this study as high frequency, small amplitude variations in the surface elevation or velocity profiles, which result from the higher order terms and derivatives in the extended Boussinesq equations of GW). This noise can lead to the output by GW of unfocused movie images. Water nodes can be replaced with land nodes but this leads to three disadvantages.

- If run up is switched on (which it is not for simulations within this thesis), the grid becomes limited in its resolution.
- The use of land nodes around a geophysical domain, which in reality is surrounded by ocean, is not realistic.

- The code of GW is set up so that no more than three sides of the domain can be land.

2 Additional noise results when the number of nodes in the horizontal directions, becomes to large (or is more than 40 per wavelength Wei et al., 1995). This noise is an accumulation of numerical errors at each node from solving higher order Boussinesq terms. However, 7 nodes per wavelength are needed by GW to resolve run up.

3 A difference between horizontal grid spacing of more than 5% can also result in numerical instability. The code of GW warns when this is the case. The smoother and more uniform a grid is, the better the convergence of numerical solutions. GW uses a fourth order, 5-point Savitsky-Golay filter, to smooth the bathymetric grid. GW version 1.0 provided no option to avoid smoothing. The minor modifications mentioned in section 3.4.1 allow the user to input pre-smoothed grids.

4 For flow that is assumed incompressible, very short time steps are required to completely simulate behaviour between nodes. The introduction to GW of a time step, dependent on the CFL (Courant-Friedrich-Levy) condition (3.26) helps to provide stability by ensuring that the numerical wave speed $dx/\Delta t$ is at least as fast as the physical wave speed, $\sqrt{gH_{\max}}$.

$$dt = 0.3 * \frac{\min(dx, dy)}{\sqrt{gH_{\max}}} \qquad 3.26$$

where dt is the numerical time step, dx and dy are the nodal spacing in the x and y directions, $H_{\max}$ is the maximum depth on the bathymetric grid, g = 9.8 ms^{-2} and 0.3 ensures that, with respect to the physical wave speed, there are at least 3 numerical times steps per grid cell.

If GW fails to converge, a grid file “zdiff.grd” is output. This illustrates the surface elevation for the third iteration of the numerical time step, for which it did not converge. Examination of this file will often illustrate where the instability began.

Chapter 4

Numerical Investigation into Tsunami Scattering from Single Idealised Bathymetric Features

The objective of the research outlined in this chapter is to use numerical methods to compare the differences between contributions from weakly nonlinear and fully nonlinear dispersive Boussinesq terms, to the reflection and transmission of a wave with dispersive properties, which is of normal incidence at four different idealized bathymetric features. These features are: a rectangular ridge (and trench), a Gaussian ridge (and trench), a step escarpment and an error function escarpment.

The chapter is divided into five sections. Section 4.1 provides an introduction and background to the objective of the research. Section 4.2 details numerical methods and setup. Section 4.3 describes the method of collection and presentation of numerical results. Section 4.4 presents and discusses these results. Section 4.5 provides an overall summary of the results.

4.1 Introduction to topic

Two main studies which investigate tsunami behaviour with bathymetric features are those of Koshimura et al. (1999) and Mofjeld et al. (2000). As discussed in Chapter 2, both use an analytical approach to develop theory for the interaction of tsunami waves with single, idealised bathymetric features. These theories have been used to interpret model results from numerical modelling which used bathymetry in the regions of the South-Honshu Ridge (Koshimura et al., 2001) and the North Pacific Ocean (Titov, 1999). The

work in this chapter is motivated by the study presented in Mofjeld et al. (2000). The aforementioned study used linear analytic theory to show the impact that small scale bathymetric features can have on tsunami propagation and emphasized the need for modelling with high spatial resolution and accurate bathymetry.

4.2 Numerical methods and setup

In order to highlight contributions from weakly nonlinear and fully nonlinear extended Boussinesq terms to wave scatter, numerical simulations were conducted using the nonlinear shallow water equations of Geowave (GWS) and the fully nonlinear extended Boussinesq equations of Geowave (GWB) with each of the bathymetries discussed in section 4.2.1. The numerical results for the amplitudes of the reflected and transmitted waves were then compared, where possible, with the linear analytic theory of Mofjeld et al. (2000) (from now on referred to as LAT).

Mofjeld et al. (2000) assume tsunamis to be non dispersive, long gravity waves that satisfy the linearized equations of motion (Equations 4.1 and 4.2)

$$\frac{\partial \underline{Q}}{\partial t} = -gH\nabla\eta \qquad 4.1$$

$$\frac{\partial \eta}{\partial t} = -\nabla.\underline{Q} \qquad 4.2$$

where η is the water surface elevation and, $\underline{Q}$ is the wave transport. Note, $\underline{Q} = H\underline{u}$, where H is the water depth and $\underline{u} = (u_x, u_y)$ is the horizontal water velocity.

Because the linear equations of wave motion solved by Geowave (GWL) are the same as those in Mofjeld et al. (2000) (Equations 4.1 and 4.2), a comparison between GWL and LAT for a discontinuous and a continuous feature (defined in section 4.2.1) was

used to show any discrepancies introduced from the numerical approach. This comparison is discussed in section 4.4.1 and 4.4.2.

Section 4.2 is subdivided into four sub sections. Section 4.2.1 introduces the bathymetric features used in this study and their associated parameters. Section 4.2.2 discusses which of these parameters are suitable for this study. The initial conditions are presented in section 4.2.3.

4.2.1 Introduction of bathymetric features used in this study and their associated parameters

Idealized discontinuous and continuous features are used in this study. The term 'discontinuous', applies to features where changes of height occur in steps. 'Continuous' refers to features where these changes are gradual while the discontinuous features used in this study are a rectangular ridge (and trench) and a step escarpment. The continuous features used in this study are a Gaussian ridge (and trench) and an error function escarpment. To retain consistency in feature profiles between this work and that of Mofjeld et al. (2000), features are described using the relevant equations from Mofjeld et al. (2000). These equations are dependent on the depth parameter (Equation 4.3). This parameter defines the ratio of the depths either side of a feature (see Figure 4.1).

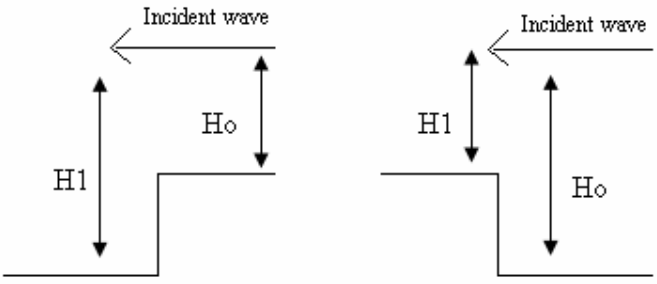

Figure 4.1: This simple bathymetry is used to define the depth parameter (Equation 4.3). H_0 is the depth over which the incident wave propagates and H_1 is the water depth over which the transmitted wave propagates. The left hand side represents $\varepsilon > 1$ and the right hand side represents $\varepsilon < 1$.

$\varepsilon = \sqrt{H_1/H_0}$ where ε=1 represents a flat bottom. 4.3

The four bathymetric features used in this study are presented in the following order: rectangular ridge (and trench), Gaussian ridge (and trench), step escarpment and error function escarpment. In each case the discontinuous feature is presented first. This is because Mofjeld et al. (2000) provide a greater set of results for this bathymetry.

Rectangular ridge and trench

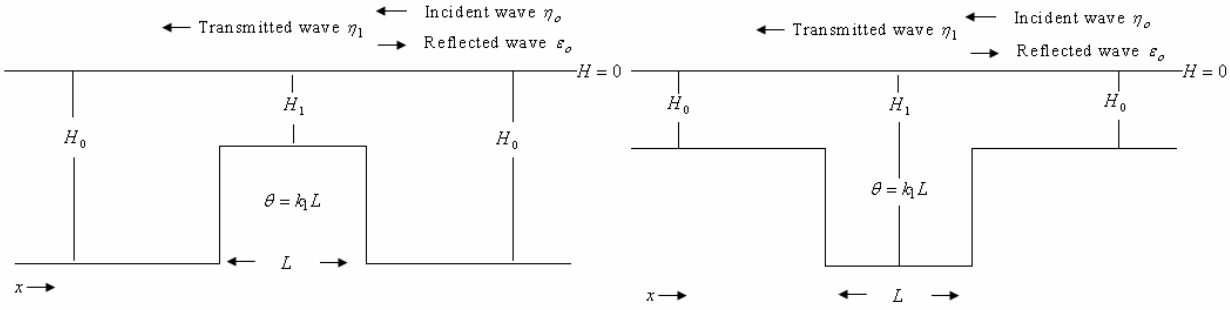

Figure 4.2: (a) rectangular ridge (ε < 1) and (b) rectangular trench (ε > 1).

For a ridge of width L, its inferred cross ridge phase shift is defined by Mofjeld et al. (2000) in as:

$\theta = k_1 L$ where $k_1 = 2\pi / \lambda$ 4.4

Mofjeld et al. (2000) shows the cross ridge phase shift θ for a fixed rectangular ridge width L, to depend inversely on ε through the relationship:

$\theta = \frac{\theta_1}{\varepsilon}$, where $\theta = \theta_1$, when ε=1 4.5

Gaussian Ridge

The continuous Gaussian feature profile used in Mofjeld et al. (2000) is described by Equation 4.6 and shown in Figure 4.3.

$$H(x) = H_0\left[1 + (\varepsilon^2 - 1)e^{-\frac{x^2}{\sigma^2}}\right] \qquad 4.6$$

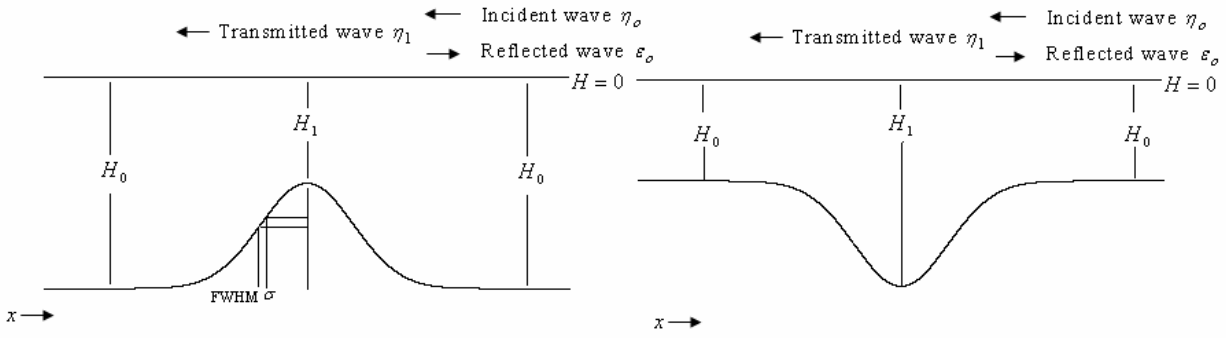

(a) (b)

Figure 4.3: (a) Gaussian ridge profile (ε < 1) and (b) Gaussian trench profile (ε > 1).

The width of a Gaussian feature is described by Mofjeld et al. (2000), using the width parameter $k_0\sigma$, where $k_0 = 2\pi / \lambda$ and, σ is the standard deviation.

Step Escarpment

The profile of the step escarpment is controlled only by the depth parameter.

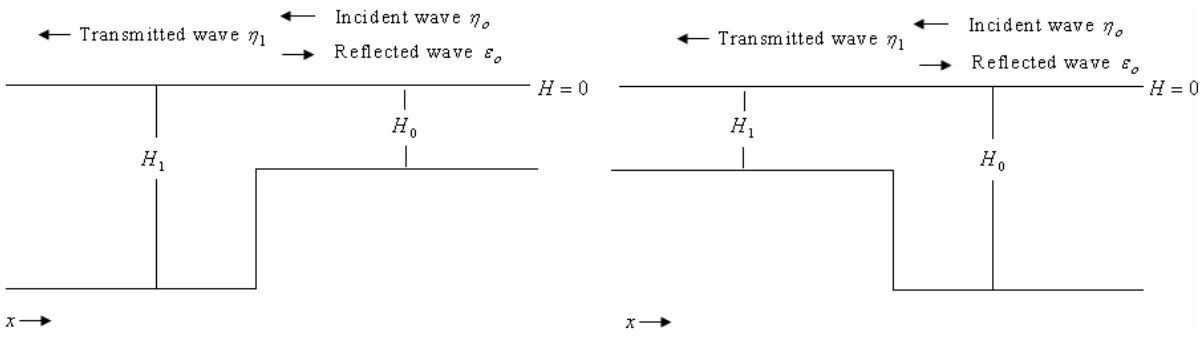

(a) (b)

Figure 4.4: (a) Downward step escarpment (ε < 1) and (b) upward step escarpment (ε > 1).

Error Function Escarpment

The error function escarpment profile of Mofjeld et al. (2000) is described by Equation 4.7 and can be seen in Figure 4.5.

$$H(x) = H_0\left[1 + \frac{\varepsilon^2 - 1}{\sigma\sqrt{\pi}} \int_{-\infty}^{x} e^{\frac{-x^2}{\sigma^2}} dx\right] \qquad 4.7$$

The width of the error function escarpment, as for the Gaussian feature, is defined by the width parameter $k_0\sigma$.

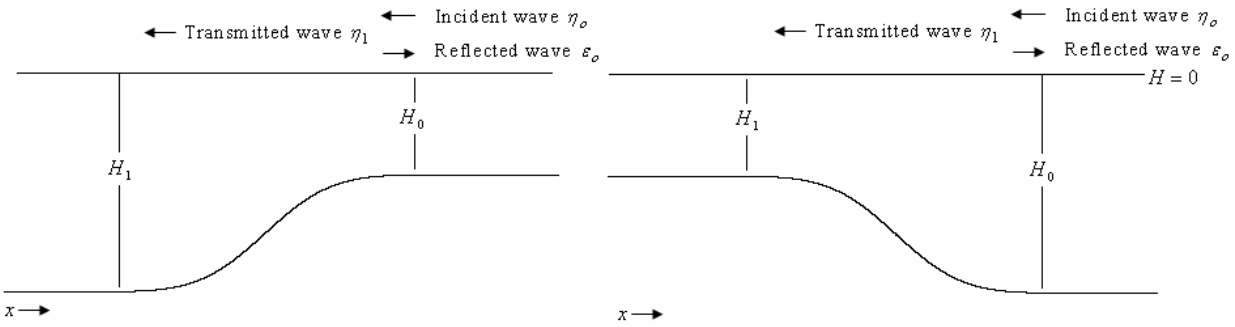

(a) (b)

Figure 4.5: (a) Downward sloping error function escarpment (ε < 1) and (b) upward sloping error function escarpment (ε > 1).

4.2.2 Parameters chosen for the bathymetric features in this study

Once the idealised bathymetric features (section 4.2.1) were selected, the two parameters that control their main dimensions were chosen. These are the depth parameter (for the control of the height) and the feature width:

Depth Parameter

Four values representing large and smaller deviations in depth across a bathymetric feature were chosen.

Large deviations: ε = 0.5 and 2

Smaller deviations: ε = 0.9 and 1.1

The values of H_0, H_1 used to satisfy these values of ε can be seen in the table below.

ε	H_0 (m)	H_1 (m)
0.9	-5	-4.05
0.5	-20	-5
1.1	-5	-6.17
2	-5	-20

Table 4.1: Values of H_0, H_1 used for the four values of ε.

Feature width

In highlighting contributions from the nonlinear and dispersive (Boussinesq) terms, it is preferable to use a width for each feature that will produce a maximum result (i.e maximum transmission or maximum scatter). Because the work of Mofjeld et al. (2000) contains a greater set of results for the reflected wave amplitudes than for the transmitted wave amplitudes, it would therefore be ideal, to use the width for which a maximum reflection was predicted to occur. However, because this optimum scattering width can vary by a factor of ten between features, its use would have meant all features could not be constructed on the same numerical grid size, with the same resolution (see section 4.2.1). Therefore this width was not chosen and instead a standard width was used for each feature. This choice took into account the widths of each feature for which Mofjeld et al. (2000) predicts the strongest reflection to occur, see below:

Rectangular ridge (and trench): The maximum reflection (based on a minimum transmissivity) occurs for a cross ridge phase shift of $\theta = 90°$ given by Equation 4.10.

However, because θ depends inversely on ε (Equation 4.5), and using the chosen values of ε (as above), a maximum reflection will only result when $\theta = \frac{45°}{\varepsilon = 0.5} = 90°$. For this value of $45°$ to satisfy Equation 4.4 (using the fixed wavelength, section 4.2.1) when ε = 1, the ridge width *L* that results, would not be resolved.

Gaussian ridge (and trench): Reflection from this feature is frequency dependent. The strongest reflection occurs from both features for a width parameter of $k_0\sigma$ = 0.707. Solving for σ and using the relationship for a Gaussian $FWHM \approx 2.35\sigma$ (where *FWHM* is the Gaussians full width at half the maximum height), the strongest reflection occurs when $HWHM = 1.32\sigma$. This is equivalent to $\lambda/3.78$ (approximated by Mofjeld et al., 2000 as $\lambda/4$).

Error function escarpment: Reflection from this feature is also frequency dependent. The strongest reflection (from the small changes in depth derived by Mofjeld et al., 2000) occurs for the values of the width parameter $k_0\sigma << 1$. For the standard wavelength of this study, the standard deviation that needed to satisfy this condition, results a distance over which the change in depth occurs, which is too small to be resolved.

Step escarpment: Reflection from this feature depends only on ε. The strongest reflection occurs for values of $\varepsilon >> 1$ (which are not simulated in this study).

The width of a Gaussian ridge (for which a maximum reflection occurs) was chosen as the standard width because firstly, the maximum reflection occurs for values of ε used in this study and secondly, because the width is resolved by the grid resolution (refer to section 4.2.3).

The consistent use of a standard numerical domain size, grid resolution and four select values of ε, means that the standard width chosen does not satisfy the conditions which cause strongest reflections from each of, an error function escarpment, a step escarpment and a rectangular ridge.

4.2.3 Initial conditions

All simulations in this chapter used the same initial conditions. These are as follows. A monochromatic sinusoidal wave of length λ = 5 m was used. This wavelength gives the wave dispersive properties across the initial propagation depths (refer Table 4.1). It also allows for 6 wavelengths of sponge layers to surround each side of the numerical domain without the domain becoming to large. These sponge layers ensured a minimum interference of the propagating wave with the grid boundaries.

An initial wave amplitude a_0 of 0.2 m was used. In order for the wave scatter to be independent from the profile of a forcing velocity, initial velocities were made zero. This resulted in the wave splitting into two components that travelled in opposite directions. According to the standard wave equation, these two components will have the same wavelength and an amplitude that is half a_0. However, because the initial sinusoidal wave form is discretized by the numerical method, the amplitude after the initial wave split is not exactly $a_0/2$. This is not of concern in this study.

To avoid discrepancies in the numerical studies between the features investigated, each simulation used a numerical domain that was consistent firstly, in its dimensions (600 m in the *x*-direction and 80 m in the y-direction) and secondly, in the resolution of the finite difference grid. On consideration of a domain which included 6 wavelengths of sponge layers on all four sides the finite difference grid was gridded using the nearest neighbour method and has a horizontal grid resolution of 0.41 m. This resolution was the

finest that could be achieved for the discontinuous ridge without modelling resulting in numerical failure, whilst at the same time resolving the distance over which the height of a feature changes by a minimum of three nodes.

Simulations involving all four bathymetries were conducted for waves of normal incidence only. Oblique incidence was not examined in this study. This was because the reflection from continuous features depends on wave frequency (Mofjeld et al., 2000) which would introduce waves of different frequencies to those of normal incidence, and results would be no longer comparable.

4.3 Collection and verification of numerical results

Information on the collection and verification of numerical results is provided in two sections. Section 4.3.1 presents details for comparing the numerical reflected and transmitted wave amplitudes with the theory of Mofjeld et al. (2000). Section 4.3.2 presents an investigation into the wave evolution predicted by GWB, GWS and GWL across a constant depth. This highlights any damping or dispersion that has occurred independent of a bathymetric feature.

4.3.1 Comparison of numerical values with linear analytic theory

The reflected and transmitted wave amplitudes predicted by GWB, GWS and GWL from and across a bathymetric feature are presented as ratios of the incident wave amplitude. The reflected wave amplitude ratio (R_r) is defined by Equation 4.8 and the transmitted wave amplitude ratio (R_t) by Equation 4.9.

$$R_r = \frac{B_0}{A_0} \qquad 4.8$$

$$R_t = \frac{A_t}{A_0} \qquad 4.9$$

B_0 is the maximum reflected wave amplitude from the feature of interest, A_0 is the maximum incident wave amplitude at the feature of interest and A_t is the maximum wave amplitude transmitted across the feature.

R_r and R_t were obtained from measurements made at numerical gages of fixed locations: B_0 - 5 m before the feature; A_0 - at the beginning of the feature; A_t - 1 m after the feature ends.

4.3.2 Wave evolution predicted by GWB, GWS and GWL across a flat bottom bathymetry

To highlight possible wave decay and other behaviours that have occurred in the simulations, independent of a single bathymetric feature, simulations using GWB, GWS and GWL were conducted over an idealized flat bottom bathymetry. The decay of the amplitude of a wave as it propagates over two different initial depths (5 m and 20 m) was considered. Wave amplitudes were taken at thirteen numerical wave gages placed every 15 m (increasing in the negative *x* direction) from the initial propagation location referenced as 330 m. Results are plotted in Figure 4.6. Note that for this study, the main wave component of interest is that which propagates in the negative x direction.

From Figure 4.6 (below) three prominent behavioural characteristics can be seen.

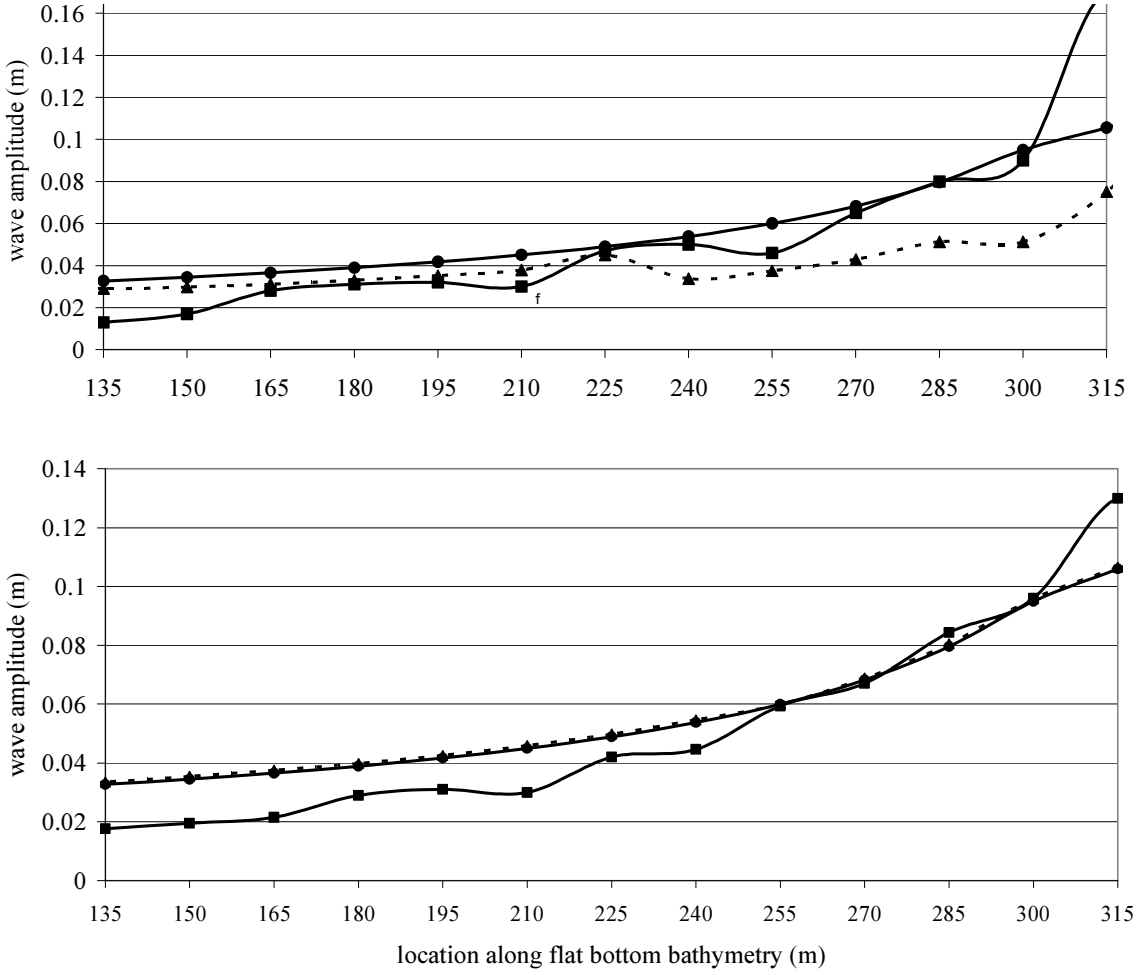

Figure 4.6: Wave amplitude as a function of the wave's position along the flat bottom basin, for GWB (squares), GWS (triangles) and GWL (circles) over depths of 5 m (top) and 20 m (bottom). (NB: propagation begins at 330 m and is in the negative x-direction).

The first of these is the obvious decay in wave amplitude across both depths. The decay in Figure 4.6 was calculated by fitting a trend line (not shown) to the GWL amplitudes in Figure 4.6. This trend line approximated a decay of 0.25 of a percent of the initial amplitude per meter.

To eliminate the application frequency of the high energy filter (defined in GW as 'itfr') as a contributor to this decay, the above experiment was repeated for '*itftr'* every 1, 5, and 200 time steps, in addition to the chosen default frequency of every 20, for a wave propagated using GWB, GWS and GWL over a depth of 5 m. This depth was chosen as it

provides a greater likelihood of non linearity's developing. A comparison between GWB, GWS and GWL simulations, for each of the four filter frequencies (1, 5, 20 and 200) showed differences in amplitude in the third decimal place. This difference was considered to be insignificant and was eliminated as a contributing factor to the observed decay in GWB, GWS and GWL wave amplitudes.

Results from trial simulations conducted using the same method as above but with the use of an initial horizontal velocity, still exhibited a decay in wave amplitude, only to a lesser extent. On closer examination of the Geowave source code it is evident that the propagation friction coefficient incorporated into the code which scales with a parameter proportional to the inverse depth. It follows that the above decay (refer to Figure 4.6) is primarily attributed to friction.

The second observation in Figure 4.6 is the inconsistent behaviour of GWB and GWS wave amplitudes between depths. An example of this is the decrease in amplitude which occurred in GWS across the 5 m depth, compared to that which occurred across the 20 m depth. The cause of this decrease can only be attributed to the shallower depth, which by comparison to the 20 m depth, causes a slightly steeper wave front which results in stronger nonlinear contributions from GWS.

The third observation in Figure 4.6 is that at the location of 315 m, GWB predicts a considerably larger wave amplitude than that of GWS and GWL.

To better understand the behaviour of the wave form as it evolves as predicted by GWB over the flat bottom bathymetry, the propagation of the wave was analysed in more detail. This involved the verification of two aspects. The first was whether the GWB waveform has split into two separate and opposite travelling components. Surface elevation after the wave has propagated 15 m in the negative x direction (refer Figure 4.7) illustrates that this process has occurred.

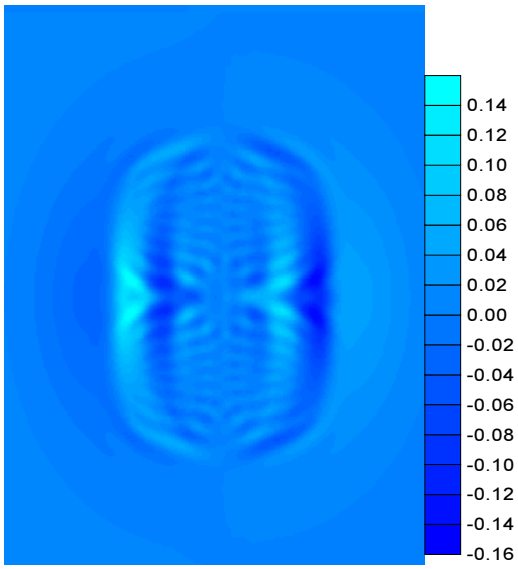

Figure 4.7: Surface elevation (in metres) of the GWB predicted wave form after a propagation distance of 15 m. Two waves travelling in opposite directions are observed.

The second aspect to verify was the occurrence of the process of dispersion. A comparison between the Fourier decompositions of the GWB predicted time series, recorded at the reference locations of 300 m and 270 m, and the equivalent decomposition of the GWL predicted time series illustrates that the process of dispersion is occurring. This comparison can be seen in Figure 4.8.

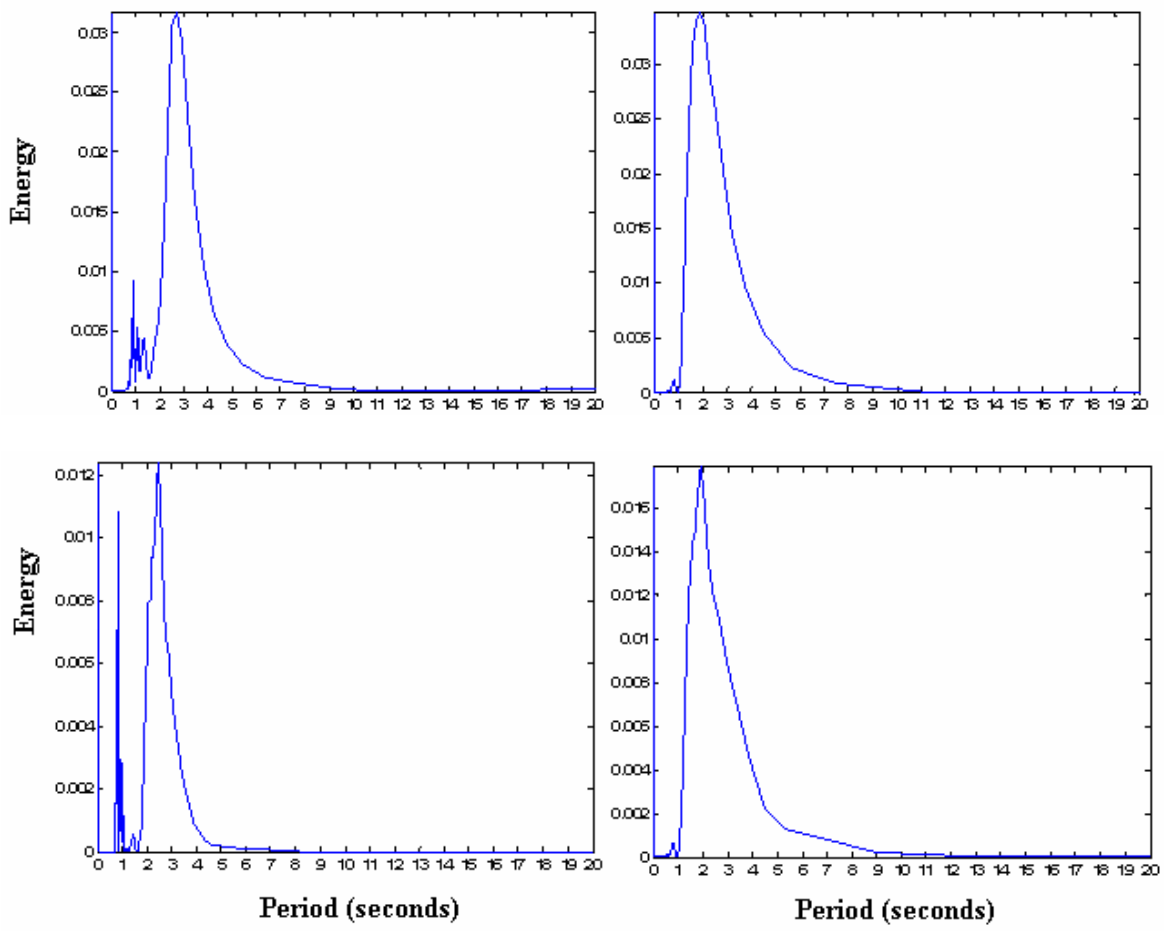

Figure 4.8: Fourier decompositions of the wave form predicted by GWB (left) and GWL (right) from the time series recorded at the reference locations of 300 m (top) and 270 m (bottom). These locations correspond to a wave propagation distance of 30 m and 60 m respectively

Figure 4.9 (below) presents the maximum heights from the Fourier transforms conducted on the time series recorded by nine of the thirteen gages mentioned in the first paragraph of section 4.3.2, and from an additional gage located at a distance 5 m in the direction of wave propagation. These results show a general decrease in the energy of the main component, as is suggested by Figure 4.6. They also illustrate that the process by which the wave is split into two components is predicted by GWB to occur over a larger spatial extent. This explains the third behaviour, as mentioned above, that is observed in Figure 4.6.

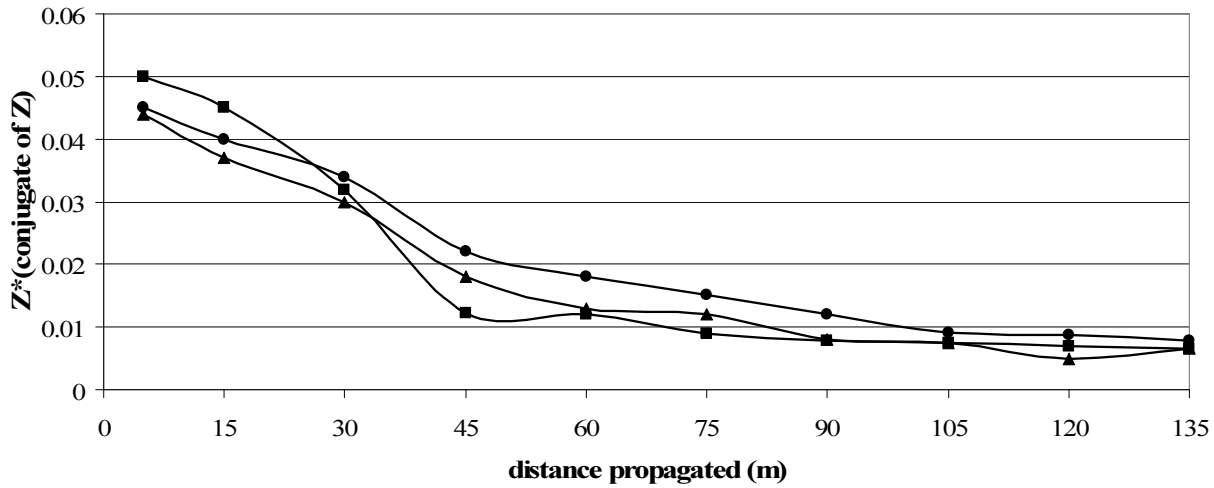

Figure 4.9: Maximum values of the Fourier transforms conducted on the time series recorded at the wave gages with positions indicated by the solid symbols. Key: GWB - square; GWS - triangle; GWL - diamond. N.B. all single bathymetric features are situated between 30 m and 40 m.

The incorporation of GWB, GWS and GWL predicted wave behaviours, for the flat bottom bathymetry

The first and second behaviours observed in Figure 4.6 (refer section 4.3.2, paragraph 3), were incorporated into the numerical results of R_r and R_t (defined in section 4.3.1) for each of the four bathymetric features. Incorporation of the first behaviour accounts for the decay that occurred between the gage where A_0 was measured and the gage where A_t was measured.

Inclusion of the second behaviour (refer section 4.3.2, paragraph 4), was necessary in order for GWB, GWS and GWL results to be representative of the wave interaction with the feature and not the dependence on the propagation distance or the water depth. This behaviour was included by dividing GWB, GWS, and GWL values of R_r and R_t for each bathymetric feature, by R_r and R_t for a constant depth. Note; these latter two values were obtained from data recorded by gages situated at the same distances as those in the numerical set up which includes a bathymetric feature.

The effects of the third point observed in Figure 4.6 (refer section 4.3.2, paragraph 5), are assumed to be eliminated to an extent best achievable for the purpose of this work by two procedures (that are both already implicated). These are that the bathymetric features are always placed at a constant distance from the initial wave, and that all results are normalised with respect to wave behaviour across a flat bottom.

4.4 Numerical results and discussion

This section is a comparison of the numerical results, with those of Mofjeld et al. (2000) for the four bathymetric features in the order: a rectangular ridge (and trench), a Gaussian Ridge (and trench), a step escarpment and an error function escarpment.

4.4.1 Rectangular Ridge and Trench

LAT values of R_t across a ridge are given in Equation 4.10. Mofjeld et al. (2000) refers to this as the transmissivity of a wave across a ridge. Equation 4.10 gives a minimum value when θ is an odd multiple of $90°$.

$$R_t = \frac{A_t}{A_0} = T_{\min}\left[T^2{}_{\min}\cos^2\theta + \sin^2\theta\right]^{-1/2} \qquad 4.10$$

where $T_{\min} = \dfrac{2\varepsilon}{1+\varepsilon^2}$

LAT values of R_r (Equation 4.11) are obtained from the reciprocal relationship $T^2 + R^2 = 1$. For verification of this relationship refer to Mofjeld et al. (2000).

$$R_r = \frac{B_0}{A_0} = \sqrt{1-T} \qquad 4.11$$

It was hypothesized that the largest difference between R_r (GWB) and R_r (GWS) would be seen for the rectangular ridge because of its discontinuity, even though the standard width does not result in the strongest reflections from this feature. However, application of GWB to the rectangular ridge (for all values of ε) resulted in numerical overflow and prevented evaluation of this hypothesis.

R_r and R_t values of GWS and GWL are compared with those of LAT (Equations 4.10 and 4.11). Results are presented in Figure 4.10.

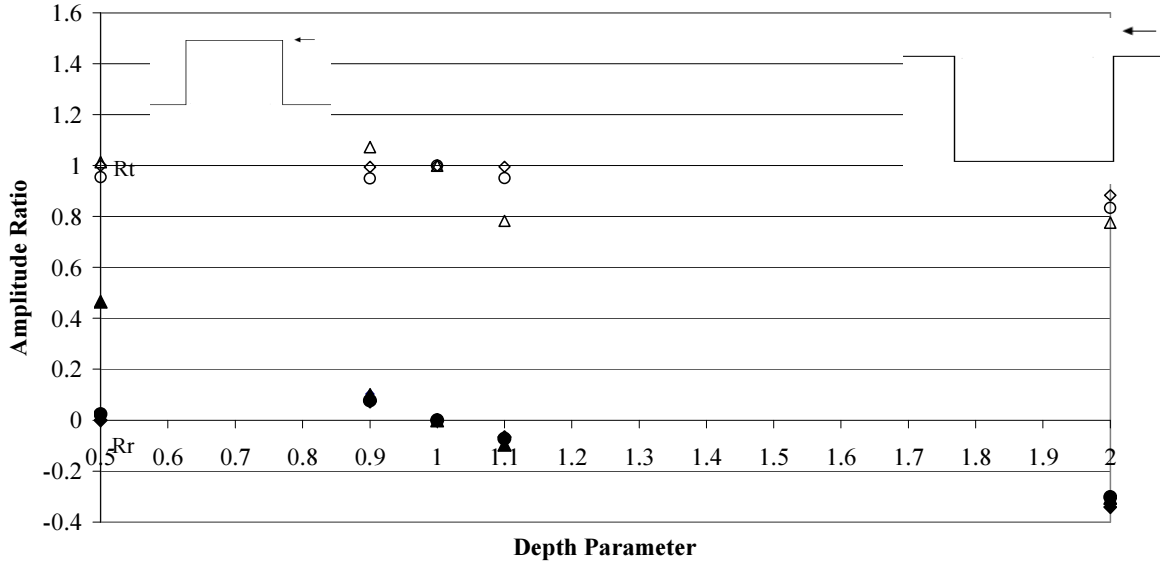

Figure 4.10: R_t (open symbols) and R_r (solid symbols), for a wave incident on a rectangular ridge and trench, of fixed frequency ω and width L for θ_1=90°. Key: GWB-square; GWS-triangle; LAT- diamond. Amplitude ratios less than zero indicate that the wave was inverted upon reflection.

Figure 4.10 illustrates a good agreement between R_r (GWL) and R_r (LAT) values from the discontinuous feature. Closer observation of these values in Table 4.2 shows a quantitative agreement of over 88%.

ε	R_r (((GWL)-(LAT))/LAT)%
2	-6
1.1	-4.5
1	0
0.9	-9
0.5	-12

Table 4.2: Percent difference between R_r(GWL) and R_r(LAT) for a rectangular feature that is discontinuous and has a smaller variation in depth. A negative value means R_r(LAT) > R_r(GWL).

However, Figure 4.10 illustrates a larger difference (45%) between R_r(GWS) and R_r(LAT) for ε = 0.5. This would suggest that the development of nonlinearities on the shallower ridge.

The two ridge values ε = 0.5 and ε = 0.9 appear to have had only a minor affect on the transmitted wave amplitude of GWS which agree to within 5%. LAT predicts a similar trend and its R_t values agree to within 0.2%.

The inverse dependence of θ on ε, through the relationship in Equation 4.5, implies that as ε increases to values greater than 1, θ becomes smaller and the effect of the trench width on scattering is decreased (Mofjeld et al., 2000). R_t(GWS) values for ε = 1.1 and ε = 2 support this trend and are within 0.8% of each other. However, both values are smaller than those of R_t(LAT) by 21% for ε = 1.1 and 16% for ε = 2. Observation of the time series from wave gages (on, before and after the feature), as well as surface elevation images, shows that these smaller R_t(GWS) values are the result of nonlinear interactions. These interactions occurred between wave components that had passed onto the trench and components reflected back from the shallower region as the main wave continued to propagate from right to left.

4.4.2 Gaussian Ridge and Trench

Results of GWB, GWS and GWL for R_r and R_t, from the interaction of a wave with the Gaussian feature (Equation 4.4) are presented in Figure 4.11. R_r values of LAT (Equation 4.12) are also presented for the smaller values of ε.

$$\frac{B_0}{iA_0} = -(\partial\varepsilon)\sqrt{\pi}k_0\sigma e^{-k_0{}^2\sigma^2}, \text{ where } \partial\varepsilon = \varepsilon - 1 \qquad 4.12$$

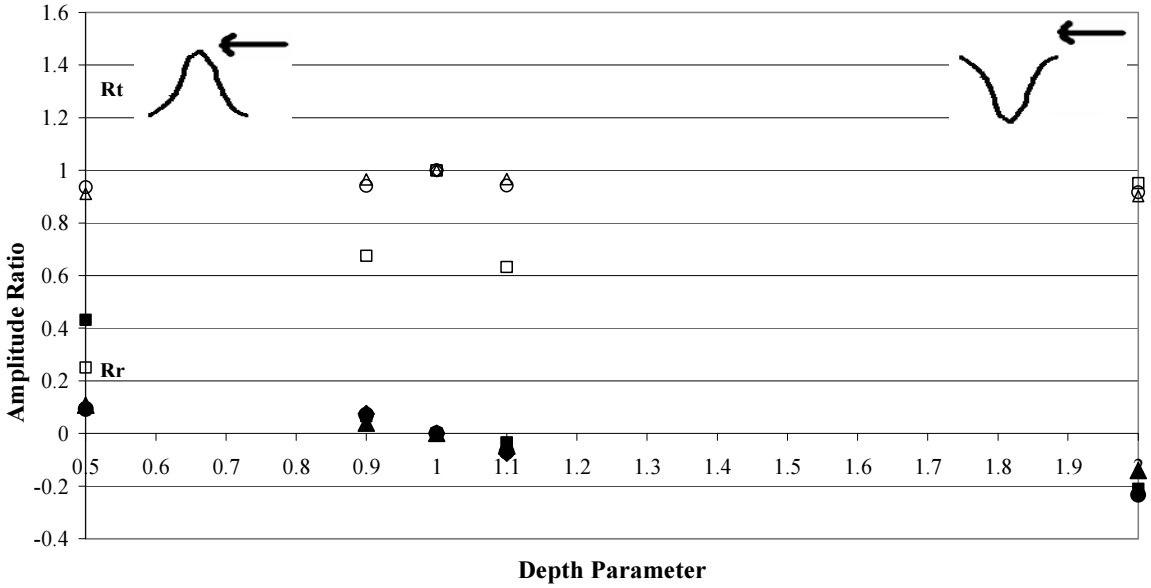

Figure 4.11: R_t (open symbols) and R_r (solid symbols), for a wave incident on a Gaussian feature, as a function of ε. Key: GWB-square; GWS-triangle; GWL - circle; LAT- diamond. Amplitude ratios less than zero indicate that the wave was inverted upon reflection.

Figure 4.11 illustrates a good agreement between R_r (GWL) and R_r (LAT) values for small changes in depth across a continuous feature. Closer observation of these values in Table 4.3 shows a quantitative agreement of over 93%.

ε	R_r (((GWL)-(LAT))/LAT)%
1.1	-7
1	0
0.9	-5

Table 4.3: Percent difference between R_r (GWL) and R_r (LAT) for a Gaussian feature that is continuous and has a small variation in depth. A negative value means R_r (LAT) > R_r (GWL).

The observed discrepancies in Table 4.3 for a continuous feature, are within 4% of those observed between GWL and LAT for a discontinuous feature (refer to Table 4.2). Hence, discrepancies between GWL and LAT are attributed to two main factors. These are firstly, the numerical discretisation of the single sinusoidal waveform which results in more than a single wave number (a Fourier decomposition of the initial conditions will show this) and secondly, possible changes to the reflected numerical wave amplitude during its propagation to where it was measured. Given that these two factors also exist for GWB and GWS simulations, differences between GWB and GWL and, GWS and GWL, are assumed to be contributions from higher order terms which occurred during the process of dispersion or nonlinear interaction. It is possible that part of this difference is attributable to the resolution and time step. Given the combination of computational limitations and resolution criteria (discussed in section 4.2.2) this possibility was not explored in great detail.

Figure 4.11 shows similar values of R_t (GWL) and R_t (GWS) for all four values of ε (refer to Table 4.4). This suggests that due to the gentle slope over which the depth change evolves for a Gaussian ridge or trench, contributions from weakly nonlinear terms are minor.

ε	R_t ((GWL-GWS)/GWS)%
2	1.60
1.1	2.86
1	0
0.9	2.87
0.5	8.42

Table 4.4: Percent difference between R_t (GWL) and R_t (GWS) for values of the depth parameter ε used in this study.

Reference to Figure 4.11 shows R_t (GWB) values are significantly smaller than R_t (GWS) for ε = 0.5, 0.9, 1.1. These differences are shown in Table 4.5.

ε	R_t ((GWS-GWB)/GWB)%
0.5	73
0.9	30
1.1	33

Table 4.5: Percent difference between R_t (GWS) and R_t (GWB).

For ε = 0.5, R_t (GWB) is 73% smaller than R_t (GWS) (refer to Table 4.5). This results from the more uniform spread of the energy between the GWB wave components, which was caused by dispersion as the wave approached the ridge top.

Comparison between R_t (GWB) values, for small changes in depth (ε = 0.9 and 1.1), shows only a 5% difference. Nonetheless, R_t (GWB) is smaller than R_t (GWS) for both these small changes in depth (refer Table 4.5).

4.4.3 Step Escarpment

LAT values of R_r and R_t, for a wave of normal incidence on a step escarpment are frequency independent and can be calculated from Equations 4.13 and 4.14 respectively.

$$R_r = \frac{1-\varepsilon}{1+\varepsilon} \qquad 4.13$$

$$R_t = \frac{2}{1+\varepsilon} \qquad 4.14$$

Results from Equations 4.13 and 4.14 are compared against those of GWB and GWS for this bathymetry. They are presented in Figure 4.12.

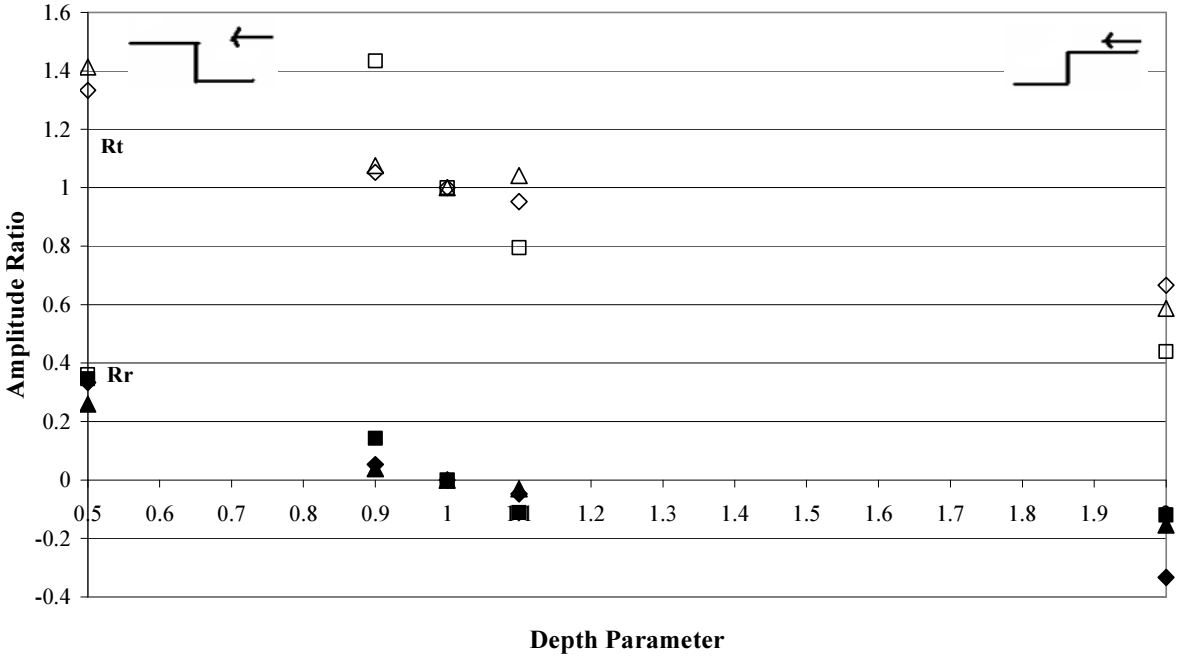

Figure 4.12: R_t (open symbols) and R_r (solid symbols), for a wave incident on a step escarpment as a function of ε. Key: GWB-square; GWS-triangle; LAT- diamond. Amplitude ratios less than zero indicate that the wave was inverted upon reflection.

The most prominent behaviour observed in Figure 4.12 is that of R_t (GWB) values. For ε = 0.5, R_t (GWB) is 3.6 times smaller than R_t (GWS). Analysis of times series and surface elevation files shows the development of an instability in the deeper water adjacent to the upward step. This resembles that of the Benjamin-Feir instability (Benjamin and Feir, 1967) in which energy is transferred from a main carrier wave to the two side band frequencies when $\Delta k/(k_0 e) < 2\sqrt{2}$, where k is the wave number and e is the steepness factor (wave number multiplied by wave amplitude) (Onorato et al., 2006). As a result of this instability, some of the energy from the main wave front was transferred into the dispersed GWB wave train. This resulted in a transmitted wave amplitude which is smaller than that predicted by GWS.

For ε = 0.9, R_t (GWB) > R_t (GWS) by 33%. This was caused by the smaller change in depth which allowed a greater proportion of the GWB components of the waveform to be passed onto the upward step and undergo nonlinear interactions. This resulted in R_t (GWB) for ε = 0.9 being approximately four times greater than R_t (GWB) for ε = 0.5.

For ε = 1.1 and ε = 2, R_t (GWB) is smaller than both R_t (GWS) and R_t (LAT) (see Figure 4.12). For these two values of ε, R_t (GWB) < R_t (GWS) by 25%. For ε = 1.1, this difference is because the previously dispersed GWB wave form underwent minimal change upon passing the step down, hence R_t (GWB) = 0.8. However, for ε = 2, this difference was due to the development of a numerical instability in GWB excited by the discontinuity in the depth.

Observation of Figure 4.12 shows very different behaviours between R_t (GWB) for ε = 0.9 and R_t (GWB) for ε = 1.1. This difference is contrary to that of R_t (GWS) for these values of ε, which are within 4% difference of LAT.

4.4.4 Error Function Escarpment

For small changes in depth across an error function escarpment R_r (LAT) can be calculated from Equation 4.15.

$$R_r = \frac{B_0}{A_0} \cong \left(\frac{-\partial \varepsilon}{2} \right) e^{-k_0^2 \sigma^2} \qquad 4.15$$

The behaviour of a wave incident on an error function escarpment is examined for the four values of ε using GWB and GWS. For all four, GWB and GWS values of R_r and R_t are presented in Figure 4.13 along with LAT values of R_r for ε = 0.9 and 1.1.

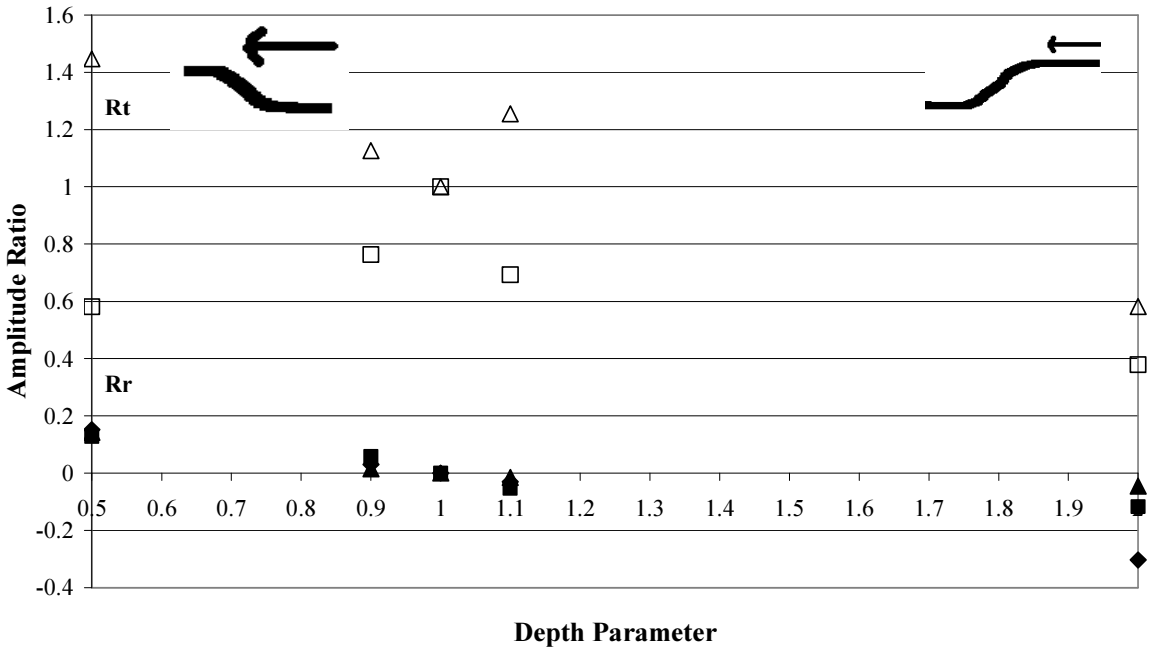

Figure 4.13: R_t (open symbols) and R_r (solid symbols), for a wave incident on an error function escarpment as a function of ε. Key: GWB-square; GWS-triangle; LAT- diamond. Amplitude ratios less than zero indicate that the wave was inverted upon reflection.

Figure 4.13 shows that R_r (GWB) and R_r (GWS) values are quantitatively much closer in magnitude than those of R_t (GWB) and R_t (GWS). (The same trend can be seen for the step escarpment, section 4.3.3). The largest difference between R_t (GWB) and

R_t(GWS) is for transmission across the upward escarpment of ε = 0.5. In this case R_t(GWS) is 156% greater than R_t(GWB). Examination of GWB time series and surface elevation images showed the decrease in the transmitted wave amplitude to have occurred as a result of both the transferral of energy via nonlinear processes and dispersion that occurred as the approached the shallower level of the escarpment. (Note, because the wave underwent dispersion and nonlinear interactions 'approaching' and 'on' this continuous error function escarpment, as opposed to only on 'approaching' the continuous Gaussian ridge, R_t(GWB), for ε = 0.5 in the above figure, is greater than R_t(GWB) for the Gaussian ridge. For further detail, refer to section 4.4.2). Conversely, GWS waveform did not disperse but underwent shoaling and so the transmitted amplitude was increased.

The second biggest difference is for ε = 1.1, where R_t(GWB) is 45% smaller than R_t(GWS). Observation of the time series from wave gages showed this to be attributable to dispersion in GWB over the increasing water depth. The larger R_t(GWS) value resulted from a combination of no dispersion and weakly nonlinear interactions. For ε = 0.9, R_t(GWB) is 35% smaller than R_t(GWS). This is due to the gradual change in depth that aggravates an increase in dispersion, meaning there is less energy located in the main transmitted wave front. This trend in which R_t(GWB) values for ε = 0.9 and ε = 1.1 are significantly less than those of R_t(GWS) is also apparent for the continuous Gaussian feature (section 4.4.2).

4.5 Summary

Comparisons of the linear shallow water equations (GWL), the weakly nonlinear shallow water equations (GWS) and the fully nonlinear extended Boussinesq equations (GWB) of GW with the linear analytic results of Mofjeld et al. (2000) (LAT), were made for wave

reflection and transmission at four bathymetries: a rectangular ridge (and trench), a Gaussian ridge (and trench), a step escarpment and an error function escarpment.

Differences between GWL and LAT reflected wave amplitudes were assumed to be primarily from to the numerical discretisation of the sinusoidal wave and therefore the differences between GWB and GWL, GWB and GWS, and GWS and GWL, were assumed to be contributions of higher order nonlinear or dispersive terms.

In addition to large changes in depth for continuous features, it has been shown that smaller changes in depth, ε = 0.9 and ε = 1.1, can cause transmitted wave amplitudes predicted by the more computationally demanding GWB to be significantly smaller than those of GWS. These differences are primarily ascribed to dispersion.

Considerable differences between R_t(GWB) and R_t(GWS) are observed for the continuous Gaussian and error function escarpment features with smaller values; of ε = 0.9 and ε = 1.1. For the error function escarpment these differences are, ε = 0.9; R_t(GWB) is 55% less than R_t(GWS) and ε=1.1; R_t(GWB) is 45% less than R_t(GWS). For the Gaussian, ε = 0.9; R_t(GWB) is 30% less than R_t(GWS) and ε = 1.1; R_t(GWB) is 33% less than R_t(GWS). For ε = 0.9, the differences observed for each feature are believed to result from decreased transmission of the dispersed GWB wave and an increase in the amplitude of GWS from shoaling. For ε = 1.1, they are believed to result from the occurrence of dispersion in GWB.

Chapter 5

Numerical Investigation into Tsunami Scattering from a Combination of Two Idealised Bathymetric Features

This chapter expands on Chapter 4. It presents reflection and transmission results for a wave with dispersive properties incident at a combination of two idealized bathymetric features. The objective of this study is to highlight, for the particular wave frequency used in the previous chapter, the dependence of dispersive and nonlinear contributions to wave scatter, both on the feature order and on the distance that separates them. As in Chapter 4, the ratio of the water depth to wavelength is representative of that which is possible for a tsunami produced from a mechanism such as a sub-marine landslide, slump or volcanic eruption.

The chapter is divided into three parts. Section 5.1 contains the numerical methods and set-up. In section 5.2 numerical results are presented. Section 5.3 contains the conclusions of this chapter's findings.

5.1 Numerical methods and set-up

Numerical simulations using the same initial conditions as in section 4.2.3 and a two feature bathymetric profile (Figure 5.1) were carried out for GWB, GWS and GWL.

To understand how contributions from nonlinear and dispersive terms vary as a function of the separation distance (SD) between the two features, simulations were conducted for the following values $0\,\lambda$, $0.25\,\lambda$, $0.5\,\lambda$, $0.75\,\lambda$, $1\,\lambda$, $1.5\,\lambda$ and $3\,\lambda$, where λ

is the wavelength of the initial wave used in this study. For a SD of 0 λ the trailing edge of the first feature links to the leading edge of the second feature. To understand if and how the order of the features affects these contributions, wave propagation from either side of the combined feature profile was simulated (Figure 5.1). The incident wave propagates the same distance as used in Chapter 4 before it reaches the combined feature.

Numerical values of the reflected wave amplitude ratio (R_r) and the transmitted wave amplitude ratio (R_t) are measured at wave gages using the same procedure outlined in section 4.3.1. These ratios are given by Equations 4.8 and 4.9 in Chapter 4. R_r is calculated for the wave amplitude reflected from either side of the combined feature profile. R_t is calculated for the wave amplitude transmitted across either combination of the two features (refer to Figure 5.1). R_t values were corrected, as outlined in section 4.3.2, for any decay that may have occurred independent of the wave-feature interaction.

5.1.1 Combinations of bathymetric features

A Gaussian ridge and a Gaussian trench with respective ε values of 0.9 and 1.1 are the two features used in the combination (Figure 5.1). Their individual profile remains identical to that in Chapter 4.

The Gaussian bathymetry was chosen to represent real bathymetric forms. As depth variations of ε = 0.9 and ε = 1.1 are more prevalent in ocean floor bathymetry these values were chosen over the more theoretical values of ε = 0.5 and ε = 2 (used in Chapter 4).

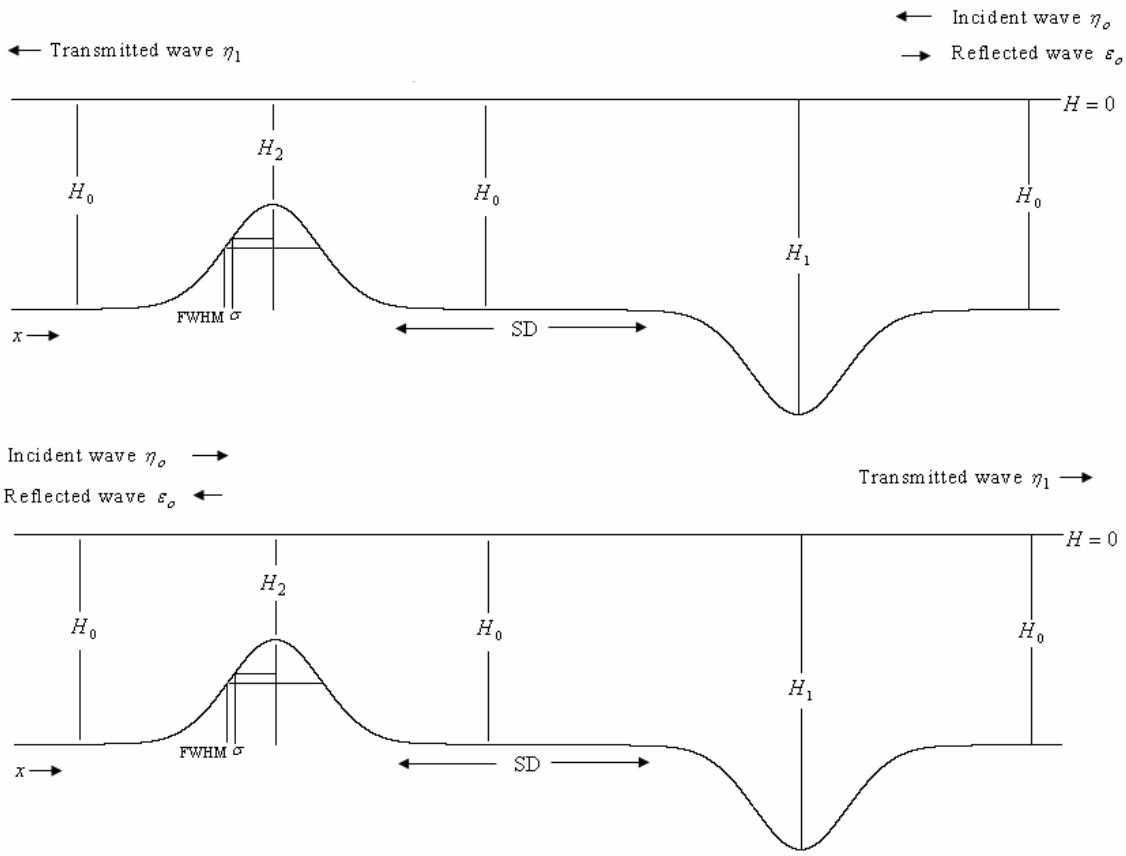

Figure 5.1: The top and bottom profiles represent the two possible combinations for which a wave will interact. The ratio of the depth either side of the trench is given by $\varepsilon = \sqrt{H_1/H_0}$ =1.1 and, of the ridge by $\varepsilon = \sqrt{H_2/H_0}$ =0.9. The separation distance (SD) is defined as the distance between the point on the left hand side feature before it ascends above H_0, and the point on the right hand side feature before it descends below H_0.

5.2 Numerical results

The numerical results of wave reflection and wave transmission are presented in sections 5.2.1 and 5.2.2 respectively. There are no analytic solutions (LAT) available for comparison.

5.2.1 Reflection

R_r values for the combinations RT (refer bottom section, Figure 5.1) and TR (refer top section, Figure 5.1) are plotted as a function of the separation distance in Figures 5.2 and 5.3 respectively.

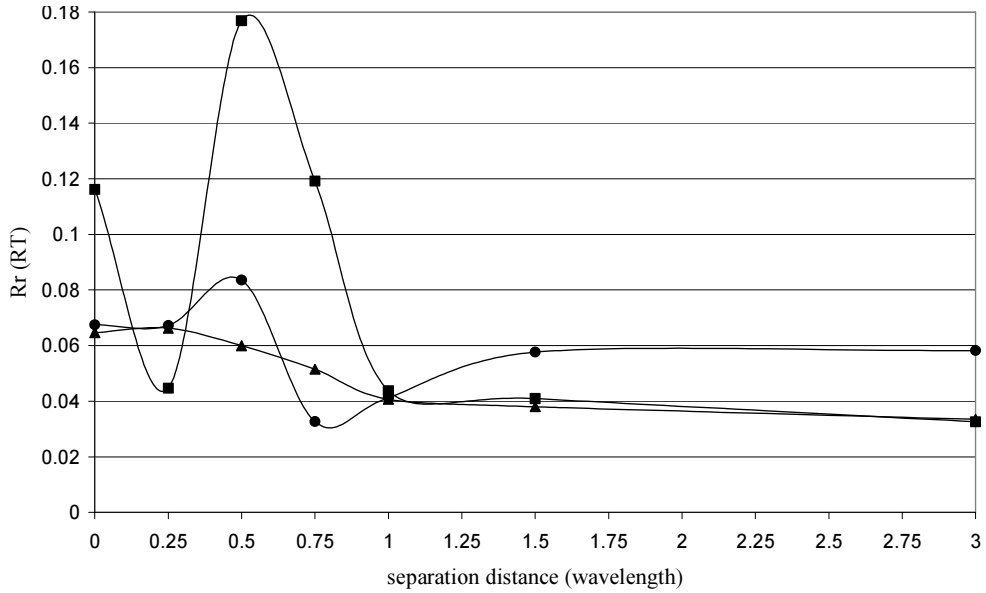

Figure 5.2: R_r values as a function of the separation distance, for a wave incident on a Gaussian ridge-trench combination, for GWB (square), GWS (triangle) and GWL (circle).

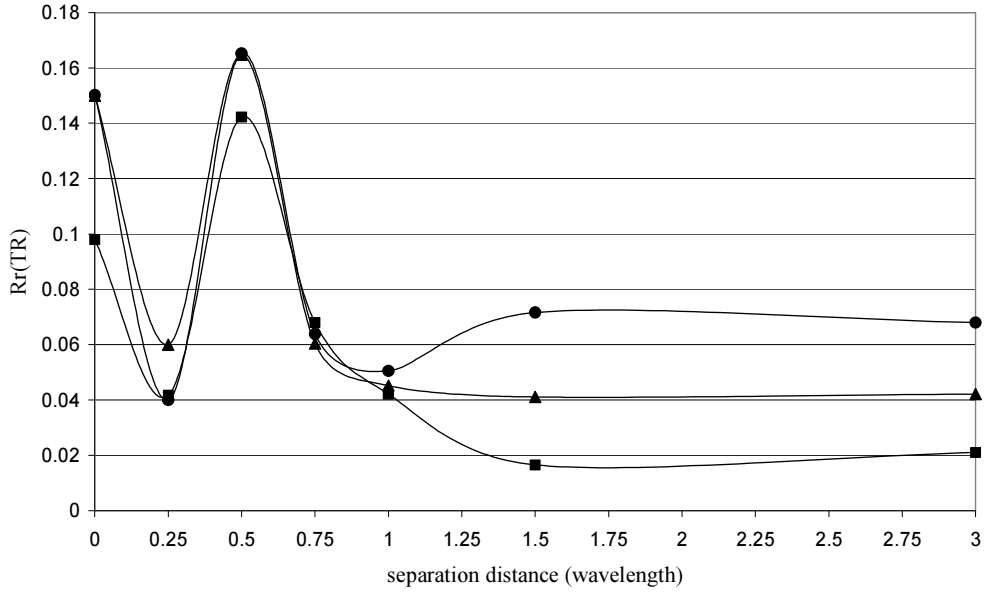

Figure 5.3: R_r values as a function of the separation distance, for a wave incident on a Gaussian trench-ridge combination, for GWB (square), GWS (triangle) and GWL (circle).

In order to highlight any possible differences between R_r for a single feature R_r(single) and R_r for the combined feature R_r(combined), ratios of R_r(combined) to R_r(single) are plotted as a function of the separation distance for the RT and TR combinations. Results can be seen in Figures 5.4 and 5.5 respectively.

Although on first glance Figures 5.4 and 5.5 appear different, closer observation reveals two significant behaviours prevalent for both. The first is that the ratio of R_r(combined) to R_r(single) is close to one for SD of 1.5 λ and 3 λ. This suggests that the reflected wave amplitude of GWB, GWS and GWL is dependent on the presence of a second feature situated within a distance of 1.5 λ.

For both combinations this dependence of reflection is strongest for GWB, and in particular for SD = 0.5 λ. For this SD in the RT combination, R_r(GWB) is 4.23 and for the TR combination R_r (GWB) is 6.56. (For the values at 1.5 λ the reader is referred to Table 5.1). This SD is most likely associated with the fundamental frequency that occurs for the value of λ/2.

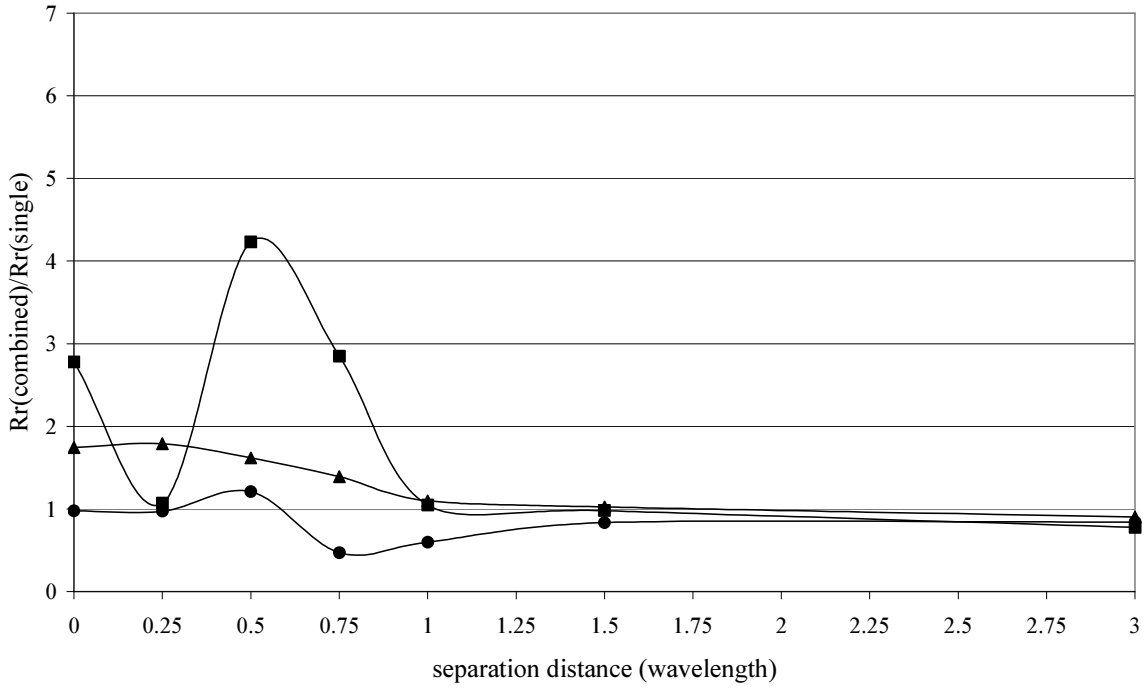

Figure 5.4: Ratio of R_r for a ridge-trench combination to R_r for a single Gaussian ridge, as a function of the separation distance, for GWB (square), GWS (triangle) and GWL (circle).

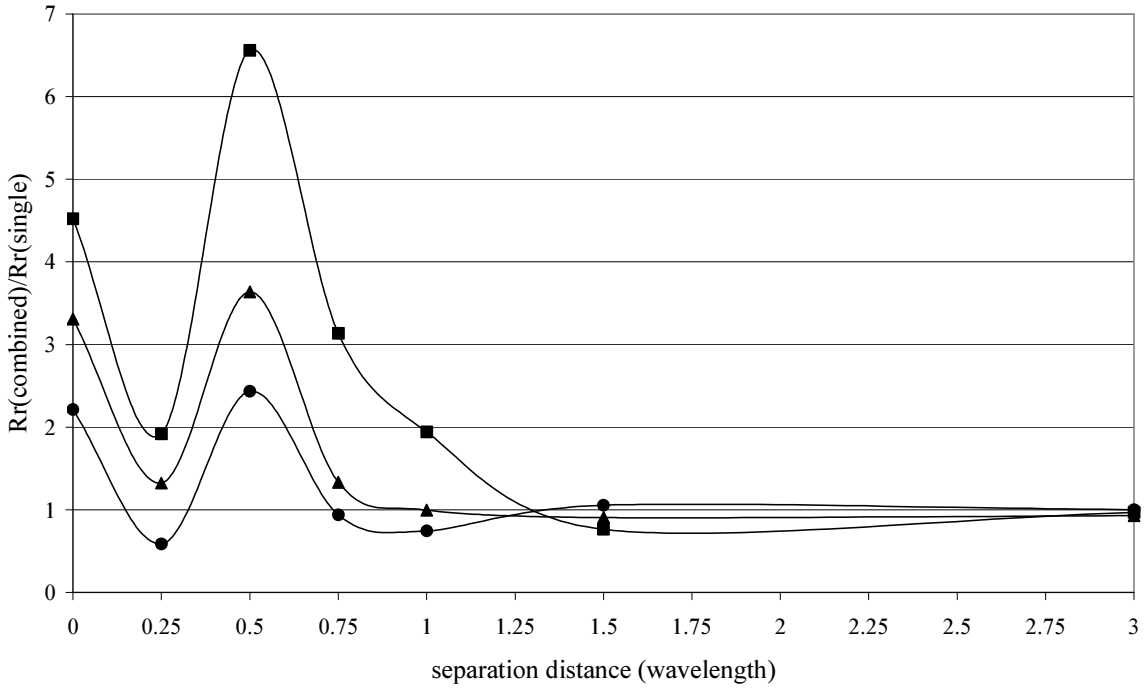

Figure 5.5: Ratio of R_r for a trench-ridge combination to R_r for a single Gaussian trench, as a function of the separation distance, for GWB (square), GWS (triangle) and GWL (circle).

	RT	TR
GWB	0.979	0.763
GWS	1.025	0.907
GWL	0.836	1.035

Table 5.1: Ratio of R_r for a combined feature (with a separation distance of 1.5 λ), to R_r for a single feature.

5.2.2 Transmission

For each combination (RT and TR), R_t values of GWB, GWS and GWL are presented as a function of SD, seen in Figures 5.6 and 5.7 respectively. Because the transmitted wave must here always propagate over a second feature the transmitted amplitude is therefore always a function of this feature and so values of R_t for a combined feature have not compared to those of a single feature, as was done for reflection results in section 5.3.1.

In order to highlight any nonlinear behaviour owing to the presence of a second feature that has contributed to the transmitted wave amplitude, R_t(GWL) values for both the single Gaussian ridge and trench were combined and then subtracted from R_t(GWL), R_t(GWS) and R_t(GWB) results for the combined feature. (Upon combining the ratios of both single features, it was assumed that the SD between the combined features is zero, i.e. no decay in wave amplitude between single features has been accounted for). The intention of this is to show at which SD any linear behaviour in the transmitted wave amplitude arising from the second feature stops. Results for each combination are represented by outlined symbols in Figures 5.6 and 5.7.

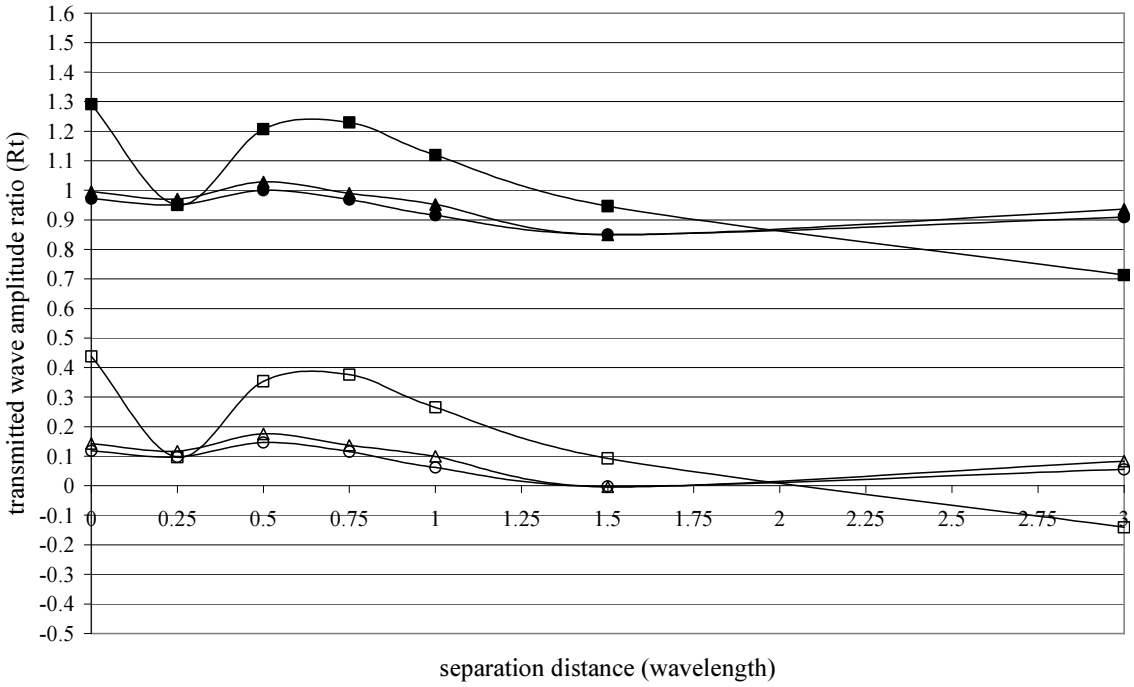

Figure 5.6: Closed symbols (top) represent R_t values as a function of the separation distance, for a wave incident on a Gaussian ridge-trench combination, for GWB (square), GWS (triangle) and GWL (circle). Open symbols represent the result when the R_t values for each single Gaussian features have been combined and subtracted from the R_t values for the combined feature.

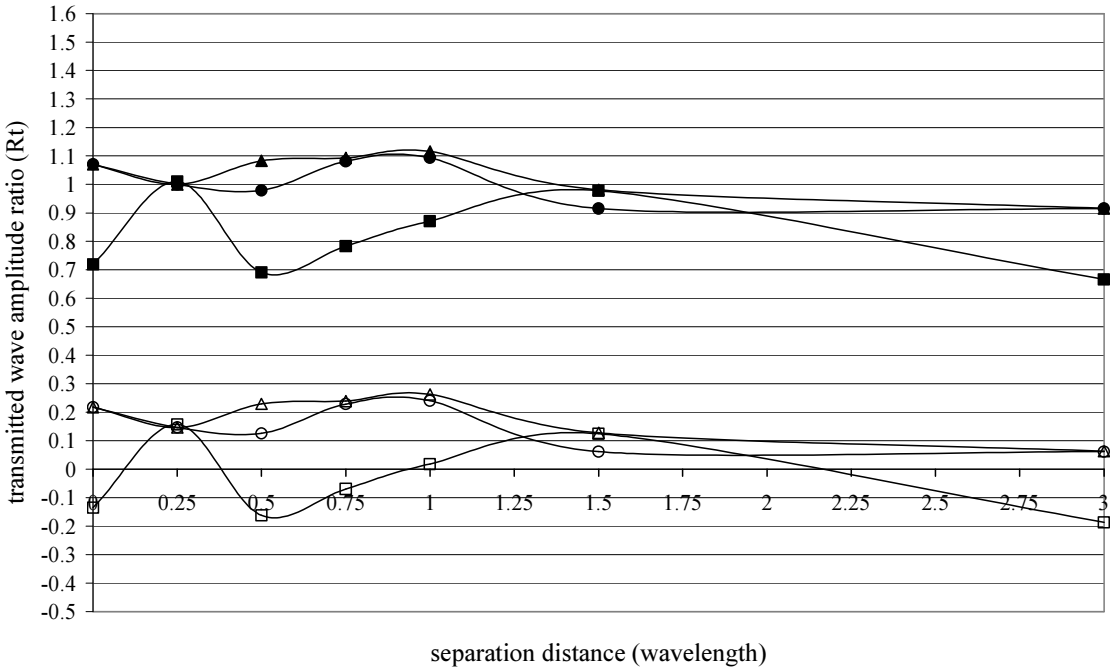

Figure 5.7: Closed symbols (top) represent R_t values as a function of the separation distance, for a wave incident on a Gaussian trench-ridge combination, for GWB (square), GWS (triangle) and GWL (circle). Open symbols represent the result when the R_t values for each single Gaussian features have been combined and subtracted from the R_t values for the combined feature.

On observation of the above Figures, the first point to note is that the R_t(GWL) value for both combinations RT and TR of the combined feature, is larger than that calculated from the combined R_t(GWL) results for a single Gaussian ridge and trench. This is with the exception of SD = 1.5 λ in the RT combination, for which no difference is observed. As shown in Figure 5.7, R_t(GWL) predictions for the wave transmitted over a trench and then a ridge,appears to become constant (~ 0.061) at SD = 1.5λ, suggesting that all linear behaviour owing to the second feature has stopped and that the remaining differences seen in R_t(GWB) and R_t(GWS) are attributable to contributions from the dispersive and or nonlinear terms. For the combination RT with SD = 3λ, R_t(GWL) is 0.055. This suggests that the transmitted wave amplitude ratios for the combined feature

could remain at between 0.055 and 0.061 greater than those of a single feature. This is investigated further at the end of this chapter.

Figures 5.6 and 5.7 show three general behaviours characteristic to both combinations. The first of these is that for each combination, and for each value of SD investigated, GWS and GWL predict transmitted amplitudes which agree to within 4%. An exception is the 11% difference which occurs for the TR combination at SD of 0.5 λ. This 4% agreement is larger than that for a single Gaussian feature, (for a Gaussian ridge, ε = 0.9, it is 2.87% and for a Gaussian trench, ε = 1.1, it is 2.86%). This suggests that the presence of a second feature, situated within all given values of SD for the RT combination (except 1.5 λ), and within all those of the TR combination (except 0 λ, 0.25 λ and 3 λ), will give rise to weakly nonlinear contributions.

The second behaviour is that when SD is 0.25 λ, R_t(GWB) makes a strong deviation towards a value of 1. (It is interesting to note that the lowest values of R_r(GWB), for SD < 1.5 λ, also occur for this value of SD, and for both combinations).

The third behaviour evident is the opposing trend in R_t(GWB) between combinations for SD less than 1.5 λ. For example, for SD = 0 λ in the RT combination, R_t(GWS) and R_t(GWL) are within 0.002 and, R_t(GWB) is 0.30 greater than R_t(GWS) whereas for the TR combination, R_t(GWS) and R_t(GWL) are within 0.001 and, R_t(GWB) is 0.29 less than R_t(GWS).

To determine if neglecting decay upon combining the single feature R_t(GWL) values contributed towards the larger R_t(GWL) value for the combined feature (refer Figures 5.6 and 5.7), the procedure of subtracting these combined single feature values was repeated with the incorporation of a decay factor (refer section 4.3.2) for the different values of SD. Results are plotted in Figures 5.8 and 5.9 and show that with the inclusion of decay, the combined single Gaussian values of R_t(GWL) predict a transmitted amplitude

that is larger than that recorded to pass over the combined feature.

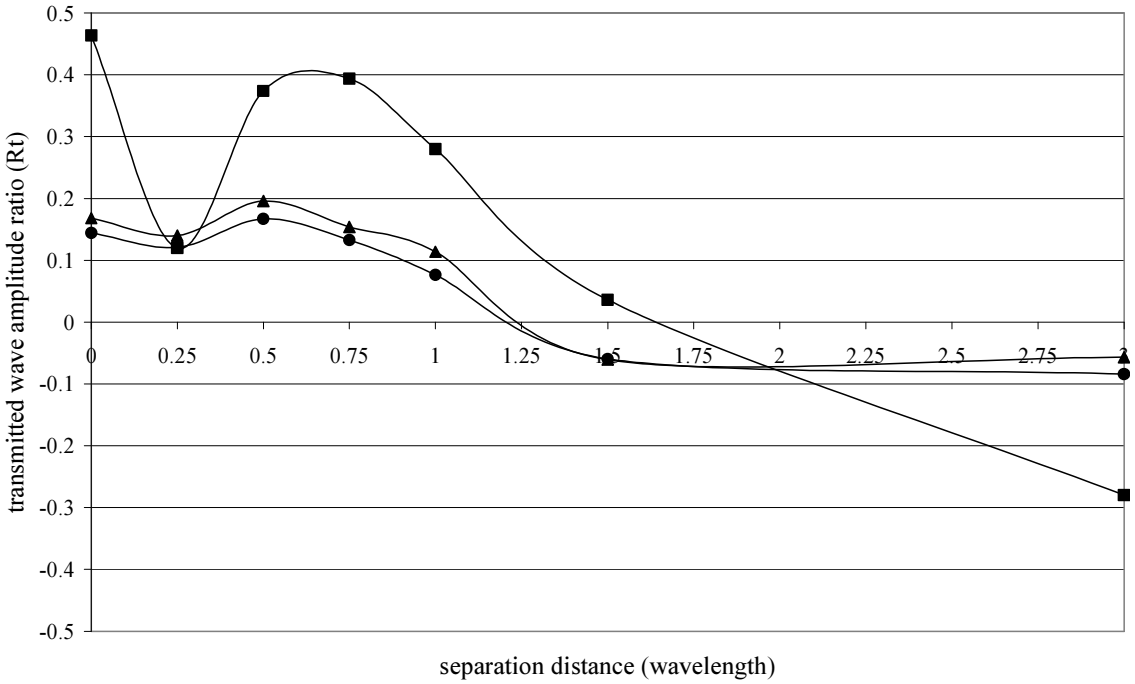

Figure 5.8: Difference between R_t values for the Gaussian ridge-trench combined feature, with and without the incorporation of the calculated decay factor, for: GWB (square), GWS (triangle) and GWL (circle), and the R_t (GWL).

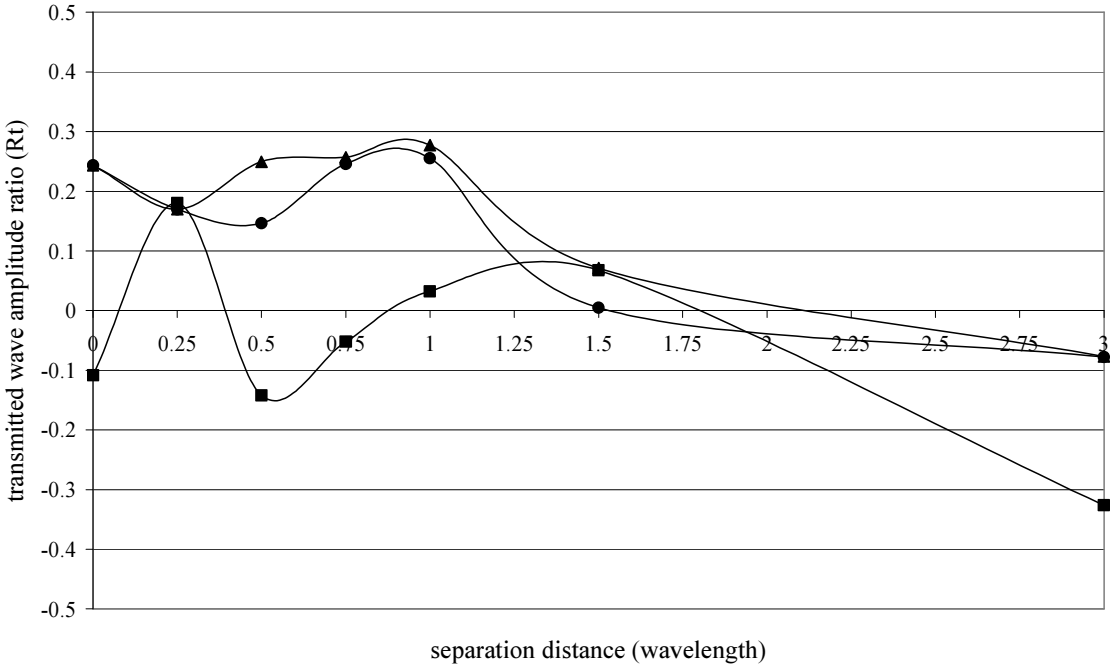

Figure 5.9: Difference between R_t values for the Gaussian trench-ridge combined feature, with and without the incorporation of the calculated decay factor, for: GWB (square), GWS (triangle) and GWL (circle), and the R_t (GWL).

5.3 Conclusions

From this investigation the following conclusions are drawn:

- The reflected amplitude of a wave with dispersive properties incident at a combination of two bathymetric features, is dependent on a second feature located within a distance of 1.5λ (refer to Figure 5.4 and Figure 5.5). Contributions from the fully nonlinear dispersive terms depend most strongly on the distance separating the two features and are of particular significance when the features are separated by 0.5λ.
- The linear dependence of the transmitted wave on a second feature was estimated to end at SD = 1.5λ.
- Slightly larger variations between GWS and GWL transmitted wave amplitude ratios, associated with the combined feature, compared to those for a single feature, show that the presence of a second feature situated within all given values of SD for the RT combination (except 1.5λ) and, within all those of the TR combination (except 0λ, 0.25λ and 3λ), will give rise to weakly nonlinear contributions (refer to Figures 5.6 and 5.7). These values of SD are not characteristic to both combinations.
- Contributions from dispersive terms in GWB, to transmitted wave amplitudes, vary to a significant extent between the two bathymetric combinations (refer to Figures 5.6 and 5.7).

Chapter 6

Numerical Investigation into Tsunami Scattering From a Geophysical Bathymetric Feature

This chapter links the theoretical studies conducted in Chapters 4 and 5 to the geophysical world. Section 6.1 shows how the theoretical work is adapted for this application. This includes the choice of a geophysical bathymetry. Section 6.2 details numerical set-up and simulations. Numerical results are presented in section 6.3. Section 6.4 is a summary which supports the application of the more computationally demanding extended Boussinesq model to a real world tsunami scenario in which the wave has dispersive properties and the bathymetric domain contains gentle sloping features.

6.1 Choice of feature

In order to apply the theoretical studies in Chapters 4 and 5 to the geophysical world, it was necessary to reselect several parameters associated with the idealized bathymetric features. Firstly, a bathymetric feature with a continuous topography will be chosen as this is more realistic in the geophysical world. Secondly, the large values of $\varepsilon = 0.5$ and $\varepsilon = 2$, will not be considered as they represent a more theoretical type of feature. Instead a feature with the smaller values of $\varepsilon = 0.9$ or $\varepsilon = 1.1$, will be chosen. Lastly, a single feature which satisfies the experimental parameters in Chapters 4 and 5 is easier to find than a combination of two and is therefore the preferred choice.

It is important to emphasize that the above single feature can be found in real bathymetric depths. The most accessible bathymetric data set in which to discover this

feature is the ETOPO2 database (Smith and Sandwell, 1997). This data set has a grid cell spacing of 2-arc minutes. In order to match the water depth to wavelength ratio used in Chapters 4 and 5 (so as to provide a wave with the same dispersion properties as given in 4.2.3) whilst using a feature resolved by a minimum of three bathymetric data points, the feature must be selected from the deep ocean. This allows for the wavelength (which satisfies the features standard width) to be equal to the ocean depth at time $t = 0$.

In the case that there is finer resolution bathymetry available for an ocean region, double features (which satisfy the above criteria) would be easier to locate. This would allow for correlations between model predictions in this region and the behaviour's observed in Chapter 5.

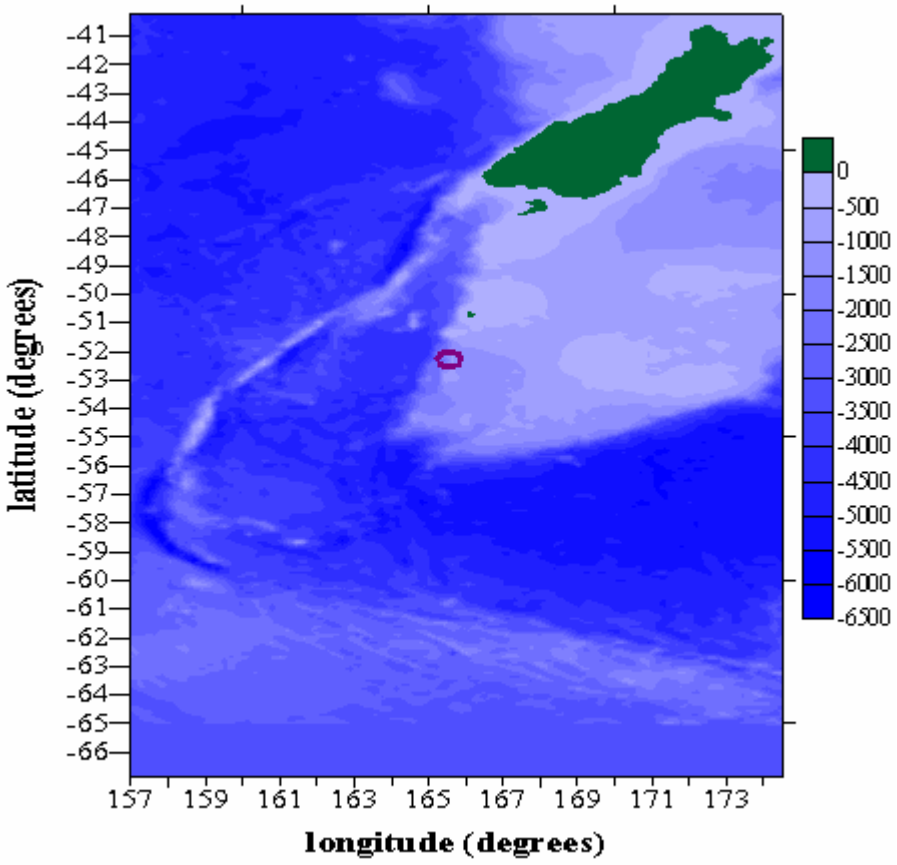

Figure 6.1: The unique combination of bathymetric features in the region south of New Zealand. The submarine Macquarie Ridge can be seen to extend southwest from the South Island. The colour bar represents depth in metres. The purple outline encloses the chosen feature (as discussed below).

The region south of New Zealand (Figure 6.1) is selected as the area from which the feature will be chosen. This choice was motivated by its proximity to New Zealand and its varied combination of submarine features. These include mountain ridges, a deep-water trough and shallow water plateaus. An added advantage of this domain is that the mountain ridges have the possibility of generating a tsunami by means of a submarine landslide, or slump.

The feature selected for this study is an escarpment. Its location is encompassed by the purple outline in Figure 6.1. The real data points which depict the feature are plotted in Figure 6.2 below. A possible wave source is assumed to be in the region of the Macquarie Ridge. Therefore, with respect to a potential wave, incident on the feature, the escarpment is described as upwards sloping with a depth parameter of $\varepsilon = 0.9$.

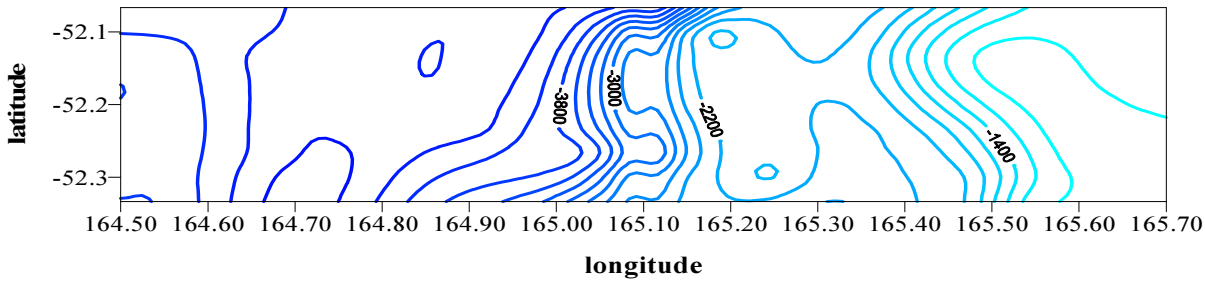

Figure 6.2: Contour plot representing the bathymetric data obtained from ETOPO2 (Smith and Sandwell, 1997) in which a geophysical escarpment, analogous to that in section 4.4.4 was found. Contours are at 200 m intervals.

Equation 4.7 and MATLAB were used to convert the distance between the upper and lower levels of an escarpment to a function of the wavelength. The result was a distance equivalent to 1.6 times the wavelength. This result shows that the chosen escarpment is analogous to the idealized escarpment in section 4.4.4. On reference to Figure 6.2, it is seen that the lower level of the escarpment is at a depth of approximately 4000 m. Assuming a wavelength of 4500 m, the distance between the lower and upper levels can be calculated as 0.095 of a degree of longitude. As ETOPO2 has a grid cell

spacing of 2-arc minutes the feature is represented by 2.9 (~ 3) 'real' data points. The 4500 m wavelength was assumed based on the existence of nearby potential mechanisms for generation of a wave with dispersive properties (such as the aforementioned Macquarie Ridge).

6.2 Numerical set up and simulations

Numerical domain

The finite difference grid required for numerical simulations was developed from the data presented in Figure 6.2 by means of a radial basis function gridding method. This method was used because the radial basis functions are exact interpolators and a much smoother grid is produced, see Figure 6.3.

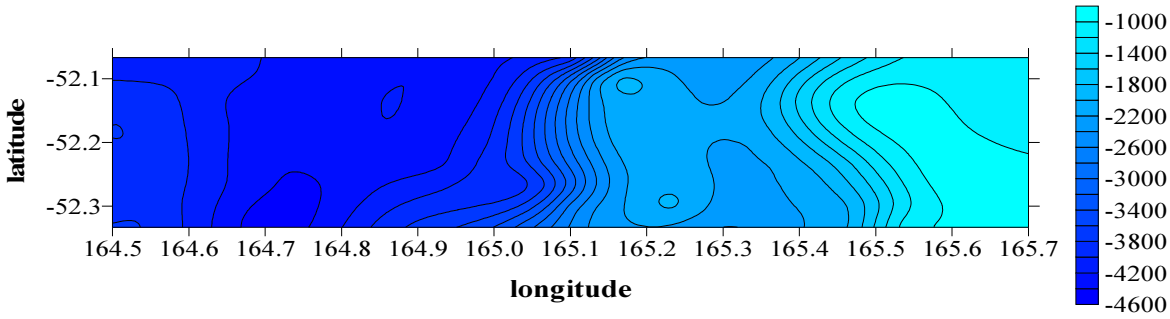

Figure 6.3: The finite difference grid developed from the data presented in Figure 6.2 by means of a radial basis function gridding method. Note, axis values are given as the degree of latitude or longitude followed by a decimal fraction of a degree. The distance separating the two most significant levels is observed to be between 165.06 and 165.16. This is approximately 1.6 times the assumed wavelength.

Initial Conditions

As the feature is located in an open ocean domain, the water depth to wavelength ratio used in Chapters 4 and 5 is satisfied. However, as a result of this, the wave amplitude corresponding to the wave amplitude to water depth ratio in Chapters 4 and 5 is unrealistic. Instead, that of amplitude of a typical tsunami which propagates the open ocean is assumed. As stated in Chapter 2, this amplitude is commonly less than 0.5 m

(Hammack, 1972). Accordingly, the amplitude of 0.2 m from Chapters 4 and 5 is retained. As mentioned in section 6.1.1, the initial depth and wavelength are both 4000 m. The initial velocity profiles of zero and the ten grid nodes per wavelength also stay the same as in Chapters 4 and 5. The resolution in both horizontal directions is 336 m. Propagation was in the positive x direction. For computational reasons the number of nodes allocated to the sponge layer is 1.9 wavelengths.

This study only considers the transmitted wave amplitude predicted by GWB, GWS and GWL. This is for two reasons: the real world context, for which the transmitted wave amplitude is assumed to be most significant and, the fact that reflection ratios for the single idealized feature with ε = 0.9 and ε = 1.1 are small.

Numerical results for the transmitted wave amplitude R_t were obtained using the same methods and equations as in section 4.3 of Chapter 4. As previously defined, R_t is the ratio of the transmitted wave amplitude A_t to the incident wave amplitude A_0. As the numerical wave gage locations are dependent on the initial wavelength, the new locations for this study are as follows. The gage to record the transmitted wave amplitude A_t is located 800 m into the higher level of the escarpment. The gage to record the initial wave amplitude A_0 is located at the beginning of the lower level of the escarpment. As discussed in section 4.3.2, R_t for the above geophysical escarpment (Figure 6.3), has been divided by R_t for a numerical domain with a constant depth of 4000 m. This ensured that R_t for GWB, GWS and GWL is representative of the wave interaction with the geophysical escarpment and that it does not depend on the propagation distance or the water depth prior to this interaction.

Because the focus of this chapter is on a real world application, it is the results output by GWB, GWS and GWL that are of importance. Therefore, any decay in wave

amplitude occurring between the gages at which the incident wave amplitude and the transmitted wave amplitude were measured, was excluded.

As the ratio of water depth to wavelength, which matches that in Chapters 4 and 5, was satisfied but the ratio of wave amplitude to water depth was not, it was hypothesized that any differences between R_t (GWB) and R_t (GWS) are contributions from the dispersive terms, or the fully nonlinear terms in GWB, due to nonlinear interactions associated with the dispersed waveform.

6.3 Numerical results

R_t values for GWS and GWB are presented in Table 6.1. R_t (GWB) is observed to be a factor of ~ 2 smaller than R_t (GWS). With respect to the 'real world' context of this investigation, the transmitted wave amplitude predicted by GWB was calculated as a percentage of that predicted by GWS. The result is that GWB predicts a transmitted wave amplitude 22% less that GWS. With the background knowledge from section 4.4.4, this smaller value predicted by GWB was expected. As before, it was caused by the continuous gradual depth change characteristic to the feature, which caused an increase in the dispersion of the wave as it propagated over this feature. As a result there was less energy in the main transmitted wave front.

	GWS	GWB
R_t	0.9631	0.4701

Table 6.1: Transmitted wave amplitude ratios for GWS and GWB for a wave with dispersive properties incident on an upwards sloping geophysical escarpment. Any decay attributable to the numerical approach and that occurred between the gages where the incident wave amplitude and the transmitted wave amplitude was measured, is excluded.

As hypothesized in section 6.2, the difference between R_t values of GWS and GWL (refer Table 6.2 below) is minute and can be seen in the 4th decimal place. This indicates that there have been no significant nonlinear contributions from GWS and suggests that any nonlinear contributions in GWB were associated with the dispersed waveform.

	GWL	GWS
R_t	0.9630	0.9631

Table 6.2: Reflected wave amplitude ratios for GWL and GWS for a wave with dispersive properties incident on an upwards geophysical escarpment.

A comparison of R_t (GWS) values for the 'real feature' with those for the 'idealized feature', refer Table 6.3 below, shows the former is 0.85 of the latter. The difference was attributed to two factors. The first is the small ratio of the wave amplitude to the wavelength used in this real geophysical problem. The second is the exclusion of the correction for decay which incorporates any decay resulting from the numerical approach.

	GWS (real escarpment)	GWS (idealized escarpment)
R_t	0.9631	1.1258

Table 6.3: Comparison between GWS transmitted wave amplitude ratios, for a wave with dispersive properties incident on; an upwards sloping geophysical escarpment and on an idealized escarpment.

6.4 Summary

This chapter provided a link between the theoretical studies of Chapters 4 and 5 and the geophysical world. GWB, GWS and GWL were used to simulate a hypothetical tsunami

wave with dispersive properties across an upwards sloping geophysical escarpment. Results show that the transmitted wave amplitude predicted by the computationally demanding fully nonlinear extended Boussinesq model (GWB) is significantly smaller (by ~ 22%) than that of the less demanding, nonlinear shallow water model (GWS).

This difference supports the application of the more computationally demanding Boussinesq equations to a geophysical tsunami scenario in which the wave has dispersive properties and the bathymetric domain contains gentle sloping features described by a depth variation of $\varepsilon = 0.9$ or $\varepsilon = 1.1$.

Chapter 7

Real World Application of the Numerical Model Geowave V1.0

This chapter serves two purposes. The first, presented in sections 7.1 to 7.3, is to record an investigation and evaluation into the applied real world ability of the fully nonlinear extended Boussinesq tsunami generation and propagation model Geowave V1.0 - revised (Watts, 2002). The second (presented in section 7.3), is to provide a discussion of the issues involved in the application of a numerical model to a geophysical tsunami problem. A summary of the chapter's findings are presented in section 7.4.

Other real world applications of Geowave found in the literature are near field investigations of; debris flow in a reservoir lake (Walder, 2006), submarine mass failure (Watts, 2003) and, the 2004 Indian Ocean Tsunami (Watts et al., 2005). This motivates the work presented in sections 7.1 and 7.2 of this Chapter. Recalling the definitions of the various propagation equation sets of Geowave V1.0 to be used in this chapter, we have; the weakly nonlinear shallow water equations – GWS and the fully nonlinear extended Boussinesq equations – GWB.

Section 7.1 presents Geowave propagation results for a near field, intermediate depth, tsunami wave event for which the 1998 Papua New Guinea submarine slump is used as the generation mechanism. Prior success of Geowave in its application to this event (Watts et al., 2003) is the reason for its use in this research where, in order to highlight contributions from nonlinear dispersive terms, Geowave results are compared with GWS (Geowave with wave propagation based on the nonlinear shallow water equations). Section 7.2 is motivated by an available numerical comparative study, Walters (2002). It

investigates the ability of Geowave to predict wave evolution and amplification of a shallow water tsunami wave in a hypothetical far field tsunami event.

7.1 A near field intermediate depth tsunami wave

The purpose of this section is to investigate the application of Geowave to a near field tsunami event occurring in a bathymetric domain which has a substantial variation in depth. This variation causes the initial surface disturbance to propagate as a deep water (dispersive) wave at the source and a shallow water (non dispersive) wave nearer the coast. The tsunami resulting from the 1998 Papua New Guinea (PNG) submarine slump event is chosen for simulation as it satisfies the above criteria. From the specifics on Geowave (refer to Chapter 3), it is seen that, due in particular to the finite difference scheme, the combination of this tsunami scenario and bathymetric domain ought to be where Geowave is most successful. The application of Geowave to the PNG event in this section differs from that in Watts et al. (2003) in that run up is not calculated and that GWS results for this event are compared with those of Geowave

7.1.1 Model set up

The bathymetric data comes from the PNG grid provided with the Geowave source code, courtesy of Phil Watts of Applied Fluids Engineering, Long Beach, CA. For the purpose of this numerical work, the PNG grid was extended on all four sides to include sponge layers 1.9 wavelengths in thickness. The resulting grid dimensions are $141.619°$ to $142.681°$ E and $-3.431°$ $-2.319°$ S. The grid was then discretized into 585 x 615 uniform cells, of horizontal width 200 m.

The initial surface (Figure 7.1) is based on the hypothesized PNG slump mechanism (Heinrich et al., 2000; Tappin et al., 2001; Synolakis et al., 2002; Watts et al.,

2002) and was constructed using the initial conditions tool TOPICS (Watts, 2002). (Note that this tool is part of Geowave. For further information refer to Chapter 3). Input parameters for TOPICS were taken from the website www.tsunamicommunity.org. The initial velocity profiles were zero.

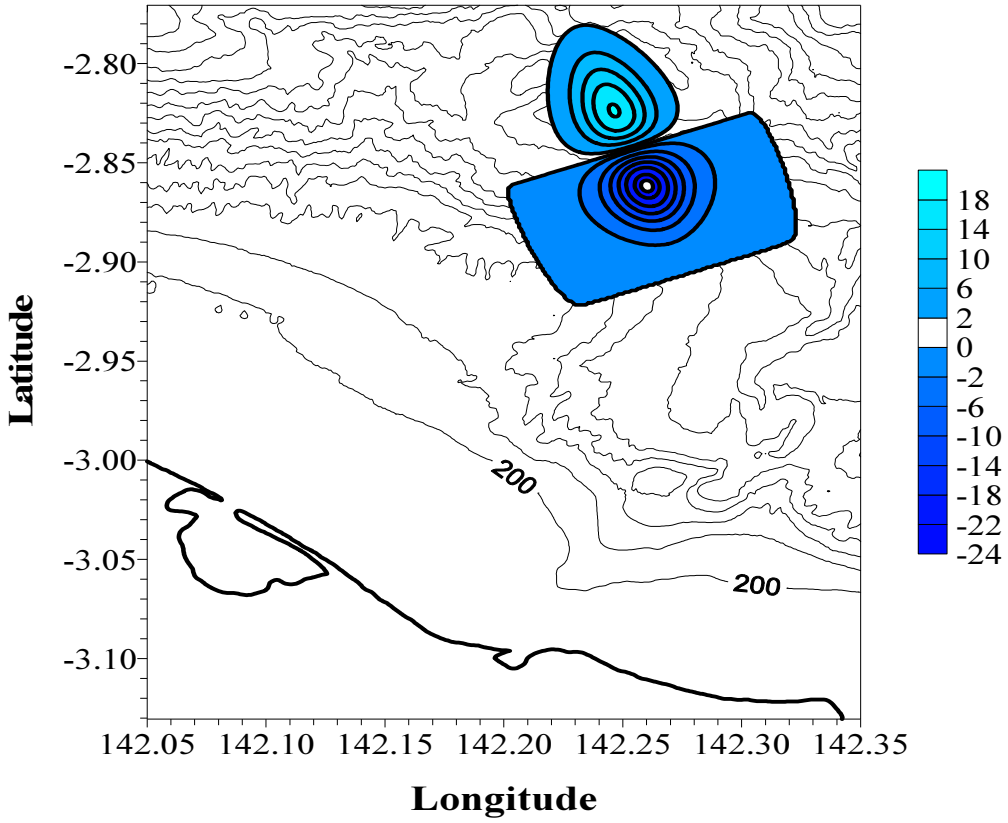

Figure 7.1: Initial Surface, Sissano Lagoon, Papua New Guinea. Its dimensions are: 141.619° to 142.681° E and −3.431° −2.319° S. The colour bar represents depths in meters. Contours are at 200 m intervals.

7.1.2 Numerical Results

The surface elevation output after 1, 3 and 7 minutes of wave propagation time (Figure 7.2), illustrates that the waveform predicted by GWS remains as localised, distinct and single. A discontinuity in this waveform is seen perpendicular to the entrance of Sissano Lagoon. As opposed to this, the Geowave waveform shows that dispersion affects

introduced in the source region have altered the waveform and as a result, several wavelengths now exist.

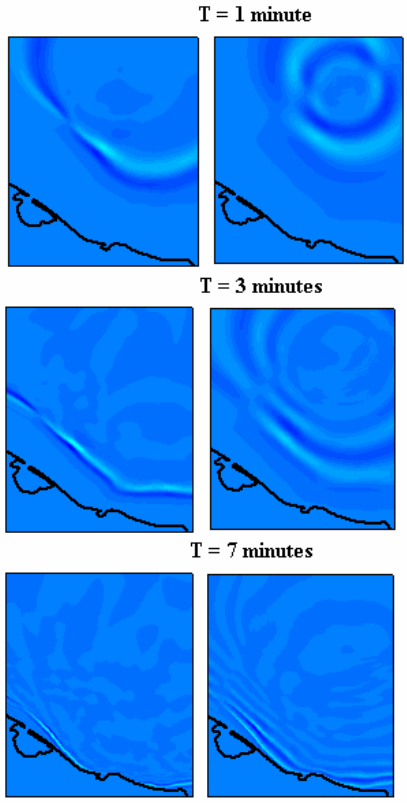

Figure 7.2: Waveform predicted by GWS (left), and Geowave (right), after a wave propagation time of 1 minute (top), 3 minutes (middle) and 7 minutes (bottom).

To highlight the contribution from the fully nonlinear extended Boussinesq terms to the weakly nonlinear shallow water equations (GWS), the maximum surface elevation for GWS is plotted in Figure 7.3 (a) and the difference between this elevation and that predicted by Geowave, is plotted in Figure 7.3 (b).

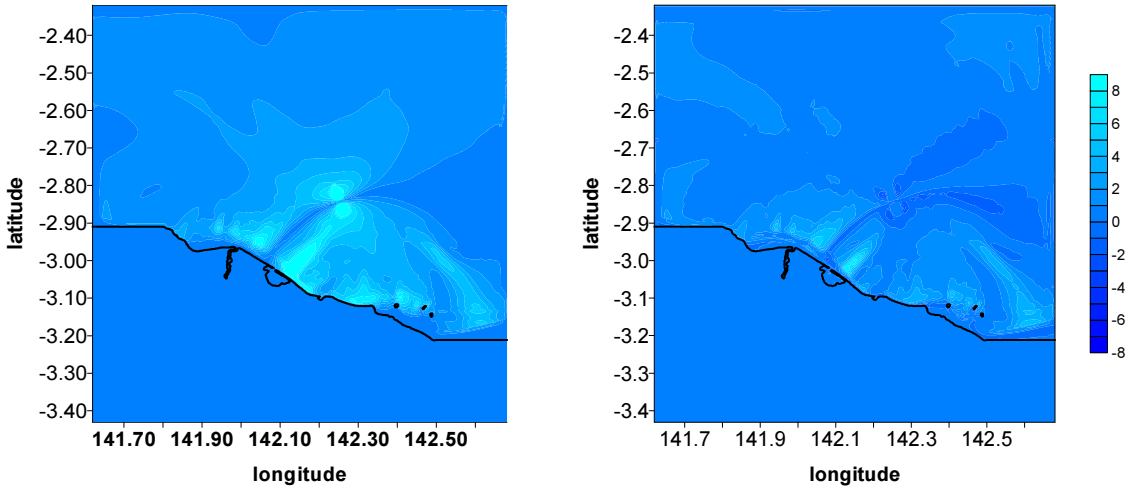

Figure 7.3 (a and b): Maximum GWS predicted surface elevation (left) and the difference between the maximum predicted surface elevation of GWS and Geowave (right). Note that the right figure the lighter blue indicates that the predicted amplitude of GWS is greater than that of Geowave. Scale is in metres.

To further emphasize the contributions of the fully non linear extended Boussinesq terms to GWS time series taken from three numerical wave gages, (see locations in Figure 7.4), are presented in Figure 7.5.

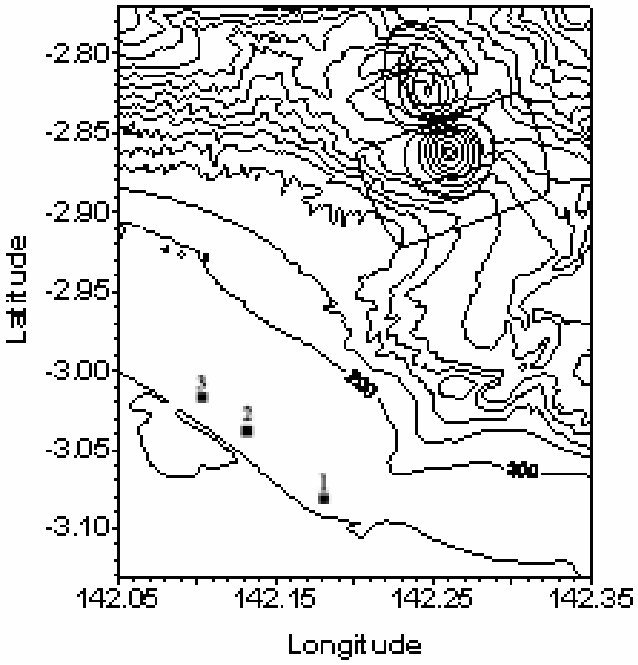

Figure 7.4: Diagram illustrating the approximate positions of the three wave gages located at the exact longitude latitude coordinates; Gage 1: (142.185 -3.06), Gage 2: (142.13 -3.02) and Gage 3: (142.10 -3.0). Both the idea of this diagram and the approximate wave gage locations were taken from Lynett et al. (2003).

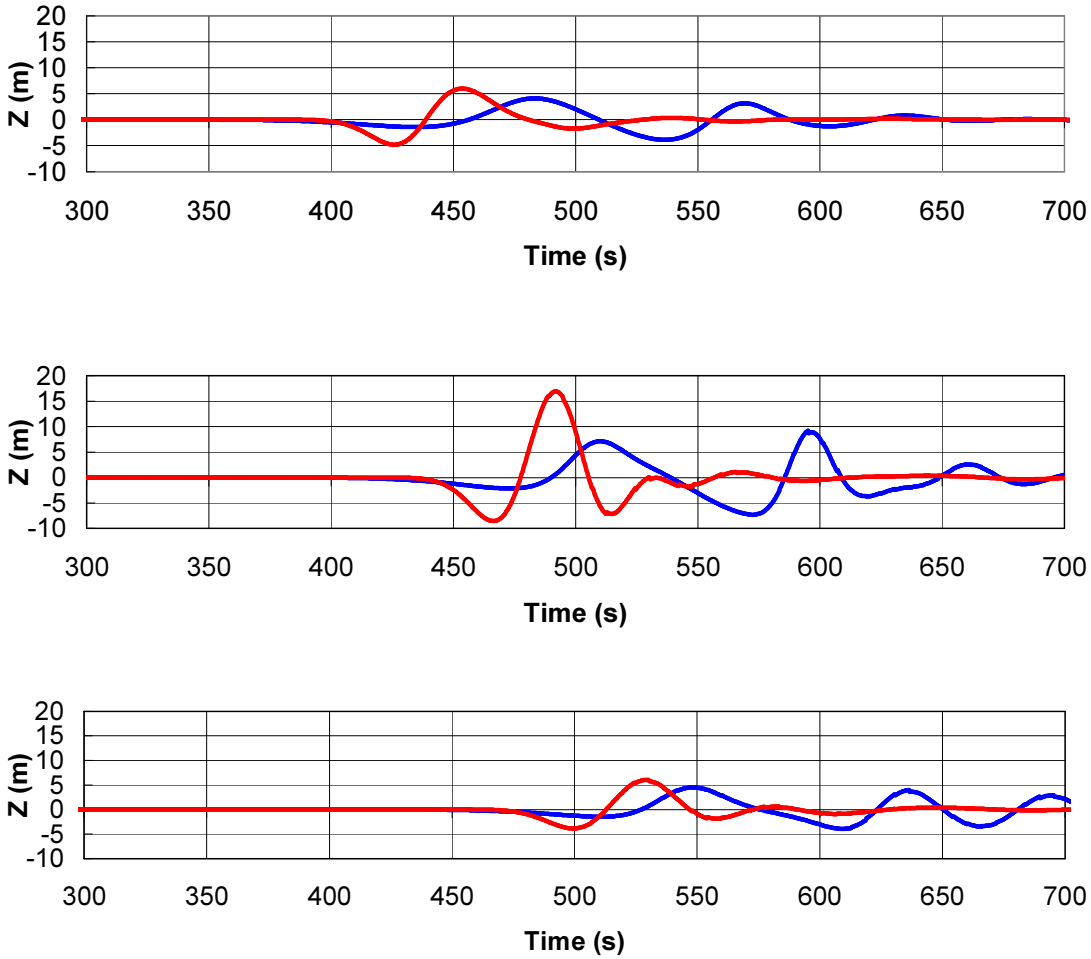

Figure 7.5: Predicted surface elevations Z, by GWS (red) and Geowave (blue), at wave gages 1 (top) 2 (middle) and 3 (bottom).

All three time series show the GWS wave to arrive between 20 and 30 seconds earlier than that of Geowave. Both Geowave and GWS predict the wave to arrive at the Gages in the order 1, 2 then 3. On reference to the bathymetry in 7.4 and, recalling the image in Figure 7.2, the wave appears to be channeled by the bathymetry. The highest initial wave amplitudes are predicted by both GWS and Geowave to occur at Gage 2. Of these, GWS is the largest by 130%. This is due to the absence of the dispersive Boussinesq terms in GWS, meaning a greater proportion of the initial energy remains in the main GWS wave front. Hence, there is more energy to be transferred into the wave's amplitude as it shoals on approach to shallower water.

The ratio of the computational time of GWB and GWS, for the above simulations is 2.13.

7.1.3 Conclusions

This section has emphasized the abilities of Geowave to predict wave propagation for a near field, dispersive tsunami. Contributions from the fully nonlinear extended Boussinesq terms in Geowave during propagation of a 'dispersive' wave form were highlighted by the comparison of Geowave and GWS results.

7.2 A hypothetical far field non dispersive tsunami wave

As section 7.1 demonstrated Geowave's ability to predict propagation of a dispersive wave, this section focuses on propagation of a shallow water (non dispersive) wave in a far field domain. Its aim is to investigate the hypothesis that Geowave has the ability to predict a) propagation of a non dispersive wave and b) wave amplification in a far field event. This investigation follows the numerical work presented in Walters (2002).

This study was motivated by two factors. Firstly, all previous applications of Geowave published in the literature relate to near field events, with the exception of Watts et al. (2005) in which the domain has a horizontal extent of c. 6 degrees longitude, (which could almost be described as a far field domain). By comparison, the domain in the current study is clearly far field in that its horizontal extent is tens of degrees longitude. The second ground for motivation, is the available literature for comparison of Walters (2002) in which long wave resonance along the East coast of New Zealand is examined for a spectrum of long wave periods.

7.2.1 Study domain

This study focuses on wave amplification along the East coast of New Zealand. The numerical domain of interest is the region from 23.75°S to 65°S, and 156.75°E to 210°E (Figure 7.6).

The bathymetric data used in this study was provided by Roy Walters (of the National Institute for Water and Atmospheric Research, Christchurch, New Zealand) and comes from three sources: the Royal New Zealand Navy Hydrographic Office; the National Institute of Water and Atmospheric Research (NIWA), and the bathymetry archive of Smith and Sandwell (1997) (Refer Walters, 2002 for further detail).

7.2.2 Model set up

Locations of resonance predicted by Walters (2002) along the East coast of New Zealand were most predominant for the 150 minute period wave. As the boundary conditions of Walters (2002) are time dependent and those of Geowave are not, simulations in Geowave use a wave train composed of three monochromatic sinusoidal waves to approximate the infinite train wave in Walters (2002). Due to the computational limitations associated with a Boussinesq model, as well as Geowave's boundary conditions, simulations involving multiple wavelengths with a 150 minute period were not feasible. Instead, two wave periods of 60 and 75 minute were chosen, with results of Walters (2002) indicating that a significant number of resonance locations along the east coast of New Zealand were still observable.

Thus, the western boundary used to define the finite difference grid of Geowave was the same as Walters (2002), i.e 23.75°S to 65°S, at 156.75°E. However, in order to incorporate the initial wave form, the eastern boundary was assumed to be located at 256.31°E and 260.16°E for the 60 and 75 minute wave train respectively, refer Figure 7.6.

The finite element grid of Walters (2002) is discretized into 32065 nodes, with a variable horizontal spacing of between 98 km near the open ocean boundary and 300 m near the coast. Due to the computational demands of a Boussinesq model and, the factor of a finite difference grid, the resolution of Geowave's numerical grid for this far field application must be both relatively coarse and uniform (the Geowave finite difference grid provides a greater numerical stability when a maximum size difference of 5% exists between horizontal nodes, Watts, 2002). Thus, for simulations within this case study the horizontal grid spacing is 26.8 km and 27.2 km (in the *x* and *y* directions respectively). This also results in approximately the same number of nodes as in Walters (2002).

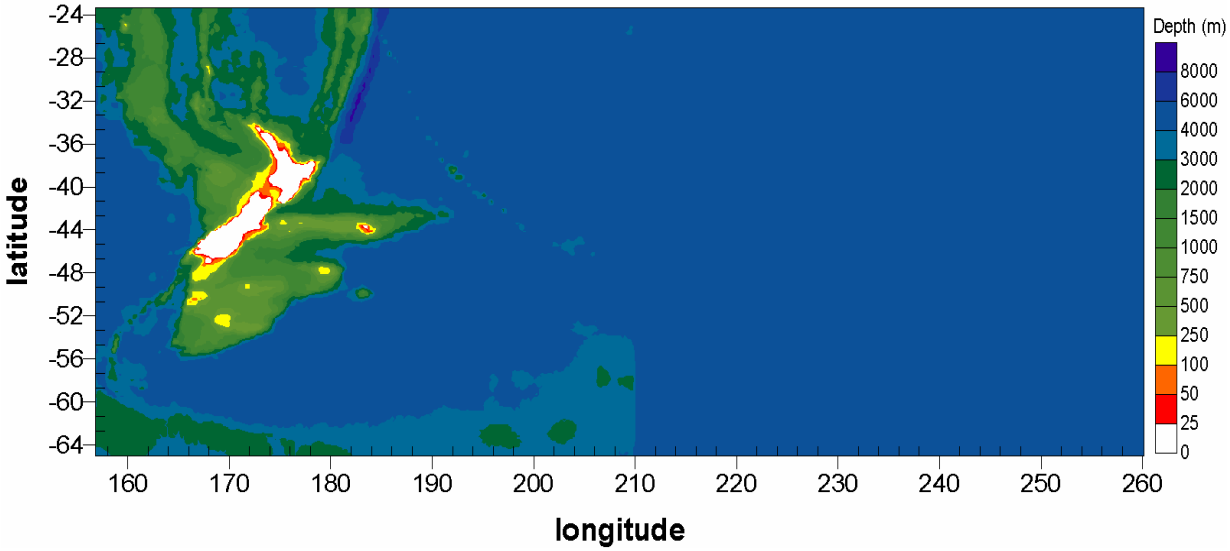

Figure 7.6: The numerical domain for the 75 min. period wave train. Note the extended, idealized, flat bottomed bathymetry from 210°E eastwards.

The initial wave train was assumed to be located at the eastern boundary of the region of interest where the average depth was c. 4500 m. This depth was then used to extend the computational domain eastwards over an idealised, flat bottom, topography in order to minimise distortion of the initial waveform as it propagated westward into the

domain of interest. Following Walters (2002), the initial amplitude was 0.01 m. The initial velocity was assumed to be zero.

To minimize reflections from the boundaries, sponge layers of 1.2 wavelengths were placed around all four sides of the domain.

7.2.3 Results

In the following results, any wave decay associated with long propagation distances over the extended bathymetric region, was taken into account by use of an amplification factor. This factor scales the coastal wave amplitudes with respect to the average wave amplitude at the eastern edge of the domain of interest. It must also be noted that resonance predicted by Geowave for the Southern coast of the South Island of New Zealand was not considered due to possible boundary influences.

Figure 7.7 compares regions of amplification as predicted by Geowave (Figure 7.7 A & C) with those of Walters (2002) (Figure 7.7 B & D). Results indicate that there is in general, good agreement with respect to areas associated with wave amplification, along the East coast of New Zealand. However, significant discrepancies exist with respect to the degree of amplification. For example, agreement of up to 80% was observed in the region of Napier (Figure 7.7 A). Nevertheless, for most areas, the agreement is less than 10%; for example, in the region north of Gisborne (Figure 7.7 A).

Two factors which influence this agreement are; firstly the use of an approximated infinite wave train and secondly, the coarse grid resolution in coastal regions, associated with the regular, finite difference grid.

The effect of the first factor is that resonances of more than 3 wavelengths away from a point of reflection, will not be captured by this Geowave simulation. For the 60 and 75 min. period wave this is analogous to 2268 km and 2835 km eastwards from a point of reflection along the New Zealand coastline. As both these distances extend past the

Chatham Islands, the approximated wave train is not considered to be the most significant factor contributing to the limited number of resonance locations captured by Geowave.

However, two reasons point towards a significant contribution from the second factor. Firstly, both the 60 and 75 minute period waves in the domain (Figure 2) are theoretically, shallow water waves (water depth/wavelength < 0.05). A comparison between Geowave surface elevations (Figure 7.8), over a relatively uniform depth (before the wave's westward approach to the Chatham Rise) and over a much shallower depth (on the Chatham Rise) confirms Geowave maintains the shallow water wave form during propagation. Hence, the largest difference between models is the length of the wave train and the grid resolution.

The second reason is the good qualitative agreement of the predicted wave amplification between Geowave and Walters (2002) where grid resolution is comparable. The best example of this is in the region of the Chatham Islands and Chatham Rise where amplification agreement can reach 100%.

This comparison may be more meaningful if the results compared were based on the same grid resolution. However, as the model in Walters (2002) uses the finite element method for grid discretization this could not be achieved for this study.

Furthermore, it is important to stress that the locations of coastal resonance shown in this study may vary for a different combination of sinusoids. This is because the induced phase shift of the sinusoids on approach to very shallow coastal waters is dependent on their initial frequency (Synolakis, 2003).

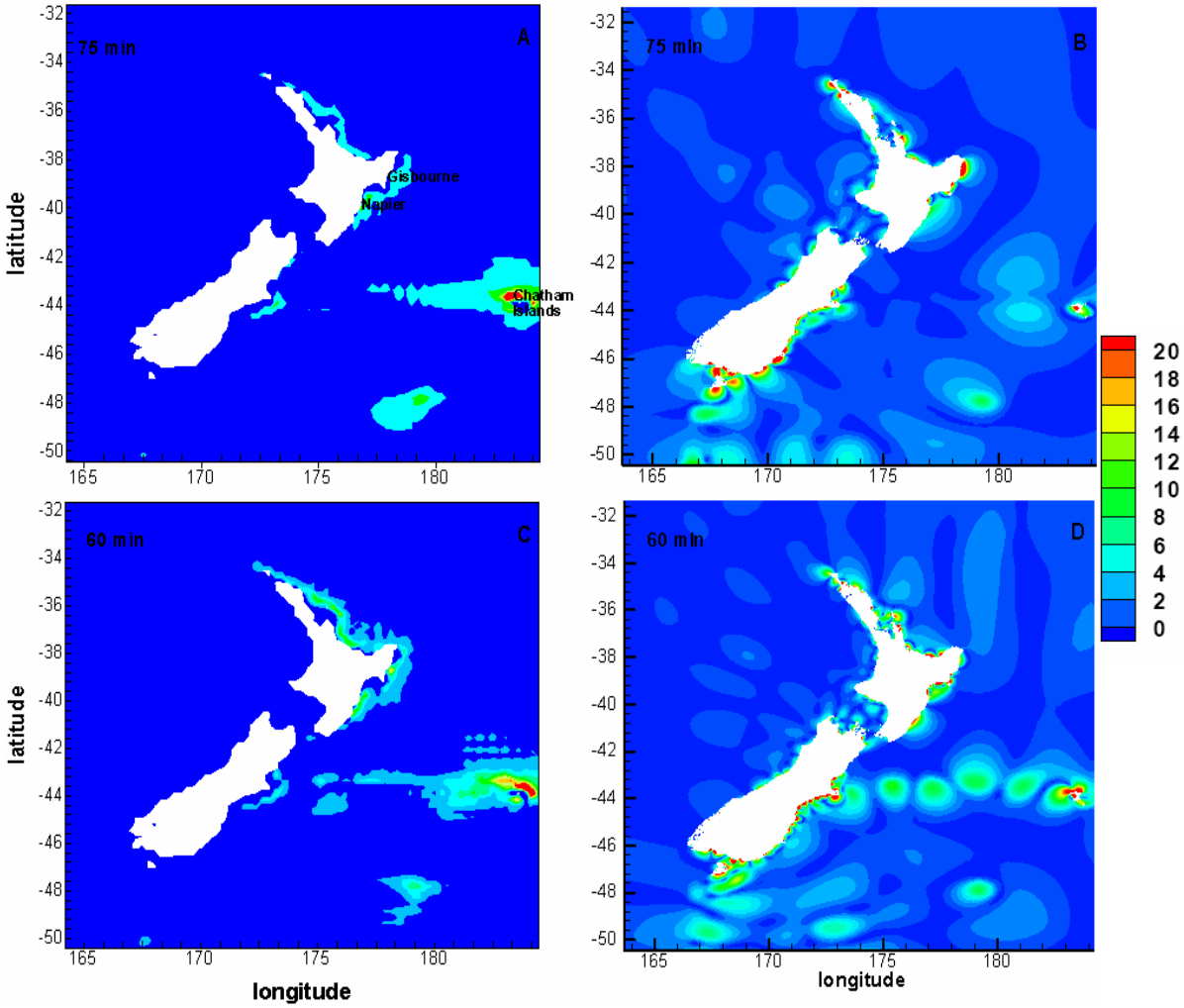

Figure 7.7: Maximum surface elevation plots illustrate resonance hotspots for Geowave (left) and of Walters (2002) (right), for a wave-train incident from the eastern boundary, composed of three 75 min. period waves (top) and three 60 min. period waves (bottom). The colour bar represents the factor of wave amplification.

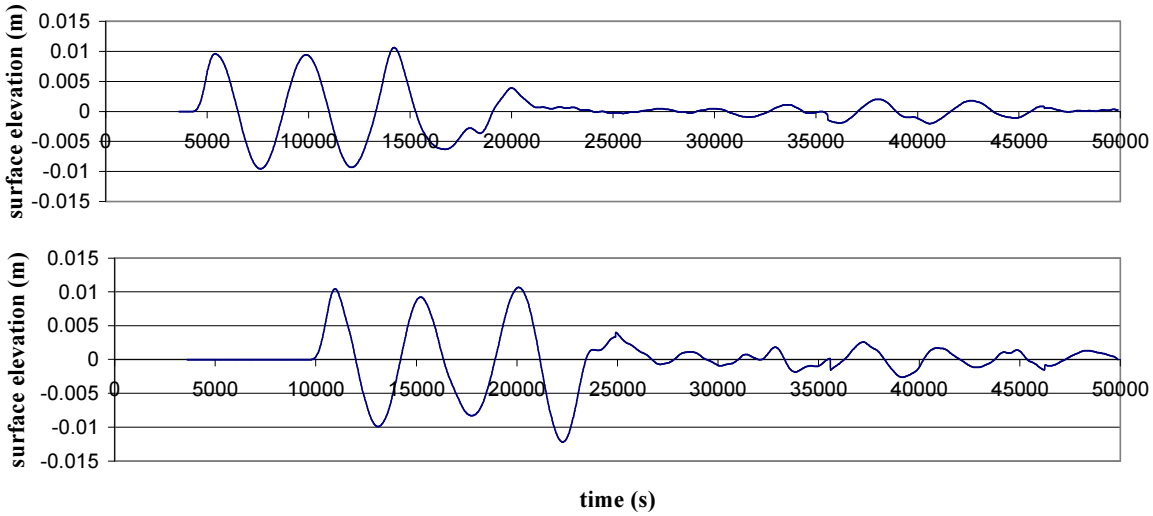

Figure 7.8: Geowave time series of water surface elevations before the wave's westward approach to the Chatham Rise (top) and on the Chatham Rise (bottom).

7.2.4 Conclusions

In summary of this section, the application of Geowave V1.0 – revised, to a far field event has highlighted firstly, that its extended Boussinesq equation sets are capable of predicting wave evolution for a shallow water wave and secondly, based on monochromatic results, that it has the ability to capture locations of possible resonance in a hypothetical far field tsunami event. And although limited by grid resolution (owing to the finite difference numerical scheme and the Boussinesq type model) that it does provide direction for future, higher resolution, smaller scale studies. Nonetheless, this coarse grid resolution resulted in numerical predictions that show no advantages in the application of a Boussinesq type of model, to this size of domain, over that of a faster shallow water model such as MOST (e.g. Titov et al, 2005b) or TSUNAMI-N2 (Imamura, 2004), or the Reynolds-averaged Navier-Stokes model RiCOM (Walters, 2005).

The ratio of the computational time of GWB and GWS, for the 60 minute period wave simulation above, is 1.75. N.B. this ratio is larger than when simulating propagation of a non dispersive tsunami wave (refer last paragraph of section 7.1).

7.3 A discussion of the issues surrounding the choice of numerical model based on the particular geophysical application.

This section discusses the issues that must necessarily be considered when deciding which type of numerical model is best suited for a study of tsunami as determined by the particular geophysical application. These issues are both physical and numerical in origin and include:

- The source of the tsunami (near or far field) as this provides an indication of its wavelength.
- The bathymetric characteristics of the study region.

- Properties of the wave including whether it is sufficiently characterised as dispersive or non dispersive, and linear or nonlinear
- Are either run up or inundation to be considered?

(For a brief discussion on the benefits of the inclusion/exclusion of the aforementioned factors the reader is referred to section 2.4.1). The first two of these issues can significantly influence the type of model that could be most suitable in predicting tsunami wave evolution.

The bathymetry that surrounds New Zealand (Figure 7.9) provides examples of the wide range of submarine bathymetric features that exist. The numbered boxes refer to a bathymetric region or feature of interest. These are listed below Figure 7.9.

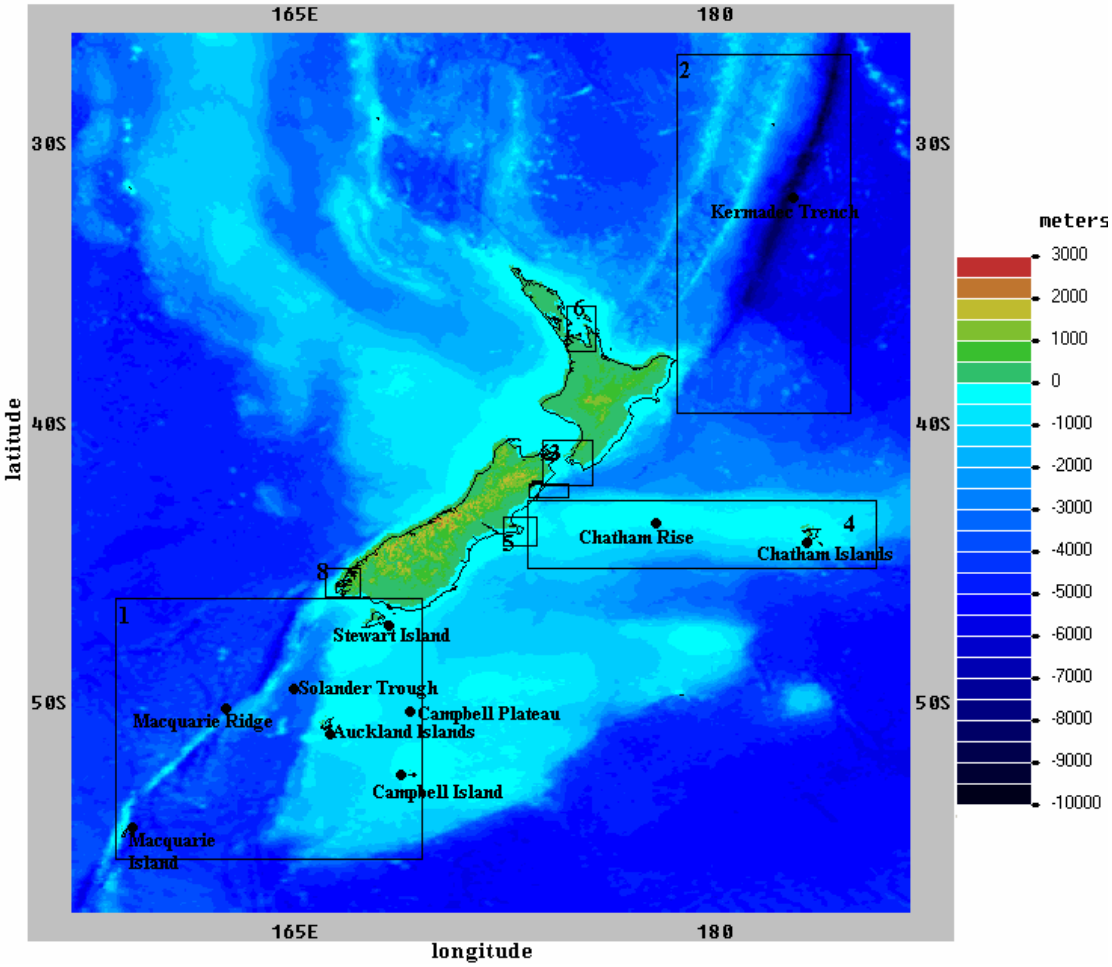

Figure 7.9: Bathymetry surrounding New Zealand. Bathymetric data are obtained from ETOPO2 (Smith and Sandwell, 1997) and are of 2 arc minute resolution. Depths are represented by negative values.

(1) South of New Zealand (contains the Macquarie Ridge, Campbell Plateau and the Solander Trough)
(2) Kermadec Trench
(3) Cook Strait
(4) The Chatham rise (extending from the Chatham Islands to the coastline)
(5) Bank's Peninsula
(6) Harauki Gulf
(7) Kaikoura Canyon
(8) The Fjords of Southland

7.3.1 Region (1) – South of New Zealand

In the region south of New Zealand, the Macquarie Ridge has the potential to produce a near field tsunami event from either a landslide or an earthquake (Berryman, 2006). This region's location (on the Rim of the 'Pacific Ring of Fire', refer to Figure 2.1) also makes it vulnerable to far field events that originate from areas such as the Chilean fault line, (situated off the west coast of South America).

Consideration is given to issues that specifically relate to the modelling of a dispersive 'deep water wave' or 'intermediate depth wave', that may originate (for example) from a near field landslide or submarine slump, and a non dispersive tsunami that may originate (for example) from a far-field seismic event.

The significance of the bathymetric variability in region (1) is illustrated in Figure 7.10. With the use of colour pairs Figure 7.10 highlights changes in depth which correspond to ε = 0.9 and ε = 1.1. When both colours of a pair are adjacent, the change in depth between them is representative of a feature with a parameter that corresponds to one of the four ε values.

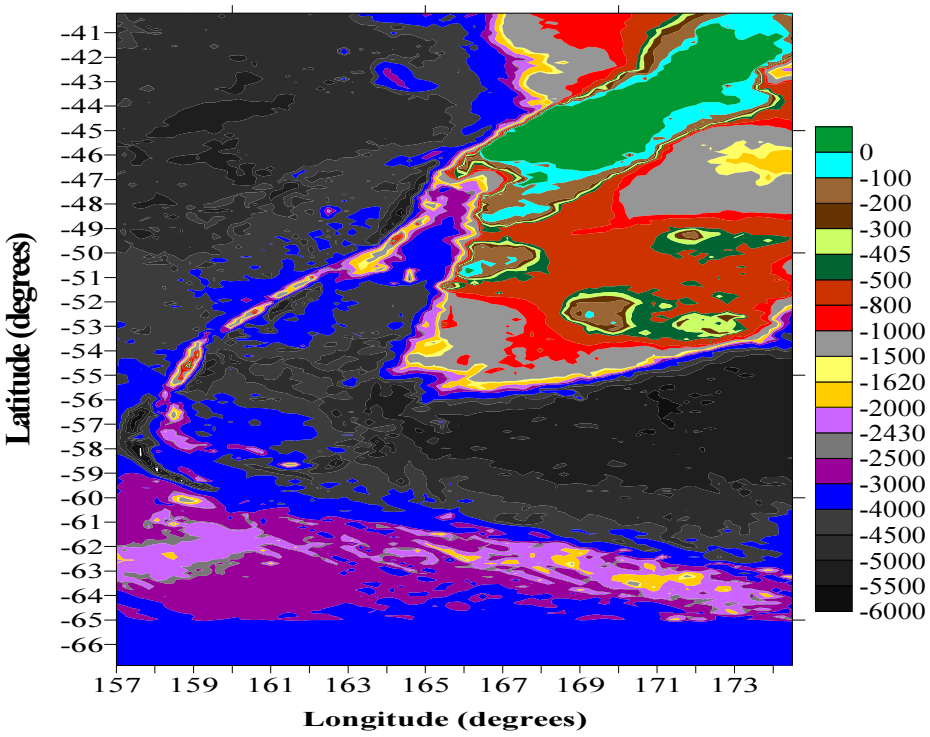

Figure 7.10: Paired colours represent bathymetric features south of New Zealand, where the ratio between each pair corresponds to $\varepsilon = 0.9$ or $\varepsilon = 1.1$. A colour pair is classified by two shades of the colour green, brown, red yellow, purple or black.

Non dispersive wave

A far field event that originates from the Chile Fault (as mentioned above) is one potential source of a non dispersive shallow water wave that may impact on region (1). Statistics of past events show that waves generated from activity along this fault line pose the largest tsunami threat to this Southern region of New Zealand (Berryman, 2006). Most of the far field tsunami events that have occurred in the Pacific basin (refer Figure 2.1) and impacted on New Zealand, have long periods and therefore the majority of their energy lies in the fundamental harmonic. For example, Fourier analysis (Gilmour, 1990) of relevant wave data for the 1960 Chile event recorded in Wellington harbour, showed the fundamental harmonic corresponded to a period of 160 minutes, and the second and third to 29.5 and 25.8 minutes respectively.

To estimate the influence bathymetric depth variations in region (1) have on the behaviour of a shallow water wave from any direction within this domain, the bathymetry is described by a Gaussian type continuous topography. This allows the concept of a width that causes maximum reflection (refer Mofjeld et al., 2003) to be introduced. This concept was used in Chapter's 4 and 5 to predict scatter from a dispersive wave. This width can by calculated using Equation 4.7 and that the full width half maximum (FWHM) of a Gaussian is given by σ*1.17, where σ is the standard deviation and where 3σ = 99.73 % = L (the distance between the bottom and top of a feature in Figure 7.11).

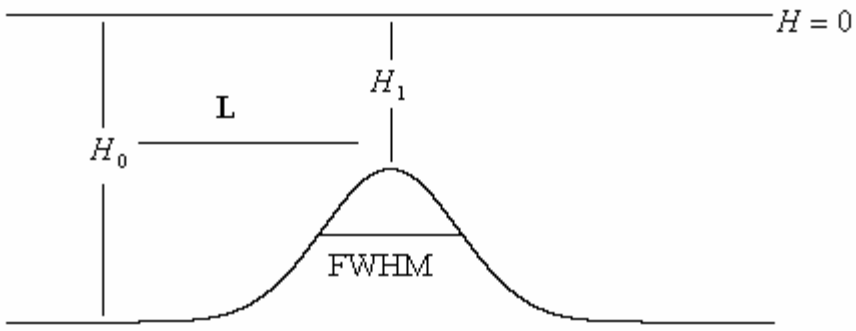

Figure 7.11: Diagram illustrating the distance L between the two depths H_0 and H_1 (that is controlled by the standard deviation, σ).

The width which will cause maximum reflection of a far field event from the East with a period 160 minutes (as above), is calculated to be approximately 265 km.

On observation of a bathymetric chart for this region (NZ 28, printed in January 1999, by Land Information New Zealand), distances (refer Figure 7.11) over which the change in depth occurs for ε = 0.9 or ε = 1.1 (Figure 7.10), are shorter than 265 km. It is therefore expected that the depth variations in this vicinity will cause the second or third harmonic of the far field wave event mentioned above, to scatter to a greater extent than that of the fundamental with a period of 160 minutes.

Most tsunami waves that propagate in this vicinity will approach the dominant features from an oblique angle. This is due to the direction from which the wave arrives, and also to guiding of shallow water tsunami waves by features such as the Solander Trench and the Macquarie Ridge. (A theoretical background on the scatter of oblique waves incident on a bathymetric feature is given in Mofjeld et al., 2003).

Preliminary simulations of a wave with a period of 8 minutes (chosen for illustration purposes only) propagating in region (1), showed significant effects from scattering, associated with the Macquarie Ridge, the Auckland Islands and the Campbell Plateau. These effects for incident angles of propagation; 120, 180 and 240 degrees, are illustrated in Figures 7.12, 7.13 and 7.14, where the scale is surface elevation given in metres. N.B. angles of incidence are measured from the reference point of zero degrees at the grids northern edge, and increase in the counter clockwise direction. Simulations utilized two wavelengths of sponge layers and had zero initial velocity profiles. Grid resolution is ~ 7 km.

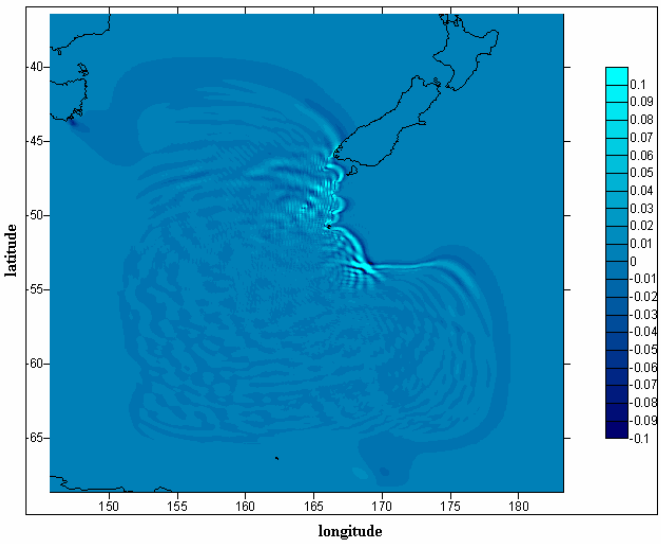

Figure 7.12: Observed scatter for a tsunami wave with a period of 8 minutes incident at an angle of 120°.

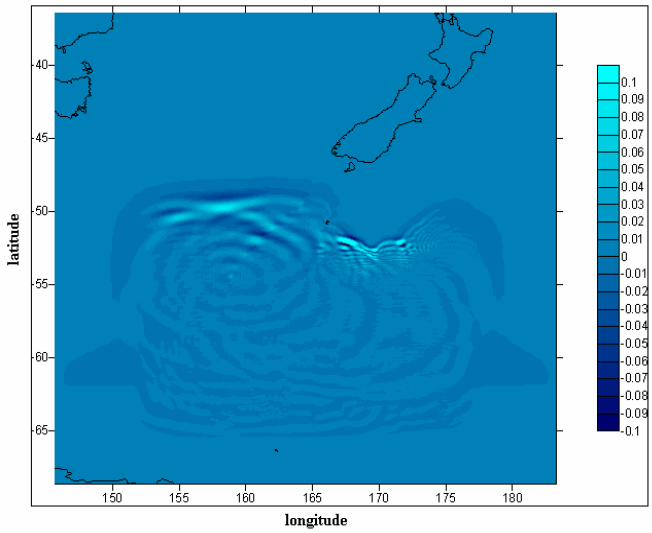

Figure 7.13: Observed scatter for a tsunami wave with a period of 8 minutes incident at an angle of $180°$.

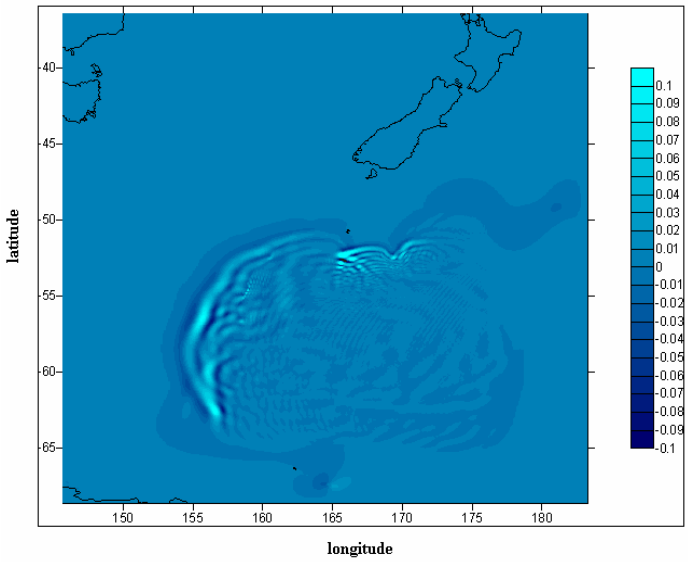

Figure 7.14: Observed scatter for a tsunami wave with a period of 8 minutes incident at an angle of $240°$.

There are several reasons which support the application of a nonlinear shallow water model as opposed to a more computationally demanding Boussinesq model (refer section 7.1) to simulate propagation of a non dispersive long period wave in region (1). These reasons are:

- When a typical far field tsunami amplitude is assumed (less than 0.5 m, Hammack 1972), the shoaling that a shallow water tsunami wave within this region could

undergo, is expected to be partially describable by nonlinear processes and therefore a nonlinear model is recommended.

- A finer grid resolution is more easily achieved by use of a nonlinear model as opposed to a Boussinesq model.
- Results in Chapter 5 (for dispersive wave propagation across a combination of two features) show a nonlinear dependence on wave transmission across two features separated by distance of less than 1.5 wavelengths. It is therefore presumed that this dependence will be even greater for a shallow water wave. As a result a nonlinear model will provide more accurate results than a linear model.
- GWB and GWS predictions for propagation of a shallow water wave (section 7.2) show there is no advantage in the use of a more computationally demanding model under these conditions.

Three areas where a fine grid resolution is required for the modelling of a 'shallow water tsunami wave' in the region South of New Zealand include areas where: depth variations are considerable (Campbell Plateau, Solander Trough, Macquarie Ridge), the ocean which surrounds islands or other equivalent small areas of land (e.g. the Auckland Islands and Stewart Island, Macquarie Island), and; along coastlines where wave amplitudes increase in response to depth decreases. From Figures 7.12 to 7.14 the areas that would require higher resolution computational grids are Stewart Island, the southern coast of the South Island, and the regions where the Fiords meet the coast.

The need for finer grid resolution in these areas is to adequately resolve wave amplification in an attempt to accurately assess the impact of tsunami on the coastal environment. If data is available, predictions from numerical simulations could be validated against past tsunami geological evidence in the vicinity on the Southern coast of the South Island (James Goff, personal communication).

Depending on the wavelength of the shallow water tsunami wave, use of a model with time dependent boundary conditions is recommended.

Due to the great distances propagated by tsunamis generated by a far field event, the inclusion of the Coriolis force can significantly alter the direction of wave propagation (Kowalik and Whitmore, 1991). The surface elevation from a simulation that included the Coriolis force is shown in Figure 2.3. The inclusion of the Coriolis force is expected to influence the proportion of energy in a far field event originating for example, from Chilean Fault line, as it sweeps around southern latitudes. This would have the result that a shallow water wave from this region will be directed up towards the Chatham Rise (Power et al., 2006), minimising the wave energy that would otherwise reach the North Island. If the Coriolis force is excluded, the wave will propagate in a direction that is more or less perpendicular to its origin (as in the idealised experiment presented in section 7.1).

If run up is to be included, i.e. if mapping of coastal hazard is desired, then a very fine resolution is required, and nested grids or an adaptive gridding technique should be employed.

Dispersive wave

In region (1) a near field source with the potential to generate a dispersive tsunami wave is (for example) a landslide from the Macquarie Ridge.

Because of the dispersive nature of this type of wave, the numerical grid resolution is required to be fine enough to resolve both the initial waveform and the range of wave components that result. A major disadvantage of higher resolution grids is that grids discretized into a uniform cell size can be very dense. In addition, the large number of numerical terms associated with the fourth order Boussinesq equations in numerical models (e.g. Geowave) can give rise to high numbers of numerical error terms. These often cause numerical simulations to become unstable.

To illustrate the numerical and physical issues associated with modelling a dispersive wave in region (1) preliminary calculations for the application of a numerical model were carried out. A wavelength of 4500 m (as in Chapter 6) was assumed. On the condition that the feature depth to wavelength ratio is comparable to that in Chapter 6, then on reference to Figure 7.11, and with use of the method above (refer non dispersive wave), maximum scatter for a dispersive wave is predicted to occur for feature widths (or depth changes) that are in the order of several kilometres.

To remain consistent in the resolution used in Chapters 4, 5 and 6 the wave should be resolved by 10 nodes. Therefore, because in this example the numerical grid is uniform, the grid encompasses only the features of interest (Figure 7.15) in order that the number of grid nodes at which the equations will be solved is reduced. Its dimensions are 157.00 and 167.96 degrees longitude and between -55.95 and -44.37 degrees latitude. The grid was discretized into 1749 cells with sizes *dx, dy* of 446.7 m and 736.9 m respectively. To ensure a stable simulation, all sides of the domain should be surrounded by two wavelengths of sponge layers. To prevent dissipation of the incident wave within these layers, propagation should begin at a distance at least 3 wavelengths in from the side from which propagation initiates.

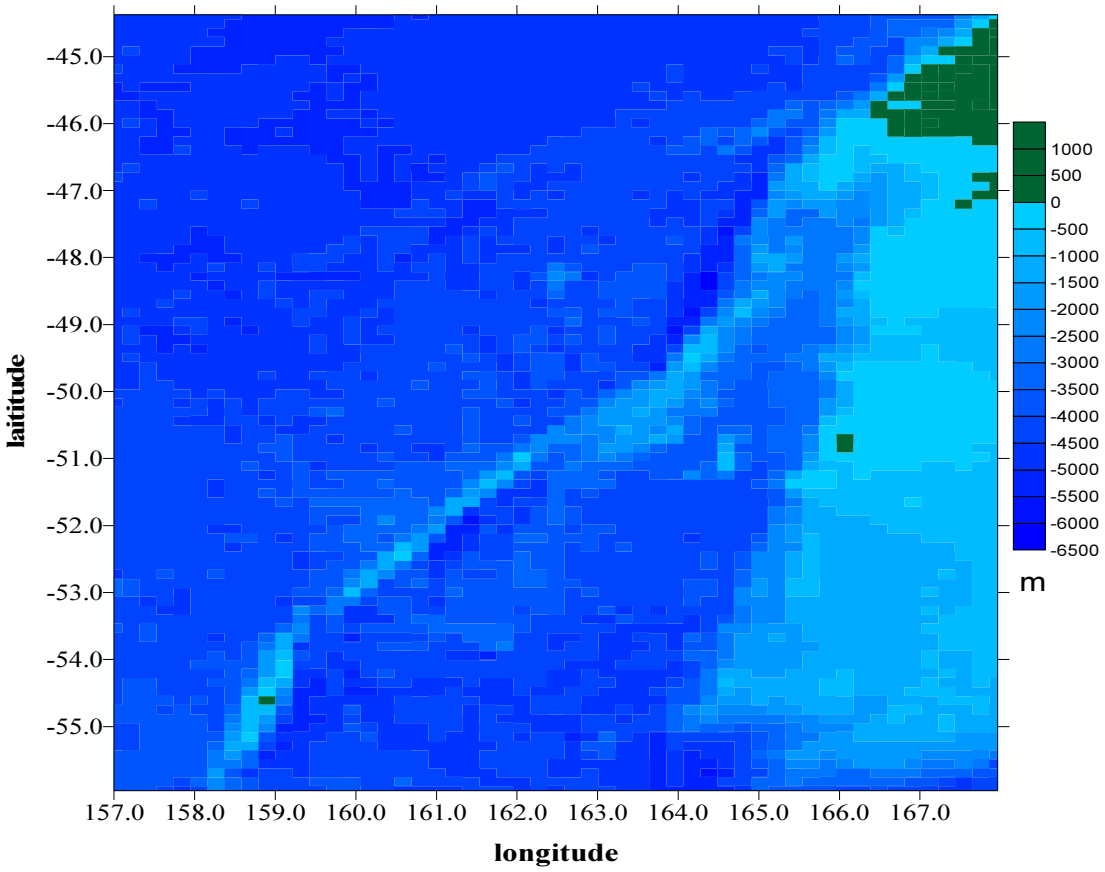

Figure 7.15: Proposed grid for use in simulation of a dispersive wave in the region south of New Zealand. The grid has a resolution *dx, dy* of 447 m and 737 m respectively. Where the colour bar represents depth in metres and depths greater than zero are land.

A non hydrostatic approach is important in this case, as it is able to predict the propagation of dispersive waves over variable bathymetry (refer to Chapter's 4 and 5). However, it is probable that simulations with a fine grid resolution will cause a Boussinesq model to become unstable for the reasons noted above. The optimum solution to this problem would be to employ nested grids. These grids should be placed across features of interest (e.g. the Macquarie Ridge, Campbell Plateau, Solander Trough) that are separated by more than 1.5 times the assumed wavelength. It is important to note that for oblique incidence, this separation distance at which the wave's nonlinear dependence on the second feature becomes less significant (refer Chapter 5) may differ. The extent of dispersion that has occurred for a particular wave after it has been scattered from a feature dictates whether or

not the components can be reincorporated back into the coarser resolution grid. If the dispersed components cannot be resolved, it may be that they are insignificant and will therefore quickly dissipate without having a significant negative impact to a nearby coastline. As grid resolution is important when modelling a dispersive tsunami wave, use of a model with time dependent boundary conditions (which results in the need for a smaller numerical domain) is recommended. This is of particular significance when the numerical grid is uniform.

7.3.2 Region (2) – Kermadec Trench

The Kermadec trench contains the deepest water within the New Zealand Economic Zone. The Kermadec Trench and the Hikurangi Plateau can be seen in Figure 7.16.

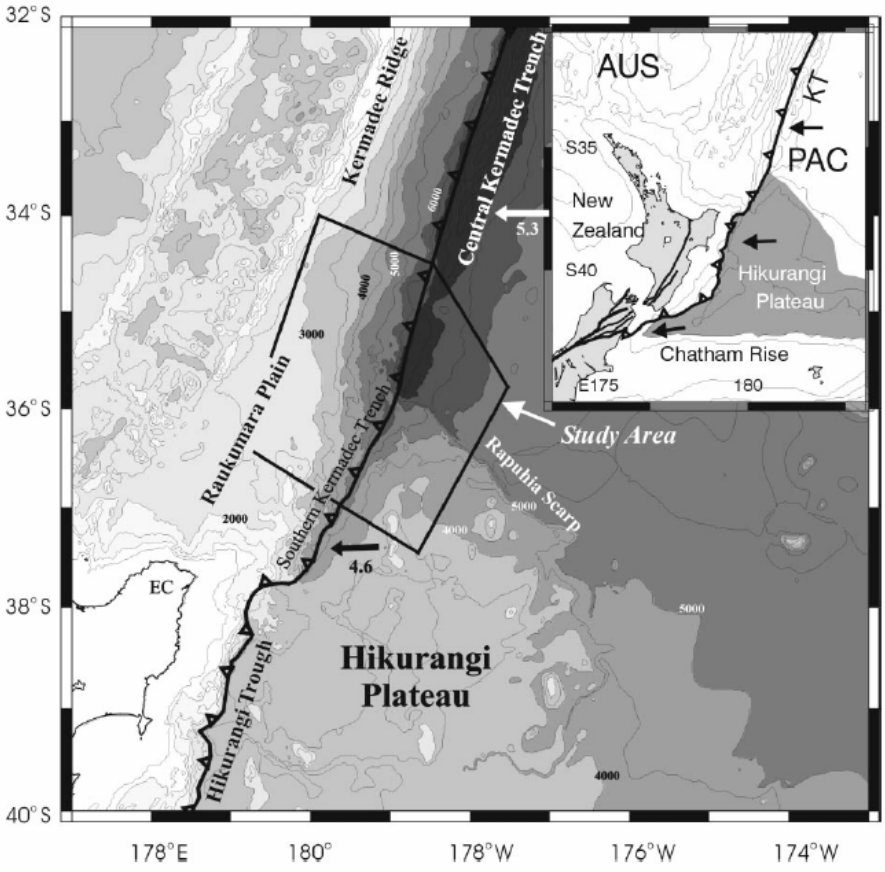

Figure 7.16: Bathymetry of the Hikurangi Plateau/Central-Southern Kermadec Trench. Open arrows show Pacific–Australia plate convergence direction from de Mets et al. (1994). The large inset is a simplified

bathymetric map that shows the extent of the Hikurangi Plateau the Kermadec Trench (KT) is the deformation front between the Pacific (PAC) and Australia (AUS) plates. EC: East Cape; SKT: Southern Kermadec Trench. (Figure and figure caption taken from Davy and Collot, 2000).

An example of a potential near field source within region (2) would be a landslide generated from the Rapuhia Scarp (Davy and Collot, 2000) (Figure 7.16). This region is also susceptible to far field events that originate from areas such as off the west coast of South America (The Chilean Fault) or from the northern region of the Pacific Basin (the Aleutian Mega Thrust fault).

A closer image of the features within Figure 7.16 can be seen in Figures 7.17 and Figures 7.18. Figure 7.17 illustrates the interesting angles at which the features intercept. Figure 7.18 shows that the horizontal scale of these features is similar to those found in Chapters 4 and 5. Reference to Figure 7.16 and Davey and Collot (2000) indicate that the depth of these features is between 5000 and 6000 m.

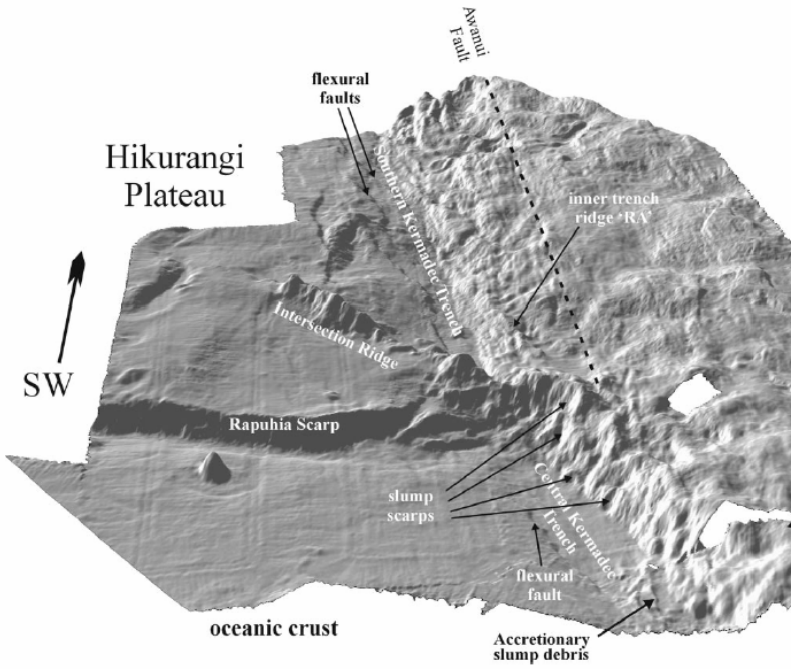

Figure 7.17: Shaded perspective diagram of the Central-Southern Kermadec Trench looking southwest; illumination is from the southeast; vertical exaggeration is 3:1. (Figure and figure caption taken from directly from Davy and Collot, 2000).

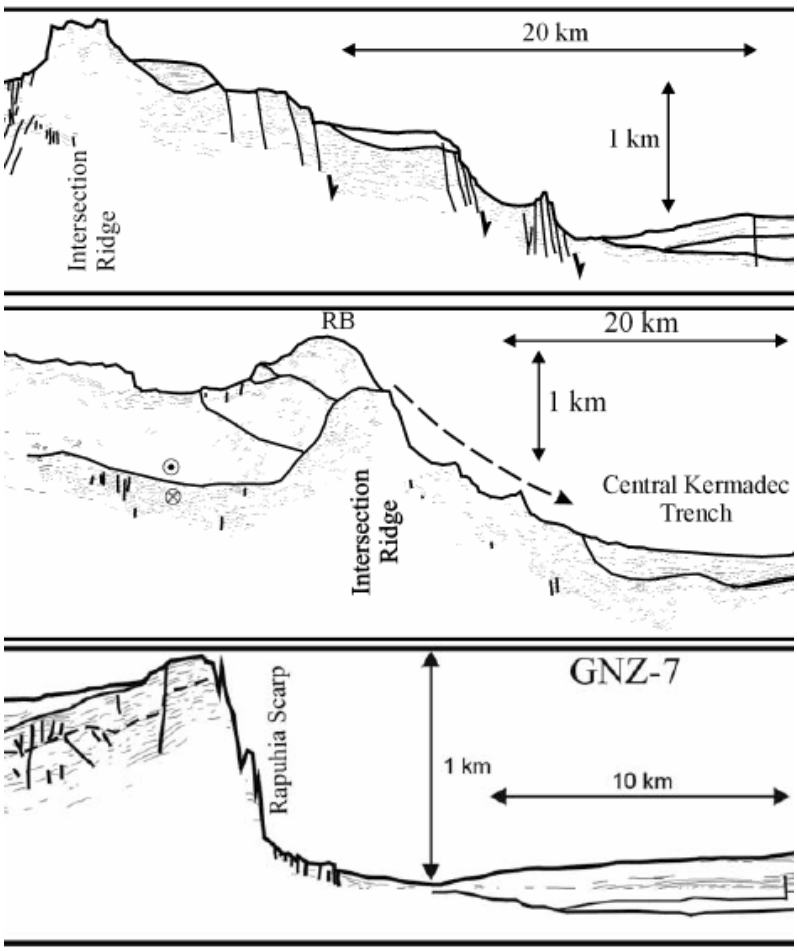

Figure 7.18: This figure provides an indication of the scale of the bathymetric features that are presented in Figure 7.17. (These images are extracted from two more comprehensive images in Davey and Collot, 2000).

Non dispersive wave

It is anticipated that features such as the Kermadec trench and the Hikurangi Trough would act as wave guides and thus influence the propagation direction of a shallow water (non dispersive) tsunami wave. For example, a shallow water wave event that is generated at the Aleutian Islands would be guided in towards the coastline reaching areas such as Gisborne.

To simulate propagation of a non dispersive tsunami wave within region (2) the same numerical treatment as for the non dispersive event in section 7.3.1 is recommended. Nested grids should be used over bathymetric areas of interest. Their purpose would be to ensure that the changes in wave amplitude caused by a particular bathymetric feature or

depth change can be resolved and incorporated into the solution of the wave's amplitude after it has passed the particular area of interest.

Nested grids should be used to resolve large scale ridge or trench features (i.e. those with a width of approximately one quarter the shallow water wavelength of interest, refer Mofjeld et al., 2003), for example the Kermadec Trench and Hikurangi Trough. In addition, it is advised that a nested grid be used to resolve the area that encompasses the combination of features shown in Figure 7.17 (Rahupia Scarp, Kermadec Trench and Intersection Ridge). The purpose of this would be to capture resonant effects from the separation angles between the features. Referring to Chapter 5, it has been observed that resonances for a separation distance between features of less than 1.5 wavelengths have given rise to nonlinear contributions for a dispersive wave that propagates across a combination of two features. For values of the separation distance less than 1.5 wavelengths, variations in the linear predictions were also observed, which suggests that the nonlinear interactions are not exclusively related to the waveform undergoing dispersion. Therefore it is anticipated that use of a nested grid in the aforementioned region is necessary. This is despite the variations between the theoretical normal incidence results in Chapter 5 and the more realistic real world scenario of oblique angles of incidence.

Dispersive wave

Referring to Figures 7.18, 7.16 and the work of Davey and Collot (2000) for the discussion that follows it is assumed that the height of the Rahupia Scarp is approximately 1 km (Figure 7.18), and that the change in depth between the ocean floor and this height occurs over a distance of the order $k_0\sigma = 0.707$, (refer Chapter 4), where k_0 is the wave number and the wavelength satisfies the ratio between feature depth and the dispersive wavelength in Chapters 4, 5 and 6. The application of these assumptions makes it apparent that the

dimensions of the Rahupia Scarp are very similar to those in Chapter's 4, 5 and 6. It is therefore anticipated that a wave with a wavelength of ~6000 m that propagates across this feature will undergo scatter and increased dispersion. The change in depth between the ocean floor and the maximum height of Intersection Ridge occurs over a distance that is far greater than that for the Rahupia Scarp. The expected result is that a wave with the assumed characteristics will not be scattered as it propagates over this Scarp but could undergo increased dispersion.

It is proposed that the oblique angle at which the features in Figure 7.17 intercept will provide further results of interest. Although Chapter 5 presents no work on wave incidence at an oblique angle, the theoretical studies of Chapter 5 conducted for normal incidence, can be used to provide an indication of the types of the behaviour which would be expected for this wave. If the feature depth to wavelength scale is of the order of that discussed in Chapter's 4, 5 and 6 then the separation distances between the features (Figure 7.17) is observed to be larger than a distance 1.5 times this wavelength and the development of nonlinear interactions with these features is deemed insignificant. This is with the exception of the region closer to the point of interception of the three features (where it is suggested that a nested grid be used). However, if the assumed wave is in the range of an intermediate depth wave, (defined in Table 2.4) and closer to the regime of a shallow water wave, the statement with regards to the distance separating the features in Figure 7.17 would not necessarily apply.

To simulate propagation of a dispersive tsunami wave within region (2), the same recommendations are made as for the dispersive event in section 7.3.1. For the various reasons discussed in section 7.3.1, the use of nested grids for modelling a dispersive wave event is advantageous. When modelling this wave in region (2) it is recommended that nested grids be used to resolve the Intersection Ridge and the region in which it meets with the Rahupia Scarp and the Southern Kermadec Trench.

7.3.3 Summary

The physical and numerical issues associated with the application of a numerical model for use in tsunami studies were discussed in detail for regions to the south and north of New Zealand. For both regions it was concluded that to model a shallow water tsunami wave a nonlinear model be used and that to model a dispersive tsunami wave, a Boussinesq model be used. Both models require time dependent boundary conditions and the employment of nested grids or an adaptive gridding technique.

The discussion within section 7.3 has highlighted the necessity for use of a model that includes some type of variable gridding approach for modelling regions of complicated bathymetry. This was shown to be an important prerequisite for the application of both a nonlinear and a Boussinesq model as the ability to resolve wave amplification is of key importance when attempting to quantify the impact of tsunami on the coastal environment.

7.4 Chapter summary

The investigations presented in the first three sections of this Chapter have provided an overall indication of the extent to which Geowave is robust in its application to the geophysical environment.

A comparison of GWS and GWB in Section 7.1 highlighted significant contributions from the fully nonlinear extended Boussinesq terms in Geowave in modelling the propagation of a dispersive tsunami wave.

In section 7.2 it was successfully demonstrated that the equations of Geowave (as available on the public domain) were also capable of predicting the evolution of a non dispersive tsunami wave. This section established that the coarse grid resolution in the application to a far field event or large scale domain makes the computationally demanding Boussinesq model Geowave an unsuitable choice of model for predicting coastal wave

amplification. In this type of application a faster shallow water model is a better choice. However, results did demonstrate that Geowave can assist in predicting regions of resonance which could be used for future finer scale studies.

Section 7.3 discussed the factors which relate to the application of a numerical model to a geophysical tsunami problem. This discussion emphasized the requirement for the use of nested grids in application of either a nonlinear or a Boussinesq model, to regions of complicated bathymetry.

Chapter 8

Conclusions

Chapter 8 collates the key findings of this thesis into a research summary, which illustrates the fulfilment of its initial aims. In addition, proposals for further development of the numerical model Geowave V1.0 will be made.

8.1 Research summary

The aim of this thesis was to assess differences between results predicted by a fully nonlinear extended Boussinesq model (with its ability to predict dispersion) and a non dispersive, linear or weakly nonlinear model in their application to modelling dispersive and non dispersive tsunami waves over varying bathymetries, and to determine the usefulness and robustness of the geophysical application of the more computationally demanding Boussinesq model.

The tool chosen for use in this research is the fully nonlinear extended Boussinesq model Geowave V1.0 (GW). To assist in this study, the linear (GWL) and weakly nonlinear shallow water equations (GWS) were then implemented into GW. Note that the fully nonlinear extended Boussinesq set of GW is referred to as GWB.

The work presented in this thesis was conducted in two parts. The first part used numerical simulations to highlight contributions from nonlinear and dispersive terms to the scatter of a hypothetical tsunami (with dispersive properties), from single and combined idealized bathymetric features. Results using continuous and discontinuous single idealized bathymetric features are presented in Chapter 4. Results using a combination of two

continuous features are presented in Chapter 5. Chapter 6 links the theoretical work conducted in Chapters 4 and 5 to the geophysical world.

The second part of this work is presented in Chapter 7. It used numerical simulations to determine the usefulness and robustness of Geowave V1.0 in its application to tsunami propagation over a variety of geophysical bathymetric domains. In addition it discussed the issues which relate to the application of a numerical model to a geophysical tsunami problem.

The results from Chapter 4 show small changes in depth for a continuous feature can cause transmitted wave amplitudes predicted by the fully nonlinear extended Boussinesq equations of Geowave (GWB) to be significantly smaller (by up to a factor of 2.4) than those predicted by the weakly nonlinear shallow water equations of Geowave (GWS).

They also indicate that differences between GWB and GWS contributions, to reflected and transmitted wave amplitudes, depend more on both the type (i.e ridge or escarpment) and form (i.e. continuous or discontinuous) of a feature and not whether its width will cause the strongest reflection. Results given in Chapter 5 demonstrate that the reflected amplitude of a wave incident at a combination of two bathymetric features is dependent on a second feature located within a distance of 1.5λ. Contributions from the nonlinear dispersive terms depend most strongly on the distance separating the two features and are of particular significance when the features are separated by 0.5λ. The investigation in Chapter 6 showed that GWB predicts a transmitted wave amplitude c. 22% smaller than that of GWS. This shows that there is a significant difference when a more computationally demanding extended Boussinesq model is applied to a geophysical tsunami scenario, where the wave has dispersive properties and the bathymetric domain contains gentle sloping features described by a depth variation of $\varepsilon = 0.9$ or $\varepsilon = 1.1$.

Results from real world studies presented in Chapter 7 highlighted the importance of nonlinear and dispersive terms in propagating a dispersive tsunami wave, analogous to those produced from a landslide, over a varying bathymetry. It also ascertained that the numerical model Geowave V1.0 (as available on the public domain) was robust in predicting evolution of both a dispersive and non dispersive tsunami wave but that it is inadequate for application to a large scale domain (where either horizontal dimension is tens of degrees), due to its reduced ability in predicting coastal wave amplification. The final section highlighted the requirement for the use of nested and unstructured grids in application of either a nonlinear shallow water or a non hydrostatic model, to regions where there exists a complex bathymetry.

8.2 Proposals for future work

Following the use of the numerical model Geowave V1.0 for the research conducted throughout this thesis, several ideas for its modification are proposed. As Geowave has the advantage of fully nonlinear extended Boussinesq equations, the proposed modifications to its code and numerical scheme could see its justified application to a wider range of bathymetric domains.

The first of these proposed modifications would be to change the method in which the numerical scheme discretizes the numerical domain to allow for a variable grid resolution. This could for example integrate the adaptive mesh refinement technique (Grauer et al., 1998). This modification would increase its success in application to a larger domain by providing the possibility to use both a finer resolution in coastal regions, (where wave amplification can be significant) and a coarser resolution grid in the deeper water where wave amplification is minimal. A second modification would involve reimplementation of a sponge layer boundary filter based on a wave penetration distance. Such a mechanism, although commented out, appears to have been integrated in

FUNWAVE V1.2. This filter would benefit Geowave by damping the surface elevation and horizontal velocities more efficiently and over a shorter numerical space, than that now required to minimize boundary reflections. It would also help remove the present necessity of an increased domain size (for the purpose of including additional nodes for a damping layer). A third modification which would benefit Geowave is the implementation of time dependent boundary conditions. The significance of this is that Geowave V1.0 could be used more efficiently, not only in its application to scenarios in which a tsunami event occurs internal to the domain, but also to those in which they are external and incoming to a domain.

Appendix A

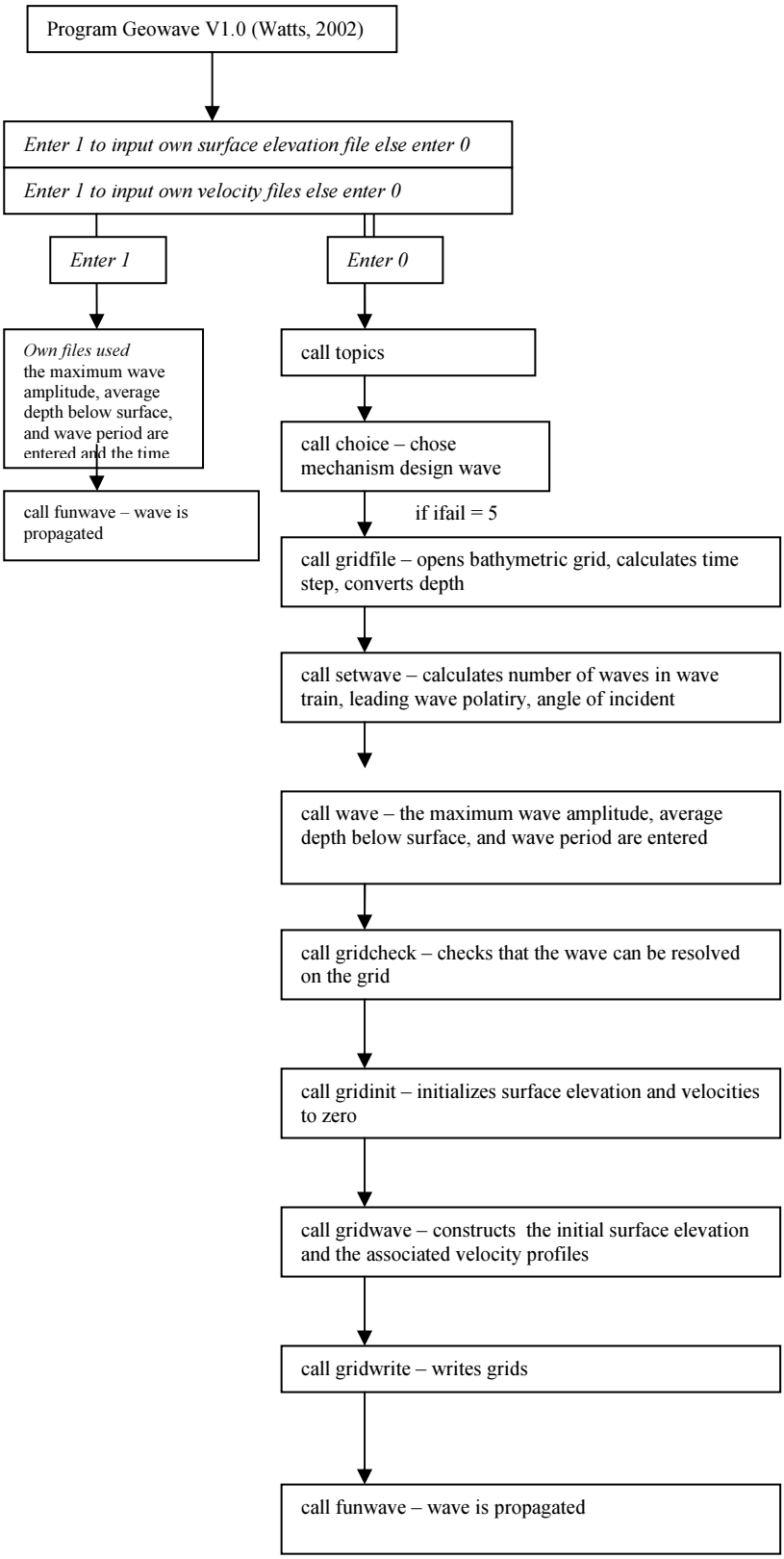

Figure B1: This flowchart depicts the initial subroutines called to produce an initial surface and associated velocity files using the setwave (design wave) subroutine. Italics indicate modifications, made for the purpose of this thesis, which allow the user to input initial files and bypass TOPICS.

References

Abe, K., Estimate of tsunami Run-up Heights from Earthquake Magnitudes, In: Tsuchiya, Y. and N. Shuto, (eds.), Tsunami: Progress in Prediction, Disaster Prevention Warning. Netherlands, Kluwer Academic Publishers, pp. 21-35, 1995.

Annunziato, A., and C. Best, The Tsunami Event Analysis and Models, Institute for the Protection and Security of the Citizen Joint Research Centre European Commission, January, 2005.

Barnett, A. G., Modelling tsunami waves along the New Zealand coast, Proceedings of the natural hazards management workshop, Wellington, 8-9 November, 1994.

Barnett, A. G., S. Beanland, and R. G. Taylor, Tsunami and Sieche Computation for Wellington Harbour, Proceedings of the Pacific Conference on earthquake engineering 1991, New Zealand National Society of Earthquake Engineers, 2, pp. 91-102, 1991.

Bearman, G., (Ed). Waves, tides and shallow water processes. Pergamon Press, Oxford, 1991.

Beji, S., and J. A. Battjes, Experimental investigation of wave propagation over a bar, *Coastal Engineering*, 19(1-2), 151-162, 1993.

Benjamin, T. B., and J. E. Feir, *J. Fluid Mech.* 27, 417-430, 1967.

Berryman, K, Review of Tsunami Hazard and Risk in New Zealand, Institute of Geological & Nuclear Sciences client report 2005/104, January 2006.

Black, K. P., The numerical model 3DD and support software. 19, Department of Earth Sciences, The University of Waikato, Hamilton, 1995.

Borrero, J. C., J. F. Dolan, and C. E. Synolakis, Tsunamis within the eastern Santa Barbara Channel, Geophysical Research Letters, 28(4), pp. 643-646, 2001.

Briggs, M. J., C. E. Synolakis, G. S. Harkins, and D. R. Green, Laboratory experiments of tsunami runup on a Circular Island, *PAGEOPH,* 144(3-4), 1995.

Chen, Q., J. T. Kirby, R. A. Darlrymple, A. B. Kennedy and A. Chawla, Boussinesq modelling of wave transformation, breaking, and run up. Part 2: 2D, *J. Wtrwy, Port, Coast, and Oc. Engrg.,* ASCE, 126(1), 48-56, 2000.

Chick, L. M. Potential Tsunami Hazard associated with the Kerepehi fault Hauraki Gulf, New Zealand. Unpublished M.Sc. Thesis, University of Waikato, 284 p, 1999.

Chick, L. M., W.P de Lange, and T.R. Healy, Potential tsunami hazard associated with the Kerepehi Fault, Firth of Thames, *New Zealand Natural Hazards,* 24(3), 309-318, 2001.

Chick, L., and W. P. de Lange, R. Fraser, Tsunami hazard and inundation modelling for the Firth of Thames, *TEPHRA*, 17, 51-55, 1999.

Choi, B. H., E. Pelinovsky, I. Ryabov, and S. J. Hong, Distribution functions of tsunami wave heights*, Natural Hazards*, 25(1), 1-21, 2002.

Choi, B. H., S. J. Hong, and E. Pelinovsky, Simulation of prognostic tsunamis on the Korean coast*, Geophysical Research Letters*, 28(10), 2013-2016, 2001.

Dahlquist, G, Å Björck, Numerical Methods, Courier Dover Publications, 2003.

Davy, B. and J. Y. Collot, The Rapuhia Scarp (northern Hikurangi Plateau) — its nature and subduction effects on the Kermadec Trench, *Tectonophysics*, 328, 269–295, 2000.

de Lange, W. P., and A. G., Hull, Tsunami hazard for the Auckland Region. Auckland regional council Environment Division, November 1994.

de Lange, W. P., and T. R. Healy, New-Zealand Tsunamis 1840-1982 New Zealand, *Journal of Geology and Geophysics*, 29(1), 115-134, 1986.

de Lange, W. P., and T. R. Healy, Tsunami Hazards in the Bay of Plenty, New Zealand: An Example of Hazard Analysis Using Numerical Models, *Journal of Shoreline Management,* 2, 177-197, 1986.

de Lange, W. P., T. R. Healy, Tsunami hazard for the Auckland region and Hauraki Gulf, New Zealand, *Natural Hazards*, 24(3), 267-284, 2001.

de Lange, W. P., Tsunami Hazard: An investigation into the potential tsunami hazards of the Bay of Plenty Region using numerical models. M.S.c thesis, University of Waikato, Hamilton, 1983.

de Lange, W., and R., Fraser, Overview of tsunami hazard in New Zealand. *TEPHRA*, 3-9, October, 1999.

Dalrymple, R. A., and R. G., Dean, Water wave mechanics for scientists and engineers, World Scientific, 1991.

Garg, V. K., Applied Computational Fluid Dynamics, ed., Inc, New York, Marcel Dekker, 1998.

Geist, E. L., S. L. Bilek, A. Diego and V. V. Titov, Differences in tsunami generation between the December 26, 2004 and March 28, 2005 Sumatra earthquakes, *Earth Planets Space*, 58, 185–193, 2006.

Gilmour, A. and B. Stanton, Tsunami hazards in the Wellington region (part 4 of 1989 study). Report prepared for Wellington Regional Council, March 1990.

Gisler, G., Sage calculations of the tsunami threat from La Palma, Proceedings of the 22nd International Tsunami Symposium, Crete, 27-29 June, 65-72, 2005.

Gonzalez, F. I., K. Satake, E. F. Boss and H. O. Mofjeld, Edge Wave and Non-Trapped Modes of the 25 April 1992 Cape-Mendocino Tsunami, Pure and Applied Geophysics, 144(3-4), 409-426, 1995.

Grauer, R., C. Marliani and K. Germaschewski, Adaptive Mesh Refinement for Singular Solutions of the Incompressible Euler Equations, *Phys. Rev. Lett*., 80, 4177-4180, 1998.

Guibourg, S., P. Heinrich, and R. Roche, Numerical modelling of the 1995 Chilean tsunami. Impact on French Polynesia, *Geophysical Research Letters*, 24(7), 775-778, 1997.

Hammack, J. L., Tsunamis – a model of their generation and propagation. Division of engineering and applied science, California Institute of Technology, Pasadena, California, June 1972.

Heinrich, P., A. Piatanesi, E. A. Okal, and H. Herbert, Near field modelling of the July 17, 1998 tsunami in Papua New Guinea, *Geophysical Research Letters*, 27(19), 3037-3040, 2000.

Herbert, H., P. Heinrich, F. Schindele, and A. Piatanesi, Far-field simulation of tsunami propagation in the Pacific Ocean: impact on the Marquesas Islands (French Polynesia), *Journal of Geophysical Research,* 106(C5), 9161-9177, 2001.

Horrillo, J. J., Z. Kowalik and W. Knight, Full Navier Stokes Approximation in Tsunami Investigation, Proceedings of the 22nd International Tsunami Symposium, 77-88, 2005.

Imamura, F., Numerical method of tsunami simulation with the leap-frog scheme, Part 2. Propagation in the ocean in the spherical coordinates, Disaster Control Centre, Faculty of Engineering, Tohoku University, Sendai 1995.

Imamura, F., Review of Tsunami Simulation with a Finite Difference Method, In Long-Wave Runup Models (eds., Yeh, H., Liu, P., and Synolakis, C.), World Scientific, River Edge, pp.43-87, 2004.

Imteaz, M., and F. A., Imamura, A non-linear model for stratified tsunami waves and its application, *Science of Tsunami Hazards,* 19, 150-159, 2001.

Kennedy, A. B., Q. Chen, J. T. Kirby and R. A. Darlrymple, Boussinesq modelling of wave transformation, breaking, and run up. Part 1: 1D, *J. Wtrwy, Port, Coast, and Oc. Engrg.,* ASCE, 126(1), 39-47, 2000.

Khramushin, V. N., and G. V. Shevchenko, A method of detailed tsunami zoning for coastal Aniva Bay, *Oceanology*, 34(2), 192-197, 1994.

Kirby, J. T. and R. A., Dalrymple, Combined refraction/diffraction model REF/DIF 1, User's Manual", Coastal and Offshore Engineering and Research, Inc., Newark, DE., January, 1985. (Revised June, 1986)

Kirby, J. T., G., Wei, Q., Chen, A. B., Kennedy, and R. A., Dalrymple, FUNWAVE 1.0. Fully Nonlinear Boussinesq Wave Model Documentation and User's Manual. Centre for Applied Coastal Research, University of Delaware, Newark. September, 1998.

Koshimura, S., F. Imamura, and N. Shuto, Characteristics of Tsunamis Propagating over Oceanic Ridges: Numerical Simulation of the 1996 Irian Jaya Earthquake Tsunami, *Natural Hazards,* 24(3), 213-229, 2001.

Koshimura, S., F. Imamura, and N. Shuto, Propagation of obliquely incident tsunamis on a slope Part II: characteristics of on-ridge tsunamis, *Coast. Eng. J.*, 41(2), 165–182, 1999.

Kowalik, Z., and P. Whitmore, An investigation of two tsunamis recorded at Adak, Alaska, *Science of Tsunami Hazards*, 9(2), 67-83, 1991.

Kowalik, Z., W. Knight, T. Logan, and P. Whitmore, Numerical Modelling of the Global Tsunami: Indonesian Tsunami of 26 December 2004, *Science of Tsunami Hazards*, 23(1), 40-56, 2005.

Liu, P. L. F., C. E. Synolakis, and H. Yeh, A report on the international workshop on long wave run up", *J. Fluid Mech.*, 229, 678-88, 1991.

Lynett, P. J., and P. L. F. Liu, A two-dimensional, depth-integrated model for internal wave propagation over variable bathymetry, *Wave Motion*, 36, 221-240, 2002.

Lynett, P. J., J. C. Borrero, P. L. F., Liu and C. E Synolakis, Field survey and numerical simulations: A review of the 1998 Papua New Guinea Tsunami, *Pure appl. Geophys.,* 160, 2119-2146, 2003.

Matsuyama, M., J. P. Walsh, and H. Yeh, The effect of bathymetry on tsunami characteristics at Sissano Lagoon, Papua New Guinea, *Geophysical Research Letters*, 26(23), pp. 3513-3516, 1999.

Melville, W K., Instability and Breaking of Deep-Water Waves, *Journal of Fluid Mechanics,* 115, 165-185, 1982.

Mofjeld, H. O., V. V. Titov, F. I. González, and J. C.Newman, Analytic theory of tsunami wave scattering in the open ocean with application to the North Pacific Ocean. NOAA Tech. Memo. OAR PMEL-116 (NTIS PB2002-101562), 38 pp, 2000.

Mofjeld, H.O., V.V. Titov, F.I. Gonzalez, and J.C. Newman, Analytic theory of tsunami wave scattering in the Open Ocean with Application to the North Pacific, NOAA Technical Memorandum OAR PMEL-116, 38 pp, January 2000.

Nakamura, M., Source fault model of the 1771 Yaeyama tsunami, southern Ryukyu Islands, Japan, inferred from numerical simulation, *Pure and Applied Geophysics*, 163(1), 41-54, 2006.

Narayan, J. P., M. L. Sharma, and B. K. Maheshwari, Run-up and inundation pattern developed during the Indian Ocean Tsunami of December 26, 2004 along the coast of Tamilnadu (India), *Gondwana Research*, 8(4), 611-616, 2005.

Onorato, M., A. R. Osborne, M. S. and S. Bertone, Freak Waves in Random Oceanic Sea States, (May 22, 2006) published at www.arXiv.org

Pararas-Carayannis, Presented at the tsunami symposium from May 25-27, Honolulu, 1999.

Pelinovsky, E., C. Kharif, I. Riabov, and M. Francius, Modelling of tsunami propagation in the vicinity of the French coast of the Mediterranean, *Natural Hazards*, 25(2), 135-159, 2002.

Power, W., G. Downes and M. Stirling, Estimation of tsunami hazard in New Zealand due to South American earthquakes, *Pure and Applied Geophysics* (accepted), 2006.

Sato, S, Numerical Simulation of 1993 Southwest Hokkaido Earthquake Tsunami around Okishiri Island, *Journal of Waterway, Port, Coastal and Ocean Engineering,* 22(5), 209-215, 1996.

Shapiro, R., 1970: Smoothing, filtering and boundary effects, *Rev. Geophys. Space Phys.,* 8, 359-387.

Shi, F. Y., J.T. Kirby, R.A. Dalrymple, and Q. Chen, Wave simulations in Ponce de Leon Inlet using Boussinesq model, *Journal of Waterway Port Coastal and Ocean Engineering-Asce,* 129(3), 124-135, 2003.

Smith W. H. F., and D. T., Sandwell, Global sea floor topography from satellite altimetry and ship depth soundings, *Science,* 277, 1956-1962, 1997.

Smith, P. E., A Three-Dimensional, Finite Difference Model for Estuarine Circulation. Dissertation, University of California, Davis, 1997.

Sorensen, R. M., Basic Wave Mechanics for Coastal and Ocean Engineers, John Wiley and Sons, Chapter 2, 1993.

Stoker, J. J., Water Waves: the mathematical theory with applications, New York, Interscience Publishers, 1957.

Synolakis, C. E., J. P. Bardet, J. C. Borrero, H. L. Davies, E. A. Okal, E. A. Silver, S. Sweet, and D. R. Tappin, The slump origin of the 1998 Papua New Guinea Tsunami, *Proceedings of the Royal Society of London Series a-Mathematical Physical and Engineering Sciences,* 458(2020), 763-789, 2002

Synolakis, C. E., P. Liu, G, Carrier and H. Yeh, *Science,* 278(5338), 598 – 600, 1997.

Synolakis, C.E., Tsunami and Seiche, in Earthquake Engineering Handbook, edited by Chen, W–F and Scawthorn, C., CRC Press, 9–1-9–90, 2003.

Tanioka, Y., and M. Okada, *Science of Tsunami Hazards*, 15(2), 67-80, 1997.

Tappin, D. R., P. Watts, G. M. McMurtry, Y. Lafoy, and T. Matsumoto, The Sissano, Papua New Guinea tsunami of July 1998 - offshore evidence on the source mechanism, *Marine Geology*, 175(1-4), 1-23, 2001.

Tinti, S., A. Armigliato, A. Manucci, G. Pagnoni, F. Zaniboni, A. C. Yalciner, Y. Altinok, The generating mechanisms of the August 17, 1999 Izmit bay (Turkey) tsunami: Regional (tectonic) and local (mass instabilities) causes, *Marine Geology* 225(1-4), 311-330, 2006.

Tinti, S., and C. Vannini, Tsunami trapping near circular islands*, Pure Appl. Geophys.* 144, 595–619, 1995.

Tinti, S., Evaluation of Tsunami Hazard in Calabria and Eastern Sicily, Itlay, Tsunamis in the World, Kluwer Academic Publishers, Netherlands, pp. 141-157, 1993.

Titov V.V., and Gonzalez, F. I., Implementation and testing of the method of splitting tsunami (MOST) model, NOAA Technical Memorandum, ERL PMEL-112, 1997.

Titov, V. A. B. Rabinovich, H. O. Mofjeld, R. E. Thomson and F. I. Gonzalez, The global reach of the 26 December 2004 Sumatra tsunami, *Science,* 309, pp. 2045-2048, 2005.

Titov, V. V., H. O. Mofjeld, F. I. Gonzalez, and J. C. Newman, Offshore forecasting of Alaska-Aleutian Subduction Zone tsunamis in Hawaii. NOAA Tech Memo. ERL PMEL-114, Seattle, WA, 22 pp, 1999.

Titov, V. V., H. O. Mofjeld, Frank I. Gonzalez, and J. C. Newman, Offshore forecasting of Hawaiian tsunamis generated in Alaskan-Aleutian Subduction Zone, NOAA Technical Memorandum ERl MEL-114. pp. 21, 1999.

Titov, V.V., and C. E. Synolakis, Numerical modelling of tidal wave runup, *Journal of Waterway Port Coastal and Ocean Engineering-Asce*, 124(4), 157-171, 1998.

Todd, D. Regional Tsunami Studies: Canterbury & Otago, *TEPHRA*, pg 56, October, 1999.

Walder, J. S., P. Watts and C. F. Waythomas, Case Study: Mapping Tsunami Hazards Associated with Debris Flow into a Reservoir, *J. Hydr. Engrg,* 132 (1), 1-11, 2006.

Walder, J. S., P. Watts, and C. F. Waythomas, Case study: Mapping tsunami hazards associated with Debris flow into a reservoir, *Journal of Hydraulic Engineering-Asce,* 132(1), 2006.

Walters, R. A., A semi-implicit finite element model for non-hydrostatic (dispersive) surface waves, *Int. J. Numer. Meth. Fluids*, 49, 721-737, 2005.

Walters, R. A., D. G. Goring and R. G. Bell, Ocean tides around New Zealand, *New Zealand Journal of Marine and Freshwater Research,* 35, 567–579, 2001.

Walters, R. A., Long wave resonance on the New Zealand coast. NIWA Technical Report 109, 32 pp, 2002.

Walters, R. A., P. Barnes and J. R. Goff, Locally generated tsunami along the Kaikoura coastal margin: Part 1. Fault ruptures, *New Zealand Journal of Marine and Freshwater Research*, 40(1), 17- 28, 2006.

Walters, R., and J. R. Goff, Assessing tsunami hazard on the New Zealand coast, *Science of Tsunami hazards*, 21 (3), 137-153, 2003.

Ward, S., and S. Day, Cumbre Vieja Volcanoe-Potential collapse and tsunami at La Palma, Canary Islands, *Geophysical Research Letters,* 28(17), 3397-3400, 2001.

Watts et al., Ocean Waves Measurement and Analysis. Paper number 221, Presented at the Fifth International Symposium WAVES 3rd-7th July, Madrid, Spain, 2005.

Watts, P., (2002), Geowave V1.0, courtesy of Applied Fluids.

Watts, P., (2002), TOPICS V1.2, (a component of Geowave), courtesy of Applied Fluids.

Watts, P., F. Imamura and S. Grilli, Comparing model simulations of three benchmark tsunami generation cases, *Science of Tsunami Hazards*, 18 (2), 107-123, 2000.

Watts, P., J. C. Borrero, D. R. Tappin, J. P. Bardet, S. T. Grilli and C. E. Synolakis, Novel simulation technique employed on the 1998 Papua New Guinea tsunami, presented at the IUGG General Assembly in Birmingham, UK, and published by the first author at www.appliedfluids.com/rsume.html, 2002.

Watts, P., M. Ioualalen, S. T. Grilli, J. T. Kirby, and F. Shi, Numerical simulations of the December 26, 2004 Indian Ocean tsunami using a higher-order Boussinesq model', Proc. Waves'05, Madrid, July 3-7 Paper 221, 2005.

Watts, P., M. Ioulalen, S. T. Grilli., F. Shi, and J. T. Kirby, Numerical Simulation of the December 26, 2004 Indian Ocean Tsunami using a Higher-order Boussinesq Model, In Proc. 5th Intl. on Ocean Wave Meas. And Analysis (WAVES 2005, Madrid, Spain, July 2005), ASCE Publ., paper 221, 2005.

Watts, P., S. T Grilli, J. T. Kirby, G. J. Fryer and D. R. Tappin, Landslide tsunami case studies using a Boussinesq model and a fully non linear tsunami generation model, *Natural Hazards and Earth System Sciences*, 3, 391–402, 2003.

Watts, P., Tsunami features of solid block underwater landslides, *Journal of Waterway Port Coastal and Ocean Engineering-Asce,* 126(3), 144-152, 2000.

Wei, G., and J. T. Kirby, Time-dependent numerical code for extended Boussinesq equations, *Journal of Waterway Port Coastal and Ocean Engineering-Asce*, 121(5), 251-261 1995.

Wei, G., J T. Kirby, S. T. Grilli, and R. Subramanya, A fully nonlinear Boussinesq model for surface waves. Part 1: Highly nonlinear unsteady waves, *J. Fluid Mech.,* 294, 71-92, 1995.

Yalciner, A. C., U. Kuran, A. Akyarli, and F. Imamura, An investigation on the propagation of tsunamis in the Aegean Sea by mathematical modelling, In Tsunami: Progress in prediction, disaster prevention and warning (eds., Tsuchiya,Y., and Shuto, N.) (Kluwer Academic Publishers, Dordrecht, 1995) pp. 55–70.

Yeh, H. Liu, P., and Synolakis, C. (ed.), 1996 Long-wave runup models. World Scientific.

Yeh, H., P., Liu, and Synolakis, C. (ed.), 1996 Long-wave run up models. World Scientific.

Zelt, J. A. Tsunamis, The response of harbours with sloping boundaries to long wave excitation. Division of Engineering and Applied Science. California Institute of Technology, Pasadena, California. June, 1986.